Saturation-Recovery T_1 (SR-T_1) Method: A Dynamic Neuroimaging Tool for Assessment of Perfusion Change

A Dissertation
SUBMITTED TO THE FACULTY OF
UNIVERSITY OF MINNESOTA
BY

Xiao Wang

IN PARTIAL FULFILLMENT OF THE REQUIREMENTS
FOR THE DEGREE OF
DOCTOR OF PHILOSOPHY

Wei Chen, E. Russell Ritenour

October 2013

Acknowledgements

I would like to express my deepest appreciation to my advisor Professor Wei Chen, I will forever be grateful for his guidance and encouragement during my studies for the doctorate and even for my entire future life. He is a knowledgeable scholar, a passionate scientist, an exceptional mentor and a great gentleman. Consistently and convincingly, he conveyed a spirit of adventure in regard to research and an excitement in regard to teaching. I could not get a better advisor than him. Without his persistent supervision and help this dissertation would not have been possible.

I also owe special thanks my co-advisor Professor E. Russell Ritenour and to my committee members: Professor Kamil Ugurbil, Essa Yacoub and Walter Low, they all provided invaluable instructions as I progressed through my graduate school studies and engaged me with insightful discussion and gave me suggestions for my research.

In addition, this research would never have come together without the assistance of various individuals. Professor Xiao-Hong Zhu has always been available to discuss and help whenever I have had problems, even on weekends. Her rigorous academic attitude about science, her perspective insight, and diligent work really impressed and inspired me. She has set an example as a true scientist, whom I admire and from whom I need to learn. Yi Zhang worked closely with me on the animal studies and I cannot imagine how I would have proceeded with my experiments without his help. Professor Afshin Divani kindly provided the middle cerebral artery occlusion (MCAO) and traumatic brain injury (TBI) rat model, which enabled the application of our technique to the diseased model.

All the faculty and staff at the Center for Magnetic Resonance Research (CMRR) have provided me with support and assistance in one way or another as I pursue my PhD degree. CMRR is like a big family to me, a place where I never hesitate to ask

for help in any aspect. I would like to extend my special thanks to Gregor Andriany, Ivan Tkac, Dinesh Deelchand, Naoharu Kobayashi, Brian Hanna, Janis Zeltins and Andy Berhow for their technical support and selfless help.

Last, but not least, my family members and my friends are the source of my research impetus and joy. I wish to thank them for their support, encouragement, unconditional love and care throughout my studies.

Dedication

This thesis is dedicated to my husband Li Zheng and lovely daughter, Ke-xin Zheng; my parents, Si-yuan Wei and Xian-e Wang, my sister Lu Wei.

Abstract

A working brain requires continuous oxygen and nutrition supply through the circulation of Cerebral Blood Flow (CBF). CBF and its change closely reflect the energy demand of neuron activity and are highly related to variety of cerebral diseases as well. It is of great importance to noninvasively and reliably mapping CBF and its change under physiological and pathological conditions.

The goal of this research is to develop a sensitive, reliable and noninvasive MRI neuroimaging technique based on Saturation-recovery longitudinal relaxation time (SR-T_1) method to imaging CBF change and Blood Oxygen-Level Dependent (BOLD) signal simultaneously. First, the theoretical and mathematical model of SR-T_1 method is derived and MRI sequence design is described. This technique is tested on physiological and pathological rat models at 9.4T and is validated by indirect Laser Doppler Flowmetry (LDF) and direct Continuous Arterial Spin Labeling (CASL) CBF approaches. Some technical confounding factors are also investigated and discussed (Chapter 2 to 4). Second, the SR-T_1 method of imaging CBF change is applied at two different magnetic fields (9.4T and 16.4T) to examine the notion that T_1 is field dependent whereas CBF change in response to physiological or pathological perturbation is field independent (Chapter 5). Third, the SR-T_1 method is performed to quantitatively investigate the perfusion contribution to the total functional MRI (fMRI) signal using a rat model with mild hypercapnia at 9.4T and human subjects with visual stimulation at 4T. It reveals that an improved fMRI contrast-to-noise ratio and spatial specificity for mapping brain activity and physiology changes could benefit from appropriately choosing the MRI

parameters in enhancing perfusion contribution to the total fMRI signal (Chapter 6). Fourth, the SR-T_1 method is carried out on Middle Cerebral Artery Occlusion (MCAO) rat model at 1 day and 7 days of post-ischemia and then is compared to the CBF change measured by the CASL technique in varied lesion regions of rat brain. The comparison reveals a good correlation of CBF change measured with these two perfusion techniques. A variety of MR imaging modalities, such as Apparent Diffusion Coefficient (ADC) images and Cerebral Vascular Reactivity (CVR) images as well as histology are also performed on the MCAO rat brain to longitudinally study the reperfusion injury (Chapter 7). Finally, the major conclusions are summarized and the future prospects are discussed and proposed in Chapter 8.

In conclusion, the SR-T_1 method developed and applied in this thesis should provide an alternative, noninvasive and reliable neuroimaging tool to study CBF change and BOLD under both physiological and pathological conditions.

Table of Contents

List of Tables

List of Figures

List of Symbols and Abbreviations

ADC: apparent diffusion coefficient

ASL: arterial spin labeling

ATP: adenosine triphosphate

BOLD: blood oxygen-level dependent

CASL: continuous arterial spin labeling

CBF: cerebral blood flow

$CMRO_2$: cerebral metabolic rate of oxygen

CVR: cerebral vascular reactivity

DSC: dynamic susceptibility contrast

EPI: echo-planar imaging

FAIR: flow sensitive alternating inversion recovery

fMRI: functional magnetic resonance imaging

H.E.: Hematoxylin and eosin

LDF: laser Doppler flowmetry

MCAO: middle cerebral artery occlusion

MRI: magnetic resonance imaging

MRS: magnetic resonance spectroscopy

MT: magnetization transfer

N_2O: nitrous oxide

NIRS: near-infrared spectroscopy

OEF: oxygen extraction fraction

PASL: pulsed arterial spin labeling

PBS: phosphate buffered saline

PET: positron emission tomopraphy

QUIPSS II: Quantitative Imaging of Perfusion with a Single Subtraction, version II

SI: signal intensity

SPECT: single-photon emission computed tomography

TBI: traumatic brain injury

TCD: transcranial Doppler sonography

TIA: transient ischemic attack

CHAPTER 1 Introduction

A working brain needs continuous supply of oxygen and nutrition through cerebral blood flow (CBF). In an adult, the amount of CBF consists of approximately 15-20% of cardiac output, which is about 0.5ml/g/min [1-3]. CBF is regionally heterogeneous and it is tightly coupled with the local cerebral metabolism demand for oxygen and glucose required by the neuron activity. Moreover, varieties of cerebral diseases, such as transient ischemic attack (TIA), stroke, tumor, multiple sclerosis are also accompanied with CBF abnormality [4-6]. Therefore, measurement of CBF and its change are of great importance to evaluate brain function, metabolism and tissue viability.

1.1 Background and Motivation

Tremendous efforts have been made to measure CBF and remarkable number of techniques have been established and investigated. The earliest work of measuring CBF on human was done by Kety and Schmidt [7], nitrous oxide (N_2O) was used as a diffusible tracer and its rate of reaching the equilibrium state is very sensitive to global CBF. Other exogenous and radioactive tracers, such as krypton-85 and xenon-133 [8] were also employed for regional CBF measurement by monitoring the tissue concentration of the radioactive tracers through an external multiple scintillation detectors recording. [9-12]. Later on, positron emission tomography (PET) and single-photon emission computed tomography (SPECT) had been developed not only to image CBF spatially, but also to assess brain metabolism as well. [1, 13-15] Very recently, a novel technique conceptually similar to PET measurements using $H_2{}^{15}O$, utilizing ^{17}O

NMR signal of metabolically produced $H_2{}^{17}O$ in the rat brain following $^{17}O_2$ inhalation succeeded in imaging both cerebral metabolic rate of oxygen ($CMRO_2$) and CBF simultaneously [16, 17]. Nevertheless, almost all of these techniques involve (radioactive) tracers and suffer from the poor resolution and high cost. Radioisotope labeled microsphere technique [18, 19] provided a nondiffusible and direct means of measuring flow, which enabled a reliable quantification of global and regional CBF as well as blood flow in different organs. However, it requires repeated injection of different radioactive nuclei labeled microspheres for serials of CBF measurement.

There are some other qualitative methods of measuring CBF and not involved radioisotope tracers, such as laser Doppler flowmetry (LDF) [20, 21], transcranial Doppler sonography (TCD), [22, 23] near-infrared spectroscopy (NIRS) [24, 25] and thermal diffusion technique [26]. The former two techniques are based on the reflected frequency shift of the moving blood cells. NIRS depends on the tissue absorption difference of the certain wavelength and the thermal diffusion technique is based on the thermal conductivity of cortical tissue, allowing continuous recordings of CBF in a small region of cortex. The disadvantages of these techniques are that they provide only localized and relative CBF measurement with limited spatial resolution.

Perfusion imaging measured by magnetic resonance imaging (MRI) techniques developed rapidly during the past two decades. There are two main categories of MRI-based CBF measurement: one is dynamic susceptibility contrast (DSC) imaging which normally acquired after the injection a bolus of paramagnetic contrast agent [27, 28]; the other one uses radiofrequency (RF) pulses label moving spins as an endogenous contrast

in flowing blood, which called arterial spin labeling (ASL). [29-35]. Strictly speaking, only the second category ---ASL is a truly noninvasive technique.

The ASL based perfusion image usually generates from a pair of images. Figure 1.1 shows a schematic graph of magnetization preparation and acquisition of these paired images. The flowing water spins in the arterial blood are labeled magnetically when they travel through an inversion plane or band (Figure 1.1a), as these spins reach the capillaries and rapidly exchange with the static spins in the image slice after a inversion recovery time (TI), a "tagged" image is acquired. The control image (Figure 1.1b) is acquired in the same way except for the inversion plane or band being made at the equidistant of the other side of the image slice. By acquiring this control image, the off resonance effect of static spins in the image slice is balanced. The magnetization difference of these two images is proportional to the arterial blood delivered to the image plane since the background of static signal is subtracted out. Usually a serial of image volumes need to be averaged in order to improve the signal to noise ratio because the signal difference of one pair of image is only a few percent.

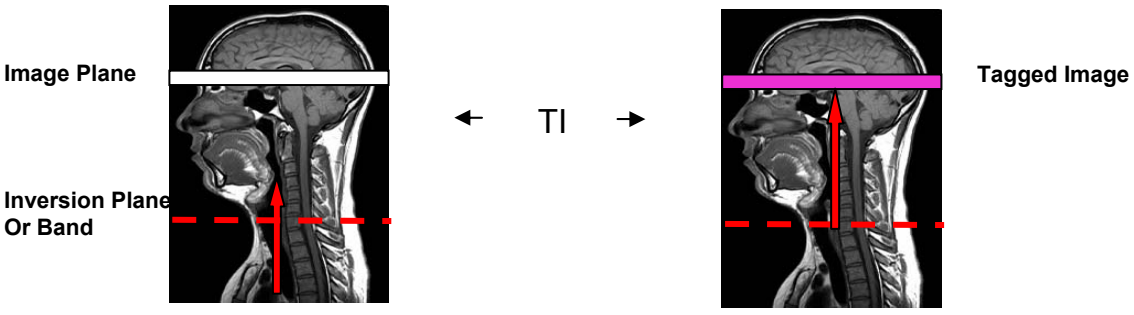

(a)

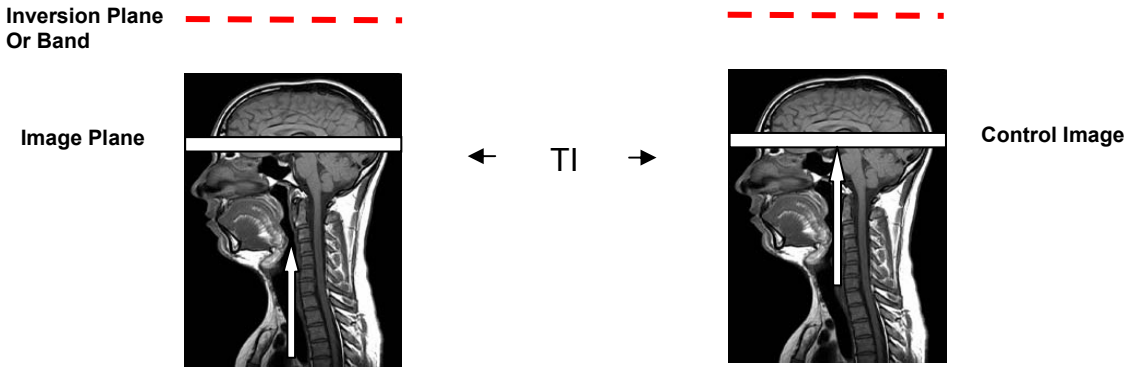

(b)

Figure 1.1 Schematic graph of paired images obtained with the ASL technique. (a) The flowing water spins in the arterial blood are labeled magnetically when they travel through an inversion plane or band (dash red line), as these spins reach the capillaries and rapidly exchange with the static spins in the image slice after a inversion recovery time (TI), a "tagged" image is acquired. (b) The inversion plane or band (dash red line) is made at the equidistance of the other side of the image slice, a control image is acquired after an identical TI.

Depending on how the magnetization of image slice is prepared and how the flowing spins are labeled, different versions of ASL can be derived. (See the review articles and the cited references therein [36]).

The innovation of this thesis comes from the observation that tissue relaxation parameter T_1-sensitive pulse sequence or the parametric T_1 images by using inversion-recovery (IR) preparation with varied inversion-recovery time (T_{IR}) could also reflect the CBF change during brain activations. [33, 37, 38]. Moreover, several groups have reported early (even within a few minutes after the middle cerebral artery occlusion) increase of T_1 in focal cerebral ischemic rat models, indicating T_1 indeed is sensitive to CBF decrease.[39-42]. Inspired by these findings, global saturation combined with EPI sampling to measure T_1 was applied to measure CBF change. It turns out that ASL and T_1

perfusion model are physically coherent per se, but view spin exchange from different standpoints. The former focuses the magnetization change by delivering tagged spins to the image at a certain inversion recovery time (T_{IR}) or saturation recovery time (T_{SR}) while T_1 perfusion model views CBF via an evolution process of longitudinal relaxation time T_1. In this thesis, we demonstrate that SR-T_1 method is feasible to provide an alternative, reliable and noninvasive neuroimaging tool to monitor CBF change and BOLD simultaneously.

1.2 Study Aims and Steps

The primary purposes of this dissertation are

i) to develop and validate a new neuroimaging tool (the SR-T_1 MRI method) enables noninvasively and simultaneously imaging CBF change and BOLD;

ii) to apply this new technique to monitor CBF and BOLD change under physiological and pathological conditions;

iii) to understand, explain physical meaning of different components of fMRI signal and subsequently provide guidance of improving the quality of fMRI imaging.

In order to achieve these goals, the following several steps are gradually accomplished:

i) develop and derive the theoretical and mathematical model of the SR-T_1 MRI method;

ii) validate this method with indirect (LDF) and direct method (CASL) of measuring CBF in rat brain under physiological and pathological conditions at 9.4T;

iii) investigate the influence of confounding factors (large vessel inflow effect and artery transit time) for imaging T_1 and CBF change with the SR-T_1 MRI method by incorporating bipolar diffusion gradient before the EPI sampling and manipulating the

varied slab thickness of saturation region;

iv) verify the notion that CBF change is field independent and T_1 is field dependent by performing the SR-T_1 MRI method of imaging CBF change at different magnetic field: 9.4T and 16.4T;

v) quantitatively investigate and decompose the total fMRI signal components by using a rat model with mild hypercapnia at 9.4T and human subjects with visual stimulation at 4T, explain and provide guidance for optimizing the MR parameters and improving the fMRI imaging quality;

vi) apply the SR-T_1 MRI method to middle cerebral artery occlusion (MCAO) rat model and combine different MRI modalities to longitudinally study the reperfusion damage in MCAO rat brain.

1.3 Chapter Overview

Chapter 2 derives the theoretically mathematical model and describes the MRI sequence design of the proposed SR-T_1 MRI method for simultaneously imaging CBF change and BOLD. Sensitivity and reliability are tested in a wide range of physiological (mild hypercapnia) and pathological (global ischemia with four-vessel occlusion) conditions in rat brain at 9.4T. Meanwhile, the measured CBF change is validated with the concurrent relative CBF change monitoring using LDF. The distinct dynamic temporal behavior of CBF and BOLD under physiological and pathological conditions is observed and briefly discussed.

Chapter 3 aims to examine whether the general confounding factors for MR techniques of imaging CBF, i.e. the large vessel inflow effect and artery transit time

would significantly contaminate the quantification of T_1 image and subsequently the CBF change using the SR-T_1 MRI method. Bipolar diffusion gradients are incorporated before the EPI sampling to investigate the inflow effect and the varied slab thickness saturation region are created to inspect the artery transit time influence of imaging T_1 and the ensuing CBF change. Data shows that these two confounding factors have negligible effects on quantifying the CBF change based on the SR-T_1 MRI method.

Chapter 4 further validates the SR-T_1 MRI method of imaging CBF change with the direct comparison of that measured with the standard CASL technique. It shows an excellent agreement of CBF increase induced by varied degree of mild hypercapnia calculated with these two techniques. Moreover, other important parameters, i.e. T_1^{int} and blood partition coefficient λ are numerically obtained based on these two measurements. baseline CBF also could be computed once the T_1^{int} is determined using SR-T_1 MRI method.

Chapter 5 applies the SR-T_1 MRI method of imaging CBF change at two different magnetic fields (9.4T and 16.4T) and verifies the concept that CBF increase in response to vascular stimulus is field independent while T_1 value is field dependent. Meanwhile, the CBF increase during the mild hypercapnia calculated at both magnetic fields is consistent with that measured with CASL technique.

Chapter 6 and chapter 7 describe the application of the SR-T_1 MRI method to understand and explain the physical meaning of the different components of fMRI signal, and to employ this method to imaging CBF change in a diseased rat model--MCAO rat brain. Chapter 6 quantitatively investigates the perfusion contribution to the total fMRI

signal using a rat model with mild hypercapnia at 9.4T and human subjects with visual stimulation at 4T. It reveals that the total fMRI change could be approximated as a linear superposition of "true" BOLD effect and blood flow-related (T_1) effect. Wisely choose the appropriate parameters (short TR and large radiofrequency pulse flip angle) of the fMRI acquisition lead to a flow-related signal enhancement, which is beneficial to an improved contrast-to-noise ratio and spatial specificity for mapping brain activity and physiology changes.

Chapter 7 applies the SR-T_1 MRI method of imaging CBF change to a diseased rat model—MCAO rat on day 1 and day 7 of post-ischemia and compares it with CASL technique in varied lesion region of the rat brain. It reveals that the CBF change in different regions of interest calculated with the SR-T_1 MRI method and the CASL technique are very consistent. A variety of MR imaging modalities, such as ADC images and CVR images as well as histology are also performed on the MCAO rat brain to longitudinally study the post-ischemic reperfusion injury.

Chapter 8 gives the summary of major conclusions of this thesis and some consideration of further technical investigation as well as future prospects of the application of the SR-T_1 MRI method.

CHAPTER 2 Simultaneous Imaging of Absolute CBF Change and BOLD with Saturation-Recovery (SR) -T_1 Method

Abstract

A neuroimaging technique based on the saturation-recovery (SR)-T_1 MRI method was applied for simultaneously imaging BOLD and absolute cerebral blood flow change (ΔCBF), which is determined by CBF-sensitive T_1 relaxation rate change (ΔR_1^{CBF}). This technique was validated by examining the relationships among ΔR_1^{CBF}, ΔCBF, BOLD and relative CBF change, which was simultaneously measured by laser Doppler flowmetry in the rat brain under global ischemia and hypercapnia conditions. It was found that during one-minute ischemia, BOLD decreased 23.1±2.8% in the cortical area; ΔR_1^{CBF} decreased 0.020±0.004s^{-1} corresponding to a ΔCBF decrease of 1.07±0.24 ml/g/min and 89.5±1.8% CBF reduction (n=5). These measured parameters were used to estimate the baseline CBF value (=1.18 ml/g/min), which is consistent with the literature. It was also found that the brain temperature decreased during ischemia and increased during post-ischemia period. CBF change quantification based on temperature corrected ΔR_1^{CBF} had a better accuracy than apparent R_1 change (ΔR_1^{app}); nevertheless, ΔR_1^{app} without temperature correction still provides an approximation for determining CBF change since perfusion dominates the evolution of the longitudinal relaxation rate. There was an excellent consistency between ΔCBF and the CBF percentage change measured during and after ischemia. In contrast,

the BOLD change during the post-ischemia period was temporally disassociated with ΔCBF, indicating distinct CBF and BOLD responses. Similar results were also observed for the hypercapnia study. In summary, the overall results demonstrate that the SR-T_1 MRI method is effective for imaging both absolute CBF change and BOLD noninvasively; and it provides an alternative and simple neuroimaging method to image CBF/BOLD changes associated with physiological (e.g., brain activation) and/or pathological (e.g., ischemia) changes.

Keywords: perfusion; cerebral blood flow; saturation-recovery-T_1 MRI; laser Doppler flowmetry; ischemia; hypercapnia; inflow effect; transit time.

2.1 Introduction

Blood perfusion through the cerebral capillary bed is essential for brain function. Imaging of cerebral blood flow (CBF) provides valuable information regarding brain physiology, function, activation and tissue viability associated with a large number of brain diseases. With the development of a large number of imaging methods from the microsphere and autoradiography techniques to positron emission tomography (PET) and single photon emission computed tomography (SPECT), tremendous progress has been made in improving the spatial/temporal resolution and quantification for mapping CBF [7]; [1, 9, 43]. All of these techniques rely on the use of exogenous and radioactive tracers. In contrast, Laser Doppler flowmetry (LDF) measures a frequency shift in light reflected from moving red blood cells [44, 45]. It enables a real-time, continuous

recording of relative (or percent) CBF change in a focal point; and is regarded as a standard tool for dynamic CBF measurements [46]. Moreover, LDF-based CBF measurements have been reported to be in good agreement with the radioactive microsphere CBF measurements [45, 47] as well as the hydrogen clearance CBF measurements [48]. However, LDF technique is an invasive method and provides only a relative perfusion change with limited spatial information.

One newly developed MRI technique for imaging CBF is the arterial spin labeling (ASL) methods for tagging the arterial water spin as an endogenous and diffusible tracer, which can be mixed with the unlabeled stationary spins of brain tissue water. The dynamic mixing between the labeled and non-labeled spins can alter the apparent longitudinal relaxation time (T_1^{app}) of water and the T_1-weighted MRI signal intensity (SI), that can be quantitatively linked to CBF and used to obtain high-resolution CBF images in a completely noninvasive manner [29, 30, 32, 33, 37, 38]. An inversion-recovery preparation is commonly applied for most ASL methods, and paired images (one control and another with spin tagging) are acquired with an appropriate inversion recovery time. The signal difference can be used to determine the CBF value. These MRI techniques provide an efficient neuroimaging modality for assessing CBF and are particularly useful for imaging relative CBF changes, for instance, induced during brain activation [49, 50] and/or physiology/pathology perturbations.

An alternative MRI-based CBF imaging method is to measure the parametric T_1^{app} images directly by using inversion-recovery preparation with varied inversion-recovery time (T_{IR}) [33, 37, 38]. Due to the slow T_1^{app} relaxation processing, this method requires a

relatively long repetition time (TR) to acquire a number of images with different T_{IR} values in order to generate T_1^{app} images, thus, results in low efficiency and low temporal resolution for imaging CBF. Nevertheless, this method could be more accurate in quantifying CBF and its change in the absolute scale with the unit of ml blood/g brain tissue/min (or ml/g/min) compared to other ASL methods, which are commonly confounded by multiple physiology parameters required for quantification and the complexity of blood circulation in a living brain (see more details in **Method and Theory**).

One common, interesting observation related to T_1^{app} changes in the literature is the detection of T_1^{app} increase at an early stage of ischemia, indicating a possible connection between the T_1^{app} change and the perfusion deficit caused by the ischemia [39, 42, 51, 52]. However, the quantitative relationship between the observed T_1^{app} change and the CBF reduction extent caused by acute ischemia has not been rigorously, quantitatively studied. A potential difficulty for quantifying CBF via the measurement of T_1^{app} lies on the confounding effect from the brain tissue temperature change owing to physiological and/or pathological perturbation, which can contribute to the T_1^{app} change [53-56]. Consideration and correction of this confound effect certainly would improve the accuracy of quantifying CBF based on the T_1^{app} measurement. Another complexity is the phenomena of concurrent changes in both perfusion and the blood oxygenation level dependence (BOLD) contrast [57, 58] during either physiology perturbation (e.g., brain stimulation) or pathology perturbation (e.g., hypoxia via ischemia); and these changes

could affect the MRI intensity via either T_1^{app}–based mechanism owing to perfusion change or T_2/T_2^*–based mechanism owing to BOLD contrast.

To address these issues, we conducted a study aiming to: i) propose an imaging approach to simultaneously measure and image the CBF change in an absolute unit (the absolute CBF change for short in the rest of this thesis) and the BOLD contrast by using the SR-T_1 MRI method; ii) validate this approach by conducting simultaneous *in vivo* measurements of absolute CBF change using the SR-T_1 MRI method and the relative CBF change using LDF recording under transient hypercapnia (increasing CBF) and acute ischemia (reducing CBF) conditions using a rat model at 9.4T; iii) investigate the effect of brain temperature change on T_1^{app} and the apparent longitudinal relaxation rate ($R_1^{app}=1/T_1^{app}$) after the induction of hypercapnia or ischemia (see Supplementary Materials); iv) establish the quantitative relationship between the CBF-sensitive R_1 change (ΔR_1^{CBF}) and the absolute CBF change (ΔCBF); and v) quantitatively study the temporal relationships among R_1^{CBF} change, ΔCBF, relative CBF change and BOLD during and after hypercapnia or ischemia.

2.2 Method and Theory

2.2.1 Saturation-recovery (SR) -T_1 MRI pulse sequence for imaging T_1^{app}

The MRI perfusion method described herein relies on T_1^{app} mapping using global magnetization saturation-recovery preparation and fast echo-planar imaging (EPI) sampling [59]. The global saturation-recovery preparation is achieved by a radiofrequency

(RF) surface coil with a focal, intense RF field (B_1) covering the rat brain [60]. Figure 2.1 is the schematic diagram showing the principle underlying the SR-T_1 MRI method.

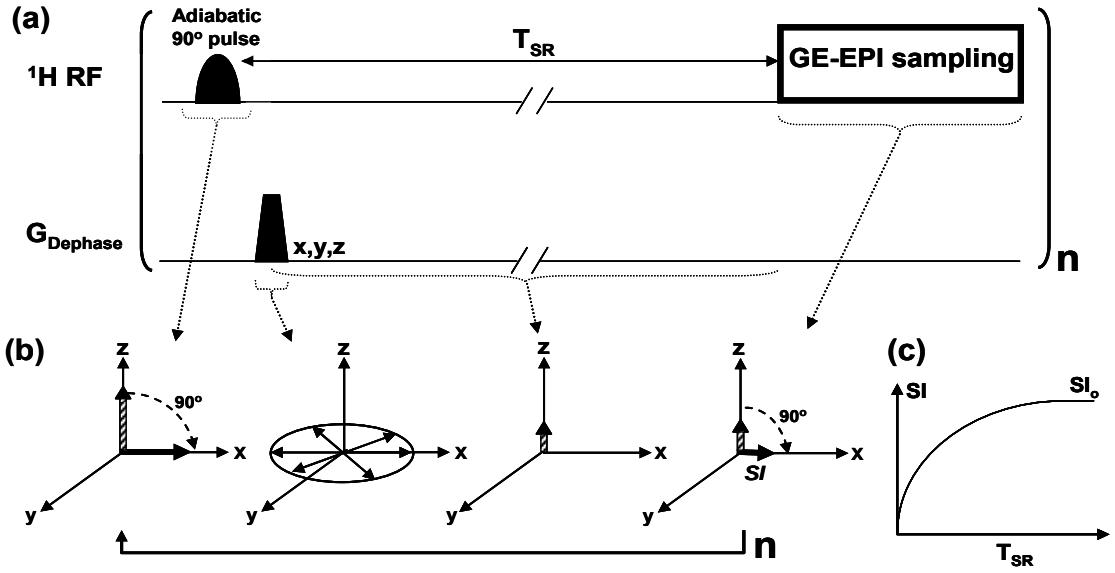

Figure 2.1 Schematic diagram of MRI sequence and spin magnetization in rotating frame of SR-T_1 method. (a) Gradient echo EPI (GE-EPI) sampling is applied after the saturation-recovery waiting time (T_{SR}). There is no an extra delay time among the imaging acquisition and the next saturation pulse. This imaging measurement is repeated n times with varied T_{SR}. (b) Schematic diagram illustrating the principle underlying the imaging sequence in the spin rotating frame. It shows the rotation of longitudinal magnetization, dephasing of transverse magnetization and the transverse magnetization changes after T_{SR} and spin excitation pulse, which is detected by GE-EPI. (c) Exponential recovery curve of EPI signal intensity (SI) as a function of T_{SR}. The regression of this curve determines the apparent T_1 value that is sensitive to perfusion.

The global magnetization saturation preparation is achieved by an adiabatic half passage 90^o RF pulse, which is insensitive to the inhomogeneous B_1 field of a surface coil, immediately followed by dephasing gradients ($G_{Dephase}$) in three dimensions (Figure. 2.1a). The adiabatic 90^o pulse rotates the longitudinal magnetization (M_z) into the transverse

plane in a spin rotating frame, resulting in the transverse magnetization (M_{xy}) with the same magnitude of M_z. The M_{xy} rapidly loses its phase coherence because of the strong dephasing effect by $G_{Dephase}$. The overall effect of the magnetization saturation preparation is to approach zero magnetizations for both M_z and M_{xy} components (Figure. 2.1b). This magnetization preparation is independent of the initial M_z value or its reduction owing to the partial magnetization saturation effect when a relatively short TR is applied. Therefore, no extra delay before the adiabatic 90^o pulse is needed. This feature can significantly improve the temporal resolution for imaging T_1^{app} as compared to the conventional inversion-recovery preparation in which the net magnitude of inverted M_z depends on the initial M_z prior to the inversion pulse and the effect of partial saturation as a function of TR; thus, in which a relatively long TR is preferred. During the period of saturation-recovery time (T_{SR}), the longitudinal magnetization starts to relax and recover according to an exponential function (Figure. 2.1c). This recovered M_z is rotated to the transverse plane again by a spin excitation pulse with a nominal 90^o flip angle, and then sampled by EPI acquisition. The detected EPI signal intensity (SI), in general, obeys the following equation:

$$SI = SI_0 \cdot [1 - e^{(-\frac{T_{SR}}{T_1^{app}})}] \cdot e^{(-\frac{TE}{T_2^*})} \qquad (2.1)$$

where TE is the spin echo time; and T_2^* is the apparent transverse relaxation time, which is sensitive to magnetic field inhomogeneity and susceptibility effects, such as the BOLD contrast; SI_0 is the EPI signal intensity when TE=0 and $T_{SR}=\infty$. This equation can be used to the T_1^{app} regression based on a number of SI measurements with varied T_{SR}.

When T_{SR} is sufficiently long (e.g., $\geq 4T_1^{app}$ as applied in this study) and TE>0, the second term in Eq. (1) approaches one, and Eq. (1) becomes:

$$SI^* = SI_0 \cdot e^{(-\frac{TE}{T_2^*})}. \quad (2.2)$$

Under this condition, SI^* is determined by the T_2^* relaxation process and becomes independent of T_1^{app}; thus, this signal can be used to quantify the BOLD contrast [57, 58]. Moreover, the addition of SI^* measurement with a long TR is critical to improve the reliability and accuracy for T_1^{app} regression, which is essential in determining the absolute CBF change, though it leads to a relatively low temporal resolution for obtaining T_1^{app} and BOLD images.

In this study, two categories of brain conditions are defined by the subscript "RC" standing for the Reference Condition (i.e., control) before the induction of physiological/pathological perturbation, and the subscript "PC" standing for the Perturbed Condition by the induction of either hypercapnia or ischemia. Accordingly, the BOLD contrast can be quantified by:

$$BOLD = \frac{SI^*_{PC} - SI^*_{RC}}{SI^*_{RC}} \quad or \quad rBOLD = \frac{SI^*_{PC}}{SI^*_{RC}} \quad (2.3)$$

where rBOLD stands for the relative BOLD.

2.2.2 Two-phase arterial spin modeling of rat brain magnetization in SR-T_1 method

The Block equation describes the dynamic behavior of brain magnetization as the following:

$$\frac{dM_b(t)}{dt} = \frac{M_b^0 - M_b(t)}{T_1} + f\left[M_a(t) - M_v(t)\right] \qquad (2.4)$$

where M_a, M_b and M_v are the longitudinal magnetization of the arterial blood, brain tissue and venous blood respectively; M_b^0 is the equilibrium value of M_b; T_1 is the brain tissue longitudinal relaxation time in the absence of flow; f represents the CBF value. Assuming that the brain tissue is a single, well-mixed compartment, so that $M_v(t) = M_b(t)/\lambda$, λ is blood-tissue water partition coefficient (= 0.9 ml/g). [61], Eq. (4) can be rewritten as:

$$\frac{dM_b(t)}{dt} = \frac{M_b^0 - M_b(t)}{T_1} + f\left[M_a(t) - \frac{M_b(t)}{\lambda}\right] \qquad . \qquad (2.5)$$

Associated with our experimental MR preparation and acquisition, we solve Eq. (2.5) with a two-phase arterial spin model individually illustrated in Figure 2.2 showing the schematic graph of the global brain region (shaded area) saturated by the surface coil overlapped on a rat brain sagittal anatomic image.

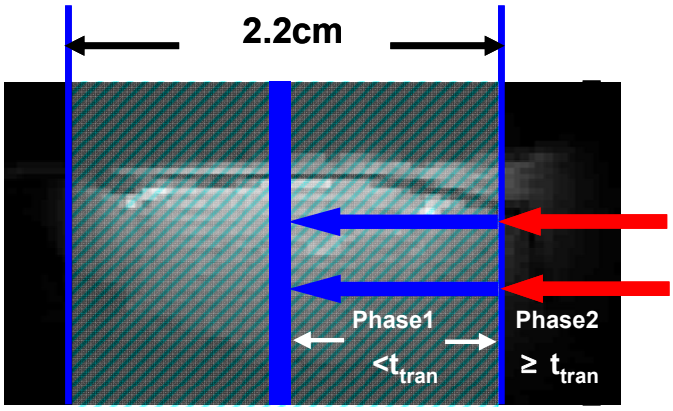

Figure 2.2 Schematic diagram for showing the global saturation region (shaded area) achieved by the surface coil being used in the study overlapped on a rat brain sagittal anatomic image. The blue arrows

stand for the phase 1 arterial spins in the global saturation region and travel into the image slice within the time window t_{tran}. The red arrows indicate the unsaturated phase 2 arterial blood spins and flow into the image slice longer than t_{tran}.

Phase 1 presents the time window in which the image slice receives the saturated arterial spins within the global saturation region (as indicated with the blue arrows in the figure); and Phase 2 is related to the time window when the fresh, fully relaxed arterial spins outside of the saturation region (as indicated with the red arrows in this figure) flow into the image slice. Assuming the arterial blood spins travel smoothly as bulk flow at a constant speed without any turbulence. The fresh spins at the edge of the saturation region will take the artery transit time (t_{tran}) to reach the image slice. For the SR-T_1 measurement with a saturation-recovery time (t) being shorter than t_{tran} ($t < t_{tran}$, i.e., Phase 1), the magnetization recovery of the saturated arterial spin as a function of time ($M_a(t)$) can be expressed as:

$$\frac{dM_a(t)}{dt} = \frac{M_a^0 - M_a(t)}{T_{1a}} \qquad (2.6)$$

where T_{1a} is the longitudinal relaxation time of arterial blood; M_a^0 is the M_a value at an equilibrium state and can be approximated by $M_a^0 = M_b^0/\lambda$. Eq. (2.6) has a solution,

$$M_a(t) = M_a^0\left[1 - e^{-\frac{t}{T_{1a}}}\right] = \frac{M_b^0}{\lambda}\left[1 - e^{-\frac{t}{T_{1a}}}\right] \qquad (2.7)$$

Eqs (2.5) and (2.7) lead to:

$$\frac{dM_b(t)}{dt} = \frac{M_b^0 - M_b(t)}{T_1^{app}} - \frac{M_b^0 \cdot f}{\lambda} \cdot e^{-\frac{t}{T_{1a}}} \tag{2.8}$$

where

$$\frac{1}{T_1^{app}} = \frac{1}{T_1} + \frac{1}{T_1^{temp}} + \frac{f}{\lambda} \qquad or \qquad R_1^{app} = R_1 + R_1^{temp} + \frac{f}{\lambda} \tag{2.9}$$

T_1^{temp} (R_1^{temp}) is the contribution of temperature-dependent longitudinal relaxation time (rate) caused by brain temperature changed by physiological or pathological perturbation (see Supplemental Materials for details). Eq (2.8) is one type of differentiation equations and can be solved with the following solution:

$$\mathrm{M}_b(t) = e^{-\frac{t}{T_1^{app}}} \left[M_b^0 \cdot e^{\frac{t}{T_1^{app}}} - \frac{M_b^0 \cdot f}{\lambda \cdot (\frac{1}{T_1^{app}} - \frac{1}{T_{1a}})} e^{t(\frac{1}{T_1^{app}} - \frac{1}{T_{1a}})} + C \right] \tag{2.10}$$

where C is a constant. For the saturation-recovery T_1 experiment with the boundary condition of $M_b(t=0) = 0$, the final solution for Eq. (2.8) and Phase 1 when $t < t_{tran}$ becomes:

$$\mathrm{M}_b(0\text{-}t_{tran}) = M_b^0 \left[\left(1 - e^{-\frac{t}{T_1^{app}}} \right) - \frac{f}{\lambda \cdot (\frac{1}{T_1^{app}} - \frac{1}{T_{1a}})} \left(e^{-\frac{t}{T_{1a}}} - e^{\frac{t}{T_1^{app}}} \right) \right] = M_b^0 \left(A - B \right)$$

$$A = 1 - e^{-\frac{t}{T_1^{app}}}$$

$$B = \frac{f}{\lambda \cdot (\frac{1}{T_1^{app}} - \frac{1}{T_{1a}})} \left(e^{-\frac{t}{T_{1a}}} - e^{\frac{t}{T_1^{app}}} \right) \tag{2.11}$$

During Phase 2 the fully relaxed artery spins in the blood outside the saturation region flow into the rat brain, and they will approach the image plane and exchange with the brain tissue water spins when $t \geq t_{tran}$. Under this condition, $M_a = M_b^0/\lambda$, therefore, Eq. (2.5) can be written as:

$$\frac{dM_b(t)}{dt} = \frac{M_b^0 - M_b(t)}{T_1} + f\left[\frac{M_b^0}{\lambda} - \frac{M_b(t)}{\lambda}\right] \quad . \qquad (2.12)$$

To reorganize Eq. (2.12) and then combine it with Eq. (2.9) leads to:

$$\frac{dM_b(t)}{dt} + \frac{1}{T_1^{app}} \cdot M_b(t) = \frac{1}{T_1^{app}} \cdot M_b^0 \qquad (2.13)$$

Solving Eq. (2.13) with the initial condition using Eq. (2.11) with $t = t_{tran}$ gives:

$$M_b(t \geq t_{tran}) = M_b^0\left[1 - e^{-\frac{t}{T_1^{app}}} \cdot (1 - C_A + C_B)\right] \qquad (2.14)$$

where C_A and C_B are the constants which equal to A and B in Eq. (2.11), respectively, when $t = t_{tran}$. Therefore, when the saturation recovery time is shorter than t_{tran} (Phase 1), the magnetization of brain tissue relax following Eq. (2.11) whereas when the saturation recovery time is longer than t_{tran} it will relax according to Eq. (2.14) instead. It is clear that the brain magnetization recovery after the magnetization saturation preparation with a significant long saturation recovery time of $T_{SR} \geq t_{tran}$ (Phase 2) follows

a single exponential relaxation time T_1^{app} (see Eq. 2.14), while the magnetization recover in Phase 1 ($T_{SR}<t_{tran}$) in theory would be influenced by both T_1^{app} and T_{1a} (see Eq. (2.11)). Close examination of Eq. (2.11), we can see that the term of A in the equation only depends on T_1^{app} whereas the term B in the equations depends on both T_1^{app} and T_{1a}. We have conducted a simulation study using Eq. (2.11) for comparing the relative contributions of A and B terms (Figure 2.3) and turns out that term B in Eq. (2.11) is less than 4% compared with term A within a reasonable transit time range (100-500ms) in the rat brain [29, 62-64]. Therefore, a single exponential recovery according to term A is a good approximation for our rat study

Figure 2.3 Simulation results of B/A ratio in Eq.(2.11) as a function of artery transit time. Simulation parameters: T_1^{app} is 2.08 sec based on our study; T_{1a} = 2.38 sec taken from the literature [65]; f is 1ml/g/min and λ is 0.9ml/g.

at a short T_{SR} since the magnetization contribution of term B is negligible. In summary, a single exponential fitting of T_1^{app} based on a number of MRI SI measurements with varied

T_{SR} values presents a simple and quantitative relationship which links T_1^{app} or R_1^{app} to CBF (see Eq. (2.9)).

2.2.3 Imaging T_1^{app} , T_1^{CBF} and absolute CBF change (ΔCBF)

The T_1 and R_1 term in Eq. (2.9) represent the intrinsic brain tissue property of longitudinal relaxation time and rate, respectively; they are usually insensitive to physiological changes and can be treated as constants. The R_1^{app} difference between the reference and perturbed conditions becomes:

$$\Delta R_1^{app} = \Delta R_1^{\text{temp}} + \frac{\Delta CBF}{\lambda} \tag{2.15}$$

where $\Delta CBF = CBF_{PC} - CBF_{RC}$. Thus, absolute CBF change (ΔCBF) between perturbation and reference conditions can be calculated from the following equation:

$$\Delta CBF = \lambda \cdot (\Delta R_1^{app} - \Delta R_1^{\text{temp}}) = \lambda \cdot \Delta R_1^{CBF} \tag{2.16}$$

where ΔR_1^{CBF} presents the R_1 change, which is solely attributed to the absolute CBF change induced by perturbation; and it can be imaged by the SR-T_1 MRI method through three steps: i) image brain SI distribution as a function of T_{SR} during both control and perturbed conditions, and then determine the T_1^{app} values in each image pixel by the exponential regression of measured SI as a function of T_{SR} according to Eq. (2.1); ii) subtract the control R_1^{app} ($1/T_1^{app}$) value by the perturbed R_1^{app} value resulting in ΔR_1^{app}; iii) determine ΔT_1^{temp} and ΔR_1^{temp} caused by a brain temperature change induced by perturbation (see Supplemental Materials for details), then calculate ΔR_1^{CBF} and ΔCBF according to Eq. (2.16). The unit of CBF in Eq. (2.16) is ml/g/second, which can be converted to a conventional unit of ml/g/min by multiplying CBF by 60.

2.3 Materials and Experiment Design

2.3.1 Animal surgery and preparation

Twelve male Sprague-Dawley rats weighing 328 ± 35 g were used in this group of experiment. Thirty-six to 48 hours prior to the MRI experiments, the vertebral arteries of each rat were occluded by electrocoagulation [66]. Briefly, the second cervical vertebra was exposed by a midline incision and separation from the neck muscles. The fibers attached to the upper part of the first vertebra were cut to expose the transverse foramen at the lateral portion of the vertebra. An electrical cauterizer (Fine Science Tools Inc., Foster City, CA) was inserted into the foramen to coagulate the vertebral arteries passing underneath. The incision was then closed and the rat was allowed to recover from the surgery.

On the day of the MR experiment, the rat was anesthetized and intubated using 5% (v/v) isoflurane in N_2O:O_2 (60/40) gas mixture. Both femoral arteries and the left femoral vein were catheterized for physiological monitoring and blood sampling. The carotid arteries were exposed and two plastic vessel occluders (Harvard Apparatus, Holliston, MA) were placed around each of them. The wound was closed by suture. Five rats (Sub-group 1) were included for simultaneous MRI/LDF/temperature measurements. The LDF/Temperature instrument (Oxford Optronix, UK) was used to concurrently measure the percentage change of CBF, which can be converted to the relative CBF change that is defined as $rCBF=CBF_{PC}/CBF_{RC}$, and the brain temperature change in the cortical region in one hemisphere by inserting the LDF/Temperature probe (0.5 mm diameter) into the brain tissue through a small hole (3×3 mm^2) passing both skull and dura (1.5-4 mm

lateral, 1.5-3 mm posterior to the bregma, 1.9 mm deep). The soft tissue around the hole was kept to minimize magnetic susceptibility artifacts in MRI. After the surgical operation, the rat was placed in a home-built cradle incorporating ear bars and a bite bar to reduce head movement and to ensure proper positioning inside the MRI scanner. The animal anesthesia was maintained at 2% isoflurane. Rectal temperature was maintained at 37.0±0.5ºC by a circulating/heating water blanket, and the inspired and expired gases and blood pressure were monitored constantly. The rate and volume of ventilation were adjusted to maintain normal blood gases. All surgical procedures and experimental protocols were approved by the Institutional Animal Care and Use Committee of University of Minnesota.

2.3.2 MRI measurement

All MRI experiments were conducted on a 9.4T horizontal animal magnet (Magnex Scientific, Abingdon, UK) interfaced to a Varian INOVA console (Palo Alto, CA, USA). A butterfly-shape surface coil (long axis of 2.8 cm and; a short axis of 2.0 cm that is parallel to the animal spine) was used to collect all MRI data. Scout images were acquired using a turbo fast low angle shot (TurboFLASH) imaging sequence [67] with the following imaging acquisition parameters: TR = 10 ms, TE = 4 ms, image slice thickness = 2 mm, field of view (FOV) = 3.2 cm×3.2 cm; image matrix size = 128×128.

The magnetization saturation of water spin inside the rat brain was achieved by using the local B_1 field of the RF surface coil and the adiabatic 90º pulse (4 ms pulse width) followed by three orthogonal crush gradients with 3 ms length. Gradient-echo (GE)

EPI (TE = 21 ms; FOV = 3.2cm×3.2cm; image matrix size = 64×64; single slice coronal image with 2 mm thickness) combined with the saturation-recovery preparation was used to image T_1^{app} with seven T_{SR} values of 0.004, 0.1, 0.2, 0.3, 0.4, 0.5 and 10 s, which resulted in a temporal resolution of 11.9 s for obtaining one set of combined T_1^{app} and BOLD (i.e., when TR=10 s ≈ $5T_1$) images. This EPI imaging sequence was applied to: i) measure ΔR_1^{CBF} resulting from either hypercapnia (CBF increase) or acute ischemia (CBF reduction) compared to the control condition; ii) determine the relationship between brain temperature change and ΔR_1^{temp} immediately after the cardiac arrest (i.e. CBF=0) with a KCl bolus injection (see Supplemental Materials for details); and iii) determine ΔCBF values and then compare and correlate the values with the LDF measurement results.

2.3.3 Experiment protocol

2.3.3.1 Transient hypercapnia study

Mild transient hypercapnia was induced in eight of the twelve rats used in this study by ventilating the gas mixture of 10% CO_2, 2% isoflurane and 88% N_2O:O_2 (60/40) for 7 minutes; three of the eight rats were used for simultaneous measurements of ΔR_1^{CBF}, ΔCBF and BOLD using the SR-T_1 MRI method, and the percentage CBF (CBF/CBF_{RC}) and temperature (T) change using the LDF/Temperature probe; and other five rats were used to conduct the MRI experiments only.

2.3.3.2 Acute ischemia study

All twelve rats performed 1-minute occlusion of the two carotid arteries to achieve acute, global brain ischemia (i.e., four-blood-vessel-occlusion rat model) [68]. Five of

them were used for simultaneous measurements of ΔR_1^{CBF}, ΔCBF, BOLD, rCBF and brain temperature using the SR-T_1 MRI method and the LDF/Temperature probe, respectively.

The transient hypercapnia experiment was performed first, and then followed by the acute ischemia experiment with an adequately long waiting period between them. There was additional waiting time between the acute ischemia study and KCl injection for approaching cardiac arrest to ensure stable animal conditions prior to each perturbation. The SR-T_1 GE-EPI data were acquired for two minutes (5 repetitive image volumes per minute) prior to each perturbation of transient hypercapnia (7 minutes long), acute ischemia (1 minute long) or KCl injection for approaching cardiac arrest. This control (or prior-perturbation) imaging acquisition period is defined as Stage 1 (**S1**). The EPI data were collected for at least 14 minutes during and after each perturbation. The duration during either the transient hypercapnia (7 minutes) or acute ischemia (1 minute) perturbation is defined as the perturbation stage or Stage 2 (**S2**). Finally, the relatively long post-perturbation period was divided into three stages (i.e., Stage 3 or **S3**; Stage 4 or **S4** and Stage 5 or **S5**). Because the post-perturbation effects on CBF and BOLD responses were much shorter for the 1-minute acute ischemia perturbation than that of 7-minute transient hypercapnia perturbation, the durations for these three stages were different for these two perturbation studies: i) for the hypercapnia perturbation: 8 minutes for **S3**; 3.4 minutes for **S4** and 3.2 minutes for **S5**; and ii) for the ischemia: 2.4 minutes for **S3**; 1.4 minutes for **S4** and 1.2 minutes for **S5** (also see Figure. 2.4).

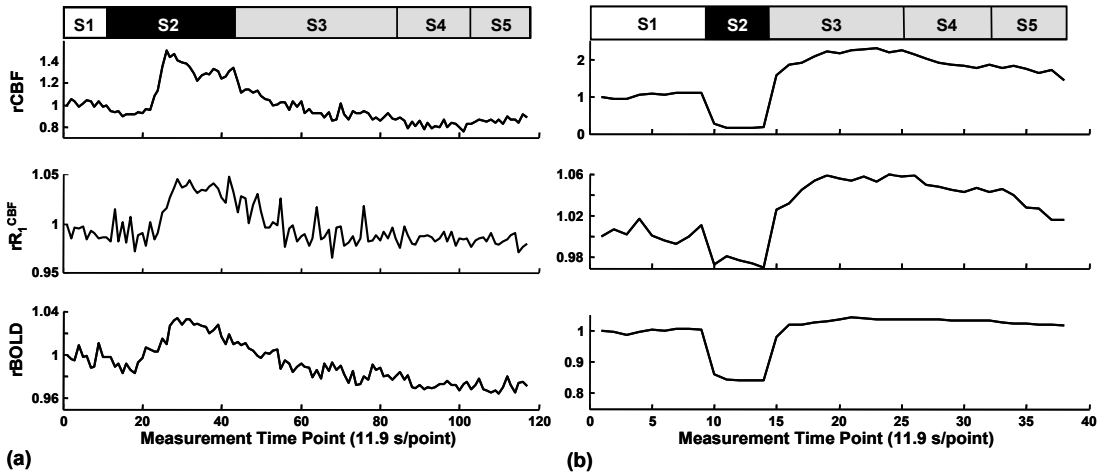

Figure 2.4 Time courses of relative R_1^{CBF} (i.e., rR_1^{CBF}) and relative BOLD (rBOLD) measured by the saturation-recovery-T_1 MRI method, relative CBF change (rCBF) measured by LDF before, during and after (a) hypercapnia and (b) ischemia perturbation from a representative rat (data extracted from a region of interest). The bar graphs on top indicate the experimental acquisition protocol of (a) hypercapnia and (b) ischemia. Five stages are defined for imaging acquisition under varied animal conditions. Stage 1 (S1) represents the control (or prior-perturbation) period (2 minutes) prior to the induction of each perturbation (i.e., hypercapnia, ischemia). Stage 2 (S2) represents the perturbation period either for the transient hypercapnia (7 minutes) or acute ischemia (1 minute). Stages 3, 4 and 5 (S3, S4 and S5) represent the three post-perturbation periods with varied time duration after either the transient hypercapnia or acute ischemia perturbation.

2.3.4 Data analysis

MRI data analysis was performed using the STIMULATE software package (Stimulate, Center for Magnetic Resonance Research, University of Minnesota, USA) [69] and the Matlab software package (The Mathworks inc., Natick, MA, USA). LDF data was sub-sampled to match the corresponding MRI sampling rate and processed with home-written Matlab programs. Both region of interest (ROI) and single pixel MRI data taken from the rat sensory cortical region were used to perform the T_1^{app} regression

analysis and to determine ΔR_1^{app}, ΔR_1^{temp} (see Supplemental Materials for details) and ΔCBF according to Eq. (2.15) and Eq. (2.16). The least-square nonlinear curve fitting program using the Matlab software was applied to perform the T_1^{app} regression analysis. The regression accuracy was estimated by the sum squared error (sse) and the square of regression coefficient (R^2).

To improve the quantification accuracy, the EPI data were averaged within each stage as defined above and then applied to calculate the values of ΔR_1^{app}, ΔR_1^{temp} and ΔCBF based on the transient hypercapnia or acute ischemia measurements. The control CBF value (CBF_{RC}) was further estimated from the averaged ΔCBF values and its corresponding percent CBF changes measured by LDF under ischemia condition and during the reperfusion period after the acute ischemia. ROIs (ranging from 24 to 52 pixels) were chosen from the rat cortical brain region in the hemisphere with the location being approximately contralateral to the LDF recording side for those experiments performing simultaneous MRI and LDF/Temperature measurements in order to avoid the MRI susceptibility artifacts caused by the LDF/Temperature probe. The GE-EPI data acquired with a long T_{SR} of 10 s (i.e., $\approx 5T_1$) were used to calculate BOLD according Eq. (2.3).

The R_1^{app} images at the control stage and a series of ΔCBF and BOLD images measured during and post hypercapnia and/or ischemia stages were created on a pixel by pixel basis (pixel size 0.25×0.25×2 mm^3, with nearest neighbor interpolation) with two-dimensional median filtering and then overlapped on the anatomic image.

Paired t-test was applied to compare the T_1^{app} values measured at reference and perturbation conditions obtained from either ROIs or single pixel shown in Figure 2.5, as well as to compare the regressed T_1^{app}s using ROI or single pixel data under a given condition.

2.4 Results

2.4.1 Reliability and sensitivity of T_1^{app} measurement and regression

The averaged T_1^{app} value measured in the rat cortex region under the normal physiological condition was 2.30±0.03 s (n=12) from the SR-T_1 measurements at 9.4T. Figure 2.5 demonstrates a representative SR-T_1 GE-EPI measurement and the T_1^{app} regression results based on ROI (Figure 2.5a) and single pixel (Figure 2.5b) data analysis from a single SR-T_1 MRI volume measurement without signal averaging measured under control, hypercapnia and ischemia condition, respectively. All the experimental data fitted well with an exponential function ($R^2 \geq 0.99$ and sse $< 2\times10^{-4}$). The individual T_1^{app} regression curves and the fitted T_1^{app} values measured under control, hypercapnia and ischemia conditions were distinguishable; and the results between the ROI and single pixel data analyses were consistent (see Figures 2.5a and 2.5b). For instance, no statistical difference was found between the T_1^{app} values obtained from the ROI analysis versus single pixel analysis under either the hypercapnia ($p = 0.93$, 12 image volumes using paired t-test) or the ischemia ($p = 0.83$, 5 image volumes using paired t-test) condition. These results reveal a high reliability of the proposed MRI method for imaging T_1^{app} and its change down to the pixel level, and this ability is crucial in generating reliable T_1^{app}

maps. Moreover, the determined T_1^{app} values under the hypercapnia and ischemia perturbations were statistically different from the control T_1^{app} value ($p<0.01$), indicating that the T_1^{app} relaxation process is sensitive to the perfusion changes induced by physiology/pathology perturbations.

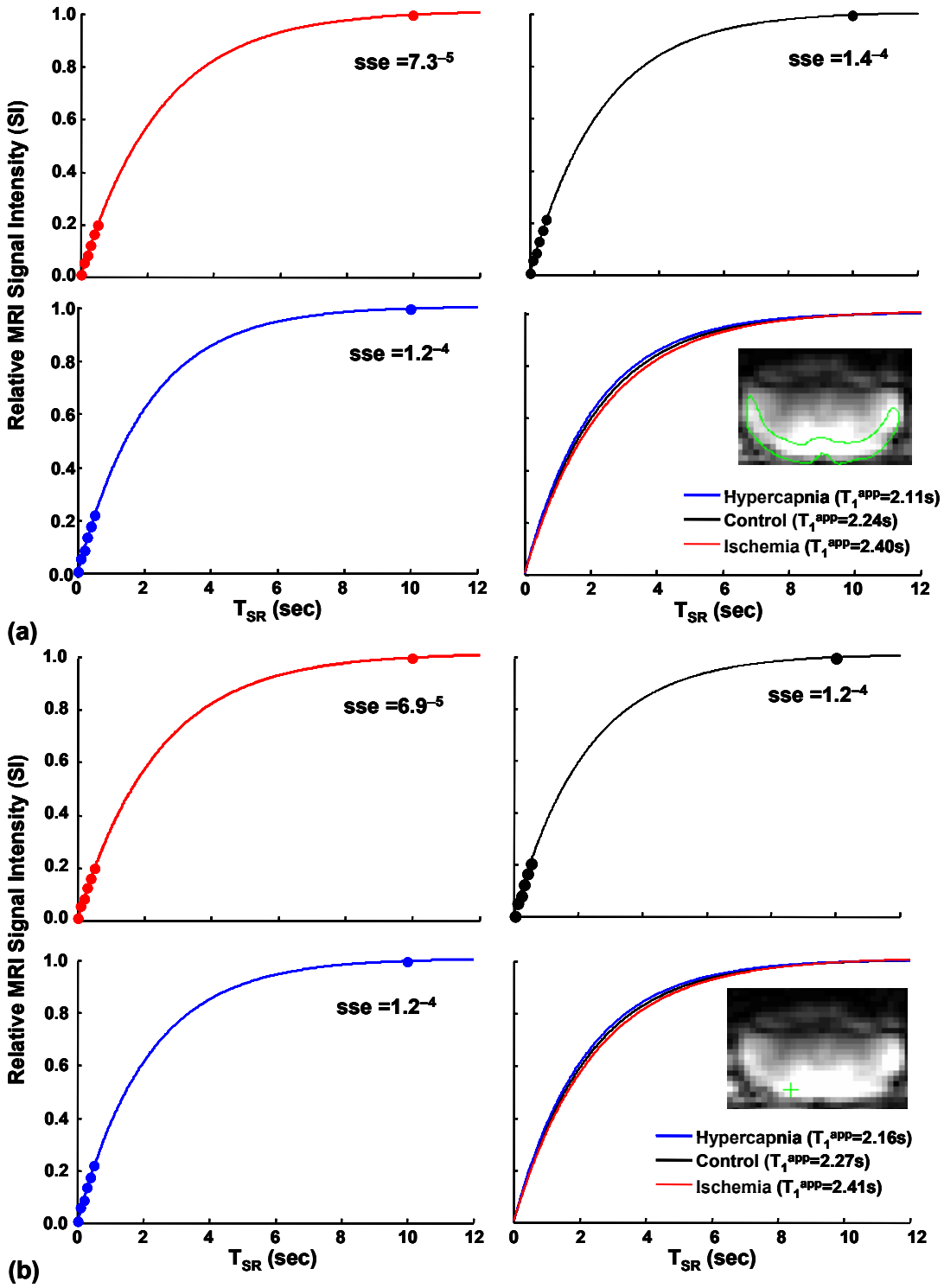

Figure 2.5 Time courses from a single saturation-recovery-T_1 GE-EPI measurement and T_1^{app} regression under control (black symbols and lines); hypercapnia (blue symbols and lines); and ischemia (red symbols and lines) conditions based on (a) ROI and (b) single EPI pixel located inside the rat brain cortex. Three T_1

fitting lines and their T_1 values under three conditions are also displayed in (a) and (b). The inserts show a coronal brain GE-EPI from a representative rat, indicating the location of (a) the ROI (enclosed in the green line) and (b) a single pixel (green cross mark) used for the regression (sse stands for the sum squared error; $R^2 = 0.99$).

2.4.2 Relationships between rCBF, relative R_1^{CBF} and BOLD induced by perturbations

Figure 2.4 shows the high temporal resolution (~12 s per data point) time courses of relative R_1^{CBF} (rR_1^{CBF}) and rBOLD measured by the SR-T_1 MRI method from the ROI located in the rat sensory cortex and rCBF measured by LDF before, during and after (a) the transient hypercapnia and (b) acute ischemia perturbation from a representative rat. Despite some fluctuations, these time courses displayed expected temporal behaviors. First, there are approximate parallel trends among all of the measured time courses. Secondly, the transient hypercapnia led to significant increases in the measured parameters owing to the vascular dilation effect followed by a recovery back to the baseline level after the termination of hypercapnia. Thirdly, the acute ischemia caused rapid reductions in all measured parameters followed by a substantial overshooting after the termination of ischemia and a slow recovery to the baseline level. Nevertheless, a careful examination of Figure 2.4 suggests a much stronger temporal correlation between the measured rR_1^{CBF} and rCBF compared to the correlation of rBOLD versus either rR_1^{CBF} or rCBF. Specifically, rBOLD shows a more significant undershoot after the hypercapnia (Figure. 2.4a) and a smaller overshooting after the ischemia than that of rR_1^{CBF} and rCBF (Figure. 2.4b). These results reveal the feasibility of the SR-T_1 MRI method to

simultaneously measure BOLD and rR_1^{CBF} which is tightly correlated to the CBF change; and its ability to temporally dissociate their responses with relatively high temporal resolution. It is also interesting to note that the rR_1^{CBF} time course had a relatively large fluctuation compared to the BOLD time course, presumably owing to a moderately low inherent contrast-to-noise ratio to measure the CBF change.

During the ischemia perturbation, R_1^{CBF} decreased 4.7±1.2% (n=5) compared to the control condition, which was equivalent to a 5.1±1.4% increase of ΔT_1^{CBF}; accordingly, CBF decreased 89.5±1.8% and BOLD decreased 23.1±2.8%. During the hypercapnia, in contrast, R_1^{CBF} increased 5.1±0.8% (n=3); ΔT_1^{CBF} decreased 4.8 ± 0.7%; CBF increased 82±12%; and BOLD increased 4.5±2.7%.

Figure 2.6 shows the plots of ΔR_1^{CBF} versus rCBF-1 (Figure 2.6a) and versus rBOLD-1 (Figure 2.6b) measured for the ischemia study. It shows an excellent consistency and strong linear correlation between the CBF change and ΔR_1^{CBF} across all five stages studied; and the correlation can be described by the following numerical equation which was obtained by the linear regression:

$$(\text{rCBF-1}) = 45.9 \times R_1^{CBF} + 0.01 \qquad (2.17)$$

with R^2=0.99. Whereas, two distinct linear fitting slopes (slope ratio = 2.6) were observed between ΔR_1^{CBF} and rBOLD-1, indicating the independence of the SR-T_1 MRI method for simultaneously determining ΔR_1^{CBF} and BOLD; and showing the decoupled changes of these two parameters during the post-ischemia stages.

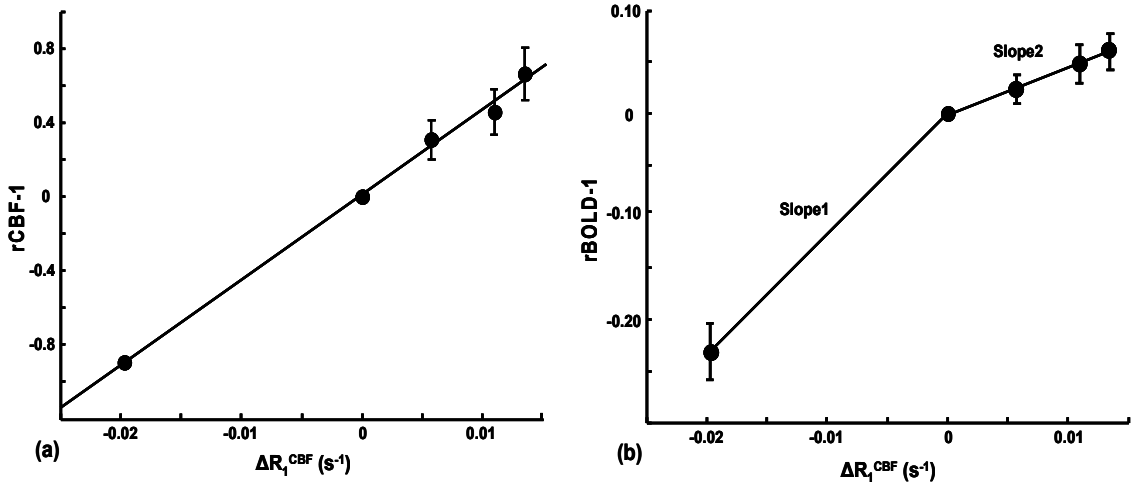

Figure 2.6 Correlation between the averaged ΔR_1^{CBF} measured by the saturation-recovery-T1 MRI method versus (a) rCBF-1 and (b) rBOLD-1 obtained during the five stages of ischemia experiment. The vertical bars indicate the standard error (SE) (n=5). There is a strong, positive correlation between (rCBF-1) and ΔR_1CBF in (a). In contrast, there are two distinct linear fitting slopes between (rBOLD-1) and ΔR_1^{CBF} in (b) owing to the mismatched change between them during the post-ischemia stages.

Table 2.1 summarizes the results of simultaneous rCBF (by LDF) and ΔR_1^{CBF} measurements (by the SR-T_1 MRI method) during the ischemia and the first post-ischemia period (Stage 3 or **S3**) for each rat and averages among inter-subjects. The ΔR_1^{CBF} value was used to calculate the absolute CBF change (ΔCBF) according to Eq. (2.13), and then rCBF and ΔCBF were applied to estimate the absolute control CBF (i.e., CBF_{RC}) according to the following relationship:

$$CBF_{RC} = \Delta CBF/(rCBF-1). \quad (2.18)$$

It was found that ΔCBF reduced 1.07±0.24 ml/g/min (n=5) during the ischemia and increased 0.73±0.17 ml/g/min during the first post-ischemia stage (Stage 3 or **S3**), corresponding to a CBF reduction of 90±2% and a CBF increase of 66±14%, respectively.

The estimated CBF_{RC} was 1.19±0.27 ml/g/min calculated from the ischemia stage (Stage 2 or **S2**) data, and 1.24±0.31 ml/g/min calculated from the first post-ischemia stage (**S3**) data, showing a good consistency between them. The estimated control CBF values in this study are coincident with the reported values in the literature ranging from 0.9 to 1.5 ml/g/min (1.29±0.05 ml/g/min) measured in the rat cortex using either the autoradiography (a "golden standard" approach) or ASL approaches under similar isoflurane anesthesia condition, which are summarized in Table 2.2. Furthermore, if we approximate the small interception value of 0.01 to 0 in Eq. (2.17) and replace (rCBF-1) term in Eq. (2.18) with the slope of Eq. (2.17), we get $CBF_{RC} = (60\text{sec/min}) \cdot \lambda(\text{ml/g})/45.9(\text{sec}) = 1.18$ ml/g/min using the relationship of Eq. (2.16). This value based on the regressed slope of 45.9sec using the data shown in Figure. 2.6a is again in good agreement with the averaged literature value of 1.29±0.05 ml/g/min. These comparison results provide abundant of evidence supporting the feasibility, as well as the reliability, of the proposed SR-T_1 MRI method in measuring the absolute CBF changes induced by physiological/pathological perturbations.

Table 2.1 Summary of ΔR_1^{CBF}, calculated absolute CBF change based on ΔR_1^{CBF} and (rCBF-1) measured with LDF during the ischemia (Stage 2) and the first post-ischemia stage (Stage 3); and the estimated baseline CBF under the reference control condition. (mean ± SEM; n=5)

	Ischemia Stage (Stage 2)				Ischemia overshooting stage (Stage 3)			
No.	ΔR_1^{CBF} (s^{-1})	Calculated ΔCBF (ml/g/min)	rCBF-1	Control CBF (ml/g/min)	ΔR_1^{CBF} (s^{-1})	Calculated ΔCBF (ml/g/min)	rCBF-1	Control CBF (ml/g/min)
1	- 0.023	-1.247	-0.883	1.413	0.014	0.751	0.332	2.263
2	-0.036	-1.928	-0.899	2.145	0.024	1.280	1.104	1.159
3	-0.014	-0.778	-0.924	0.841	0.016	0.880	0.597	1.474
4	-0.012	-0.664	-0.833	0.798	0.006	0.346	0.834	0.415
5	-0.013	-0.713	-0.938	0.760	0.007	0.389	0.445	0.874
Mean	-0.020± 0.004	-1.07± 0.24	-0.90± 0.02	1.19 ± 0.27	0.013± 0.003	0.73± 0.17	0.66± 0.14	1.24± 0.31

Table 2.2 Summary of the literature cited CBF results measured in the isoflurane anesthetized rat under normal physiology condition.

Cited literature Author, and year	Concentration of isoflurane(%)	Method of CBF measurement	CBF (ml/g/min) value at normal physiology condition
Young et al, 1991,	1.38	autoradiography	1.17(cortex and subcortex)
Frietsch et al, 2000	1.2	autoradiography	1.3-1.4(cortex and subcortex)
Machensen et al, 2000	1.4	autoradiography	1.5(cortex)
Todd et al, 1996	1.6-1.8	^{3}H-nicotine tracer	1.37 (whole brain)
Hansen et al, 1988	1.2	autoradiography	1.47-1.54 (cortex)
Lenz et al, 1998	1.4	autoradiography	1.09-1.35(whole brain)
	2.8	autoradiography	1.25-1.55(whole brain)
Kim et al., 2007	1.3-1.5	ASL	1.5 ± 0.18(somatosensory cortex)
Shen et al., 2005	1.1-1.2	ASL	1.2 ± 0.7(whole brain)
Sicard et al., 2005	1.15-1.25	ASL	1.10 ± 0.04(motor cortex)
Liu et al., 2004	1.1-1.2	ASL	0.91± 0.13(somatosensory cortex)
Wegener et al., 2007	1.5	ASL	~1.19 (sensory and auditory cortex)
Mean±SE			1.29 ± 0.05

Figure 2.7 shows the control R_1^{app} images of rat brain (coronal orientation), anatomic image, and the ΔCBF and BOLD images (pixel size = $0.25\times0.25\times1mm^3$) measured by using the SR-T_1 MRI method during and after the hypercapnia/ischemia perturbation in a representative rat without the use of LDF probe to avoid the susceptibility MRI artifacts. It illustrates that the SR-T_1 MRI method is robust and sensitive in noninvasively imaging the absolute CBF changes in response to physiological (hypercapnia) or pathological (ischemia) perturbations with a few minutes of image acquisition time. Moreover, the BOLD images can also be simultaneously obtained.

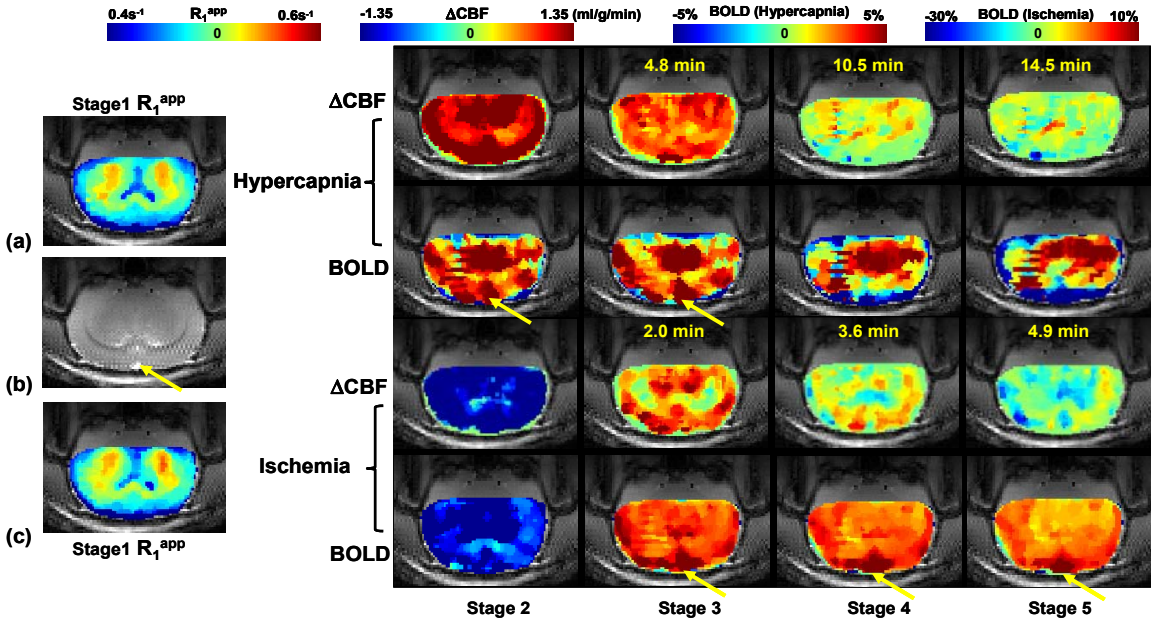

Figure 2.7 (a) and (c) Control R_1^{app} images (S1); ΔCBF and BOLD images obtained from (a) hypercapnia and (c) ischemia study, respectively, during Stages 2 to 5. (b) Anatomic coronal image of a representative rat brain. The time indicated above is the image sampling time after the termination of Stage 2 (S2). The yellow arrows point to the sinus vessel. The total image averaging time for Stages 2 to 5 (i.e., S2, S3, S4 and S5) were: 2.5, 6.5, 4.6 and 3.2 minutes for the hypercapnia study; and 1.0, 1.8, 1.4 and 1.2 minutes for the ischemia study.

2.5 Discussion

2.5.1 Underlying mechanism for imaging absolute CBF change in rat brain using the SR-T_1 imaging method

Instead of focusing the magnetization change by delivering tagged spins to the image in ASL approach at a certain T_{IR}, T_1 perfusion model [33, 37, 38] views CBF as an enhanced longitudinal relaxation through T_1^{app} defines in Eq. (2.9). The rapid exchange between the water protons in the image slice within the saturation region and the fully

relaxed arterial blood water outside of the saturation region during the SR-T_1 measurement enables a link between T_1^{app} and CBF. Based on the current MR acquisition in this study, Eqs. (2.11) (valid for Phase 1, when $T_{SR} < t_{tran}$) and (2.14) (valid for Phase 2 when $T_{SR} \geq t_{tran}$) quantitatively describes the magnetization change as a function of T_{SR} for the SR-T_1 measurement in a two-phase model shown in Figure 2.2. According to Eq. (2.11), the brain tissue relaxation depends on both T_1^{app} and T_{1a} when $T_{SR} < t_{tran}$, however, the term B in Eq. (2.11) which contains T_{1a} accounts for only few percentages of term A and its contribution is insignificant. When $T_{SR} \geq t_{tran}$ and according to Eq. (2.14), the brain tissue magnetization relaxation solely follows T_1^{app}. Therefore, T_1^{app} dominates the magnetization change through the entire T_{SR} and could link to CBF changes. The excellent T_1^{app} fitting curve (as well as the linear semi-log fitting, data not shown here), reproducibility and sensitivity shown in Figure 2.5 demonstrate that single exponential function regression worked well in this study. Moreover, the excellent correlation between ΔR_1^{CBF} measured with the SR-T_1 method and relative CBF change recorded by LDF technique (Figures 2.4 and 2.6) during physiological/pathological perturbations, and the coincidence of the calculated baseline CBF results with the reported CBF values in the literature reveals that ΔR_1^{CBF} measured with SR-T_1 method actually reflects true CBF changes. The difference between the blood and brain tissue longitudinal relaxation times is small at 9.4T and the single-exponential recovery model is a reasonable assumption. This simplification improves the accuracy of T_1^{app} measurement. For instance, the averaged T_1^{app} value based on the SR-T_1 measurements in the rat brain cortex was 2.30 s in this study. The blood T_1 (T_1^{blood}) can be estimated using an established equation of

T_1^{blood} = 0.129×B_0+1.167 with the unit of second [65], resulting in T_1^{blood} ≈ 2.38 s at B_0=9.4T. Finally, T_1^{app} can possibly be influenced by other than parameters, for example, temperature induced T_1 change besides intrinsic T_1 and CBF. Although T_1^{app} corrected with T_1^{temp} is more accurate than T_1^{app} without any correction, T_1^{app} still provide a good approximation to calculate CBF change (see Supplementary Materials).

It would be very interesting to examine whether the CBF perturbation induced ΔR_1^{app} still exists by applying the whole body saturation with a volume coil. The disappearance of ΔR_1^{app} is expected if the "spin labeling" mechanism dominates the magnetization process when whole body saturation is employed because the intrinsic T_1 would be measured instead of T_1^{app}. Otherwise mechanisms other than spin labeling need to be considered. CBF change measured by SR-T_1 method has been validated with simultaneous LDF technique in the current study, we would also like to further compare it with ASL technique.

2.5.2 Advantages, limitations and technical methodology aspects of SR-T_1 method for imaging absolute CBF

Noninvasive, quantitative and reliable neuroimaging techniques capable of imaging CBF and its change are desirable for investigating brain physiology, functional activity and pathology progression related to numerous brain diseases. The SR-T_1 MRI method described herein reliably maps both the absolute CBF change and BOLD signal simultaneously with relatively high spatial (0.5mm×0.5mm in-plane resolution) and temporal (~12 sec per combined ΔCBF and BOLD images) resolutions. In comparison

with the conventional ASL techniques using an inversion-recovery preparation, the SR-T_1 MRI method has several unique merits. First, the modeling used to quantitatively link T_1^{app} and CBF in the SR-T_1 MRI method is simple and it requires much less physiological parameters to quantify absolute ΔCBF according to Eq. (2.16). Secondly, the SR-T_1 MRI method relies on parametric T_1^{app} mapping; thus, it does not require the paired control image as applied in most ASL methods for determining CBF change. Thirdly, the saturation-recovery preparation avoids the requirement of relatively long TR constrained by the conventional ASL methods based on the inversion-recover preparation, and enables relatively rapid mapping of T_1^{app} and ΔR_1^{app} to generate the ΔCBF image as illustrated in Figure 2.7. Although the imaging of T_1^{app} requires multiple measurements with varied T_{SR} values, its temporal resolution of 12 s per complete image set is compatible with other ASL methods (approximately 5-10 s).

The ΔR_1^{CBF} and ΔCBF values measured by the SR-T_1 MRI method are correlated linearly with the CBF percentage changes measured independently but simultaneously by LDF recording during ischemia and post-ischemia periods. Furthermore, the estimated control CBF_{RC} value is coincident with the reported value in the literature. These results validated the SR-T_1 MRI method, and demonstrated both the feasibility and sensitivity of this method for imaging the absolute CBF change induced by physiological/pathological perturbation. Although this study was based on single slice measurement to prove the concept and feasibility of the proposed SR-T_1 MRI method, it should be readily extended to multiple image slices covering a much larger brain volume.

One technical limitation of the current SR-T_1 MRI method is its inability to directly measure the absolute CBF value under a physiological condition of interest, thus the control value of CBF_{RC} was indirectly estimated by two independent measurements of ΔCBF and rCBF using the SR-T_1 MRI method and LDF, respectively, in this study.

A surface coil generates an inhomogeneous B_1 distribution in space, resulting in a non-uniform RF pulse flip angle for saturating the water magnetization if a conventional RF pulse is used. In this study, we applied an adiabatic half passage 90^o RF pulse to achieve relatively uniform 90^o rotation of M_z into the transverse plane and to improve saturation efficiency, in particular, in the brain cortical region where B_1 is strong. The ROI for data processing was chosen from this region (see Figure 2.5). In the deep brain region, distant from the surface coil, it might not be warranted to approach an adiabatic 90^o rotation if the RF power is inadequate in this brain region. As a result, the RF saturation efficiency ($0 \le \alpha \le 1$) can drop in the deep brain region and lead to relatively low saturation efficiency. However, this imperfection, if it exists, should not cause a significant error in determining T_1^{app} due to the following two reasons.

First, the term of α was considered in the least square regression to calculate the T_1^{app} value using the following formula:

$$\begin{aligned} SI &= SI_0 e^{-\frac{TE}{T_2^*}}\left(1 - \alpha e^{-\frac{T_{SR}}{T_1^{app}}}\right) \\ &= K\left(1 - \alpha e^{-\frac{T_{SR}}{T_1^{app}}}\right) \end{aligned} \qquad (2.19)$$

in which three constants, K, α and T_1^{app} are determined by regression. Though α can become less than 1 in the deep brain region if B_1 strength is inadequately strong, it can be treated as a constant. The T_1^{app} regression becomes insensitive to the absolute

value of α; the regression outcome is mainly determined by the exponential rate of SI recovery as a function of T_{SR}.

Secondly, a nominal 90^o excitation pulse and a very short TE were used in the GE-EPI sampling in this study. In addition, there was no extra delay between the EPI signal acquisition and the next RF saturation pulse. This configuration further eliminates the residual M_z component before the next magnetization saturation preparation. It acts as extra magnetization saturation, resulting in an improved saturation efficiency and insensitivity to the value of α. These notions are supported by the ΔCBF images (Figures 2.7b and 2.7c) showing relatively uniform CBF changes across the entire image slice. In contrast, the BOLD images show the 'hot' spots around the sinus vein as pointed by the arrows in Figure 2.7 because of the large BOLD effect near a large vein [57]. Such 'hot' spots were not observed in the ΔCBF images, indicating that the ΔCBF image is more specific to the tissue perfusion and less susceptible to macro vessels. This differentiation between the simultaneously measured BOLD and ΔCBF images suggests that the SR-T_1 MRI method indeed is able to independently but simultaneously measure two important physiological parameters of absolute CBF change and BOLD. Although, there is a similar trend between the measured changes of ΔCBF and BOLD during ischemia or hypercapnia perturbation as shown in this study, there are clearly distinct characters in both spatial distribution and temporal behavior between the ΔCBF and BOLD images during the recovery periods after the perturbations, which provide complementary information of the brain hemodynamic changes in response to physiological/pathological perturbations.

2.5.3 Relationship between ΔR_1^{CBF} and the absolute CBF change during ischemia and hypercapnia

It is known that the development of vasogenic edema usually occurs at a later phase, approximately 30 minutes after the induction of regional ischemia [70]; and the water accumulation in the ischemia tissue owing to cellular swelling takes place hours after the onset of ischemia [71, 72]. It is unlikely that vasogenic edema and water content change could be responsible for the measured ΔR_1^{CBF} change in the present study since the global ischemia lasted only one minute and the SR-T_1 MRI measurements were continued within a relative short period during the post-perturbation stages. Therefore, ΔR_1^{CBF} imaged by the SR-T_1 MRI method could be fully quantified to determine and image ΔCBF. This notion is evident from the results of the ischemia study; and it also holds true for the hypercapnia study. However, it would be interesting to investigate the longitudinal T_1^{app} change in the ischemic brain region, which could be affected by the CBF change and possibly other characteristic changes (infarction, edema, necrosis etc.) of brain tissue. Further study of their relative contributions to the T_1^{app} change would be very helpful to understand the evolution of the ischemic lesion and its relationship with CBF.

A similar estimation using the relationship of rCBF and ΔCBF measured during the hypercapnia (Stage 2) resulted in the CBF_{RC} value as 1.45±0.05 ml/g/min (n=3). This value is very close to that calculated with during the ischemic/postischemic stages (≈1.2 ml/g/min) although they are not exactly the same. The slight discrepancy might be due to the basal CBF drifting through the prolonged period of experiment time because these experiments (hypercpania and ischemia) were combined. It also could be related to the

limited samples of hypercapnia experiments. Nevertheless, ΔCBF increase induced by hypercapnia calculated from ΔR_1^{CBF} correlates well with rCBF measured by LDF.

2.5.4 Correlation of R_1^{CBF}, CBF and BOLD during perturbations

Beside the aforementioned distinction of spatial responses between the ΔCBF and BOLD images owing to the different specificity to the hemodynamic response with varied vessel size, it is interesting to note that there were significantly mismatched temporal responses between measured ΔCBF and BOLD during both post-ischemia and post-hypercapnia stages. The "overshooting" effect was much less for BOLD than the ΔCBF and rCBF responses during the post-ischemia stage (Figure 1.4b), leading to two distinct slopes of linear regression between rBOLD and ΔR_1^{CBF} (Figure 2.6b). There was also a substantial "undershooting" in the measured BOLD change during the later post-hypercapnia recovery stages (Figure 2.4a) compared to rCBF. One explanation for this observation is that BOLD signal reflects a complex interplay among cerebral blood flow, blood volume (CBV) and oxygen consumption rate ($CMRO_2$) [57, 58]. Therefore, BOLD can become dissociated with the CBF change, and degree of the mismatched BOLD and ΔCBF relies on the fractional changes in CBF, CBV and $CMRO_2$ in response to particular perturbation. The quantitative interpretation of the mismatched rCBF-rBOLD behavior requires additional measurements of CBV and $CMRO_2$, which is beyond the scope of this article. Nevertheless, this mismatch could be linked to the uncoupling between the metabolic and hemodynamic responses associated with a physiology or pathology perturbation, and it should be useful for indirectly estimating the $CMRO_2$ time course

during the perturbation if the CBV change can be measured independently or estimated using a sophisticated BOLD modeling (e.g., [73]).

A local RF coil, such as a surface coil as used in the present study, has been commonly applied for most *in vivo* animal MRI/MRS studies. Its local RF B_1 field provides regional longitudinal magnetization changes through saturation (or inversion) preparation prior to the EPI acquisition. The combination of regional M_z preparation and relatively short blood travel time from the non-saturated region into the EPI slice in animal brains is the underlying mechanism for a quantitative link between ΔCBF and ΔR_1 that can be robustly imaged by the SR-T_1 MRI method. On the other hand, the T_1 or T_1-weighted MRI signal changes commonly observed in the clinical imaging diagnosis, for instance, stroke patients, are at least partially attributed by the perfusion change, i.e., ΔCBF. Finally, the SR-T_1 MRI method can be combined with a volume RF coil for imaging ΔCBF if a slice-selective saturation preparation can be implemented.

2.6 Conclusion

In summary, we have described the SR-T_1 MRI method for noninvasively and simultaneously imaging the absolute CBF change and BOLD in response to physiological/pathological perturbations. This imaging method was validated in the rat brain with simultaneous LDF measurements under global ischemia and hypercapnia conditions. This imaging method should provide a robust, quantitative MRI-based neuroimaging tool for simultaneously measuring the CBF change and BOLD contrast

associated with physiological perturbations (e.g., brain activation) or pathological perturbations (e.g., stroke or pharmaceutical drug treatment).

CHAPTER 3 Will Large Vessel Inflow Effect and Arterial Transit Time Significantly Contaminate the CBF Change Imaging Using the SR-T_1 Method?

3.1 Introduction

The feasibility for imaging and quantifying absolute change of cerebral blood flow (CBF) using saturation-recovery(SR) T_1 MRI approach has been previously demonstrated using rat ischemia (decreasing CBF) and hypercapnia (increasing CBF) models at 9.4T [74] . Briefly, the water exchange between the capillary and brain tissues through the blood perfusion will affect the apparent water T_1^{app}, thus, its change can be applied to determine the CBF difference (ΔCBF) between control condition and CBF perturbed condition.

Two general confounding factors of quantifying absolute CBF with arterial spin labeling (ASL) techniques are the large vessel inflow effect and arterial transit time. The former confounding factor refers to the tagged spins in an artery within a voxel before they enter a capillary bed in another region should not be counted as perfusion in that voxel. For example, pulsed arterial spin labeling (PASL) experiments like flow sensitive alternating inversion recovery (FAIR) technique with short TI often show focal bright spots in arteries because there has not been sufficient time for the tagged spins to reach the brain parenchyma [32]. This effect can be partially reduced by inserting a delay after

the tagging pulse, like quantitative imaging of Perfusion with a single subtraction, version II(QUIPSS II) and continuous arterial spin labeling (CASL). [29, 35, 75] The effect can also be reduced by applying bipolar diffusion gradients to destroy the signals from large vessels. The arterial transit time (or delay) refers to the time the tag spins need to travel from tagging region to the image voxel. It varies even within the same image slice. The longer the transit delay is, the less efficient the ASL will be because many of the tagged spins have not reached the voxel by the time of the image.

Since SR-T_1 method of imaging CBF change shares the similar mechanisms with ASL, the above mentioned two confounding factors potentially could also contaminate the CBF change measured by SR-T_1 method. In this present study, we try to answer two questions: 1) whether the large vessel inflow effect could contribute to T_1^{app}/R_1^{app} quantification and therefore affect CBF change measurement? 2) whether the arterial transit time of blood flow could significantly bias the T_1^{app}/R_1^{app} measurement for determining CBF change in rat brain? Two experiments were designed to address these questions. One was the use of bipolar diffusion gradient to suppress the large-vessel inflow effect, by thus comparing the R_1^{app} values as well as its difference (ΔR_1) with and without diffusion gradients. The other was using varied slab thickness saturation preparation to spatially manipulate blood transit distance, by thus testing the effect of blood transit time on the T_1^{app}/R_1^{app} and ΔCBF measurement.

3.2 Theory

Several studies have demonstrated that the diffusion-weighted MRI with an adequate diffusion gradient strength has the characteristic of selectively attenuating the fMRI signal generated by moving spins in both arterial and venous sides, therefore more closely reflecting the capillary beds responses. As a result, it is believed that diffusion-weighted images help to improve the spatial and temporal accuracy for mapping neuronal activation [76-79]. The degree of the attenuation (A) on the measured GE-EPI signal can be quantified by:

$$A(D) = \exp(-b \cdot D) \tag{3.1}$$

where D is the diffusion coefficient constant, and b is the diffusion-weighting factor that incorporates the amplitude and timing parameters of the diffusion gradients according to:

$$b = (\gamma \cdot G \cdot \delta t)^2 \cdot (T - \delta t / 3) \tag{3.2}$$

where γ is the gyromagnetic ratio; G and δt are the magnitude and duration of diffusion gradient; T is the time delay between the bipolar diffusion gradients.

Since a large b factor tends to significantly suppress the MRI signal contribution from large vessels with rapid blood flow velocity [77, 80, 81], the measured fMRI signal becomes more dominant by smaller arterioles, capillaries and brain tissue. Moreover, it has been demonstrated that the fMRI signal acquired at high magnetic field with high b factors (>1000 s·mm^{-2}) with a relative long TE tended to eliminate most large vascular contributions, and thus extravascular (or tissue) component becomes a dominant contribution. In the present study, a large b factor up to 1019 s·mm^{-2} was applied to

measure diffusion-weighted GE-EPI data under normocapnia and hypercapnia conditions at 9.4T.

3.3 Material and MRI Method

The MRI experiments were carried out in a horizontal 9.4T animal magnet with an 8-shape surface coil (2.8cm×2cm). Ten male Sprague-Dawley rats (W=345±36g) were used for conducting twenty hypercapnia experiments for testing large vessel inflow effect using diffusion-weighting MRI. Another group of six male (W=355±40g) rats with nine occurrences of hypercapnia were used to investigate the arterial transit time (by varying the thickness of saturation preparation band) influence to the absolute CBF change quantification with SR-T_1 method. The animal anesthesia was maintained at 2% isoflurane. The hypercapnia was induced by switching to an inhalation bag with mixed gases (6% CO_2, 34% O_2, 58% N_2O and 2% isoflurane) for 20-30 minutes. All the R_1^{app} image measurements were acquired before (i.e., normocapnia or control) and during stable hypercapnia condition, when the animal physiology (monitored during the entire experiment) was within normal ranges. The Institutional Animal Care and Use Committee of University of Minnesota approved all surgical procedures and experimental protocols.

Scout images were acquired using a turbo fast low angle shot (TurboFLASH) imaging sequence with the acquisition parameters: TR = 10 ms, TE = 4 ms, image slice thickness = 1 mm, field of view (FOV) = 3.2 cm×3.2 cm; image matrix size = 128×128. Gradient echo EPI (TE=21ms; FOV=3.2×3.2cm; image matrix=64×64; 1 mm thickness) combined with the saturation-recovery preparation was used for imaging T_1^{app} with nine varied T_{SR} of 0.008, 0.1, 0.2, 0.3, 0.4, 0.5, 1.4, 3 and 10 s. Three b factors (0, 518, 1019

s·mm^{-2}) were achieved by adjusting the diffusion gradient strength with δt = 2.5 ms and T = 3.6ms. For varied thickness slab (0.5cm and 1cm, see schematic figure 3.1a) saturation preparation studies, the EPI slice was located in the middle of saturated slab.

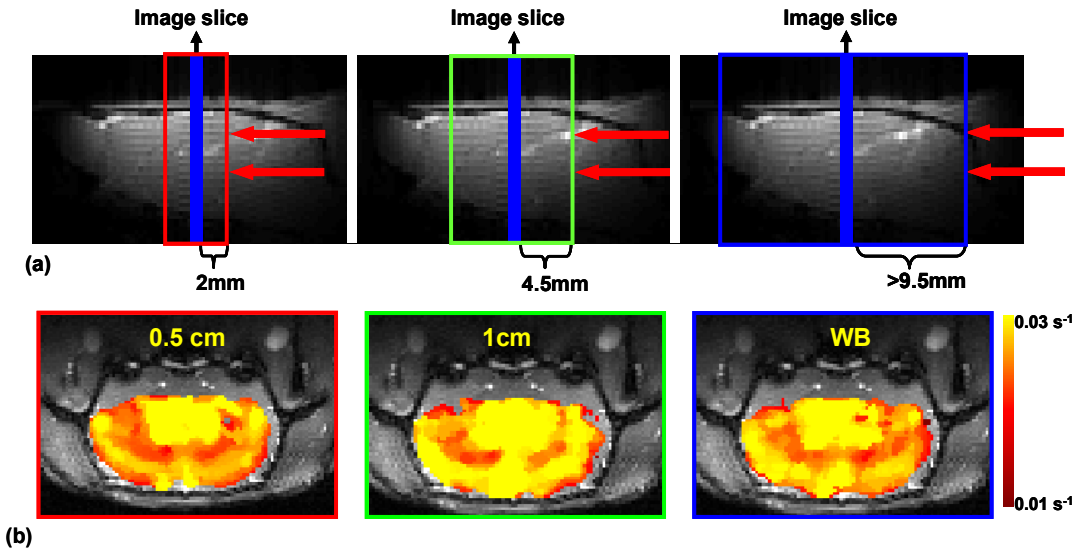

Figure 3.1 (a) Schematic graphs of varied saturation preparation bands in rat brain. Red box represents 0.5cm saturation slab, green box represents 1cm saturation slab, blue box shows the normally used global saturation region for the whole rat brain. The red arrows outside of the box indicate the fully relaxed arterial blood spins. The blue vertical bar in the middle indicates the 2mm thickness image slice. (b)ΔR_1^{app} maps between normocapnia and hypercapnia conditions with varied saturation slabs overlaid on its anatomic coronal image in a representative rat. The outline color of ΔR_1^{app} maps match with schematic graph saturation box in (a).

Slab saturation was achieved through a BISTRO pulse train combined with slice-selection gradients[82]. ROI data taken from the rat somatosensory cortex were used to perform the R_1 regression analysis and determine R_1^{app} and ΔR_1^{app}. MRI data analysis was performed using the STIMULATE software package and the Matlab software package. R_1^{app} and ΔR_1^{app} maps were generated with two-dimensional median filtering on a pixel by pixel

basis and overlaid on its corresponding anatomical image. One way ANOVA and paired t-test were used for statistic analysis.

3.4 Results

3.4.1 Consistent R_1^{app} and ΔR_1^{app} under varied b factor diffusion weightings

Figure 3.2 shows anatomic image and R_1^{app} maps obtained with and without bipolar diffusion gradients under both normocapnia and hypercapnia conditions in a representative rat. The whole brain R_1^{app} elevates during the mild hypercapnia due to the global CBF increase. There is a similar spatial pattern of R_1^{app} maps under different b factor diffusion weightings for both normocapnia and hypercapnia conditions.

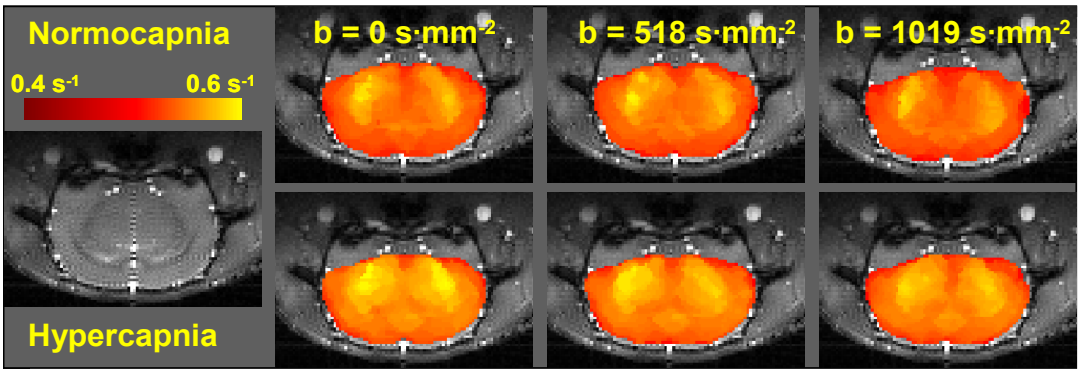

Figure 3.2 Anatomic coronal image and R_1^{app} maps with and without bipolar diffusion gradients under both normocapnia and hypercapnia conditions in a representative rat.

Table 3.1 summarizes the mean and standard deviation results of the apparent longitudinal relaxation rates measured during normocapnia (R_1^{app}) and hypercapnia (R_1^{app}') using three different diffusion-weighting *b* factors. It shows R_1^{app} significantly increased ($p<0.001$) during hypercapnia in the presence or absence of diffusion gradients, however, no

statistical difference was found among the three conditions with varied diffusion-weighting factors either for normocapnia (R_1^{app}, p = 0.80) or hypercapnia (R_1^{app}', p = 0.29) condition. These results clearly indicate that the macro-vascular flow contribution to the measured R_1 is negligible for the rat brain at 9.4T.

Table 3.1 Summary of apparent longitudinal relaxation rate obtained during control (R_1^{app}) and hypercapnia (R_1'^{app}) states in the rat brain under different diffusion-weighting *b* factors (s·mm^{-2}) (mean±SD).

b factor (s·mm^{-2})	Control R_1^{app}(s^{-1})	Hypercapnia R_1^{app}' (s^{-1})
0	0.480 ± 0.005 (n=20)	0.503 ± 0.007 (n=20)
518	0.479 ± 0.007 (n=10)	0.502 ± 0.007 (n=10)
1019	0.481 ± 0.007 (n=7)	0.498 ± 0.007 (n=7)

One-way ANOVA for comparing R_1 under different diffusion weighting *b* factors, p=0.80.
One-way ANOVA for comparing R_1' under different diffusion weighting *b* factors, p=0.29.
Paired-t test for comparing R_1 and R_1' under a given diffusion weighting *b* factor, p<0.001.

3.4.2 Consistent R_1^{app} and ΔR_1^{app} with varied slab thickness saturation preparation and different fitting approaches

Figure 3.1a shows schematic illustration of varied saturation regions. Figure 3.1b shows the anatomic image and ΔR_1^{app} difference maps between normocapnia and hypercapnia R_1^{app} images with varied saturation slabs in a representative rat. It shows that both magnitude and pattern change of ΔR_1^{app}s with three different saturation preparations are similar regardless of different slab saturation thickness. Besides the nine T_{SR} points (0.008, 0.1, 0.2, 0.3, 0.4, 0.5, 1.4, 3 and 10 sec) fitting for R_1^{app} analysis, four points (0.5, 1.4, 3 and 10sec) fitting of the identical data set was performed to purposely ignore the

magnetization contribution of initial saturation-recovery period of ≤ 400ms, which is comparable to the blood transit delay time in the rat brain[29, 62-64]. The comparison results are show in Table 3.2.

Table 3.2 Summary of R_1^{app} and delta R_1^{app} values with distinct saturation bands and with different fitting approaches. No statistic difference (n=9) was found among R_1^{app}s (both under normocapnia and hypercapnia conditions) and delta R_1^{app}s of three distinct saturation bands. The same results were observed in delta R_1^{app} s with different saturation preparation using four points fitting approach. Paired t-test also shows that delta R_1^{app} s are consistent regardless of the different fitting approaches, which demonstrates that transit delay and our early experimental method should not be a major concern for perfusion measurement. (WB: Whole brain saturation recovery method.)

	Nine points fitting*									Four points fitting*		
	Normocapnia R_1^{app} (s^{-1})			Hypercapnia R_1^{app} (s^{-1})			Delta R_1^{app} (s^{-1})			Delta R_1^{app} (s^{-1})		
	0.5cm	1cm	WB	0.5cm	1cm	WB	0.5cm	1cm	WB	0.5cm	1cm	WB
Mean	0.4867	0.4839	0.4829	0.5084	0.5111	0.5040	0.0217	0.0272	0.0211	0.0206	0.0264	0.0215
Std	0.0157	0.0148	0.0141	0.0113	0.0114	0.0097	0.0078	0.0104	0.0092	0.0084	0.0109	0.0077
P value	0.85			0.39			0.22			0.37		

Delta R_1 Nine points fitting vs. Four points fitting			
	0.5 cm	1cm	WB
P value	0.10	0.20	0.72
CI	-0.0003—0.0025	-0.0006—0.0023	-0.0024—0.0018

*Nine points fitting: R_1^{app} values obtained from0.008,0.1,0.2,0.3,0.4,0.5,1.4,3,10 seconds.
Four points fitting: R_1^{app} values obtained from 0.5,1.4,3,10 seconds.
Significantly different from the value measured prior to hypercapnia; p<0.05.

Surprisingly, almost identical results were found among ΔR_1^{app} values (0.0217 s^{-1} vs.0.0206 s^{-1} for 0.5cm saturation slab, 0.0272 s^{-1} vs. 0.0264 s^{-1} for 1cm saturation slab, 0.0211 s^{-1} vs. 0.0215 s^{-1} for whole brain saturation) based on nine points fitting approach compared to four points fitting approach despite the fitted R_1^{app} values being systematically different.

3.5 Discussion

The large vessel inflow effect and arterial transit time are two general concerns of MR ASL techniques for CBF quantification. In order to address whether these factors could significantly confound the measurement of CBF change using the SR-T_1 method, we performed bipolar diffusion gradients and varied slab thickness saturation combined with the SR-T_1 imaging sequence. It has shown that no statistical difference of R_1^{app}s measured with the graded strengths of diffusion gradients (Table3.1). This finding suggests that the macrovascular inflow effect does not dominate the R_1^{app} measurement and its effect on quantifying ΔCBF is negligible. Otherwise a persistent decrease in R_1^{app} is expected when the b factor increases. Moreover, the short T_2 in venous blood at high field (~9 ms at 9.4T) could further minimize the macrovascular in-flow contribution from the venous side when TE=23 ms was used in EPI acquisition in this study.

By varying the saturation slab thickness (Figure 3.1a), the fully relaxed blood water spins outside of the saturation bands travel (assuming the arterial blood spins travel smoothly as bulk flow at a constant speed without any turbulence) with a different distance, by thus different arterial transit time in different saturation preparation before they reach the image slice. For example, the blood transit distances are about 2mm, 4.5mm and >9.5mm when the saturation slabs are 0.5cm, 1cm and the global brain saturation respectively. If the transit time plays an important role of R_1^{app} measurement, one would expect to see the dependence of R_1^{app} on the varied transit distance. Specifically, R_1^{app} value could be largest when the 0.5cm saturation slab is applied because of its shortest transit distance. Our results, however, did not show statistic

difference in R_1^{app} and ΔR_1^{app} among three distinct slab saturation widths. Moreover, the ΔR_1^{app} values derived from four points fitting strategy also show no statistic difference with nine points (Table 3.2), indicating that the ΔR_1^{app} values are consistent disregard of the different fitting approaches. Delta R_1^{app} maps between hypercapnia and normocapnia with different saturation preparation thicknesses using SR-T_1 method, showing a consistent spatial pattern which displayed in Figure 3.1b. These results imply that different slab saturation thickness associated with the various blood water transit times might not influence the R_1^{app} values significantly. Lastly, the calculated CBF increase induced by mild hypercapnia was ~1.25ml/g/min, which is consistent with literatures under similar condition [29, 83-85]. In fact, these results also corroborate with Eq. 2.11, which describes the magnetization when $t<t_{tran}$, wherein term B accounts for less than 4% of term A. Therefore, single exponential relaxation based on the signal of $t \geq t_{tran}$ could still represent the R_1^{app} values well.

3.6 Conclusion

The overall results in this study suggest that confounding factors such as the large vessel inflow effect and arterial transit time have negligible effects on quantifying the CBF change based on the saturation-recovery T_1 MRI measurement, therefore, it should provide an alternative, valid, quantitative MRI-based neuroimaging tool for simultaneously measuring the CBF change in response to physiological perturbations (e.g., brain activation) or pathological perturbations (e.g., stroke or pharmaceutical drug treatment).

CHAPTER 4 Further Validation of the SR-T_1 Method for Imaging Absolute CBF Change with the Continuous Arterial Spin Labeling Technique

Abstract

The Saturation-Recovery(SR) T_1 method for imaging absolute cerebral blood flow (CBF) change (ΔCBF) has been proposed and verified with simultaneously relative CBF monitoring with laser Doppler flowmetry (LDF). In the present study, the absolute CBF increase induced by mild transient hypercapnia in rat brain calculated with the SR-T_1 method is further directly compared with two-coil system continuous arterial spin labeling (CASL) MR approach at 9.4T. A strong and positive correlation of ΔCBF was found between the SR-T_1 method and the CASL technique. Moreover, the tissue intrinsic relaxation time (T_1^{int}) and the blood tissue partition coefficient λ are numerically calculated based on these two measurements. Finally, we demonstrate in this study that in addition to the absolute CBF change, the baseline CBF value could be potentially obtained with the SR-T_1 measurement once the T_1^{int} is determined.

Keywords: perfusion; cerebral blood flow; saturation-recovery-T_1 MRI; Continuous arterial spin labeling CASL; hypercapnia; brain; rat.

4.1 Introduction

The saturation recovery T_1 (SR-T_1) method for imaging cerebral blood flow (CBF) change (ΔCBF) caused by physiological and pathological perturbations has been proposed and works well. [74, 86] We have validated it by comparing the calculated absolute CBF change (ΔCBF) based on SR-T_1 measurement with simultaneously relative CBF change monitoring using laser Doppler flowmetry (LDF). The calculated baseline CBF values were coincident with the results of majority of literature reported in rat brain under similar anesthesia condition. However, that was an indirect comparison and it would be more rigorous and explicit if ΔCBF calculated with SR-T_1 method could be directly compared with ΔCBF using standard MRI quantitative approach. Moreover, besides the ΔCBF induced by physiology and pathology perturbations, more comprehensive information about brain blood supply, such as the baseline CBF value are also preferable to obtain concurrently with the SR-T_1 method. In order to address the above raised two issues, a direct comparison study of imaging absolute CBF change between the SR-T_1 method and the continuous arterial spin labeling (CASL) was applied in rat brain at 9.4T.

4.2 Method and Theory

4.2.1 Absolute CBF change calculation with SR-T_1 measurement

The saturation-recovery (SR)-T_1 MRI measurement consists of a global saturation preparation followed by magnetization acquisition with fast echo-planar imaging (EPI) sampling after waiting a serial of saturation recovery time (T_{SR}). Small brain size

associated with fast blood velocity lead to a short transit time, which enables the longitudinal relaxation time in the brain tissue to be flow sensitive despite of the non-selective saturation preparation. [74] The numerical apparent longitudinal relaxation time (T_1^{app}) regressed with the above mentioned saturation recovery magnetization can be linked to CBF as the following equation,

$$\frac{1}{T_1^{app}} = \frac{1}{T_1^{int}} + \frac{CBF}{\lambda}$$

$$R_1^{app} = R_1^{int} + \frac{CBF}{\lambda} \qquad (4.1)$$

where T_1^{int} (R_1^{int}) is the intrinsic longitudinal relaxation time (rate) of brain tissue, which is an internal characteristic parameter and could be treated as a constant; λ is the blood tissue partition coefficient for water, 0.9ml/g is commonly used in the literatures [61]. An increased CBF caused by hypercapnia or stimulation leads to an accelerated longitudinal relaxation rate (R_1^{app}'). Therefore, the absolute CBF increase under hypercapnia or stimulation is able to be calculated from the R_1^{app} difference (ΔR_1^{app}) between the normocapnia (or control) and hypercapnia (or stimulation) conditions, according to equation (4.2):

$$\Delta R_1^{app} = R_1^{app}{}' - R_1^{app} = \frac{\Delta CBF}{\lambda}$$

$$\Delta CBF = \lambda \cdot \Delta R_1^{app} \qquad (4.2)$$

4.2.2 Baseline CBF and absolute CBF change calculation with CASL

CASL [29, 30, 87-89]was first proposed by Detre et al, it enables to measure CBF in an absolute scale (the absolute CBF) by a long RF pulse of labeling arterial blood with a high contrast to noise ratio. Since the cross-correlation effect between brain water and macromolecules is insignificant and negligible[90, 91] with the two-coil system measurement, the absolute CBF image can be created from a pair wise subtraction of the labeled and control image on a pixel-by-pixel basis, according to [64, 89, 91]:

$$CBF = \frac{\lambda}{T_1^{\text{int}}} \cdot \frac{S_C - S_L}{S_L + (2 \cdot \alpha - 1) \cdot S_C} \qquad (4.3)$$

Where S_C and S_L are signal intensity of the image without and with the RF spin labeling respectively, α is the effective efficiency of the arterial spin labeling and it can be determined by:

$$\alpha = \alpha_1 \cdot \frac{TL}{TR} \qquad (4.4)$$

α_1 is the initial degree of spin labeling measured at the labeling plane, which is equals to 1 for inversion and 0.5 for saturation; the duty cycle is defined as TL/TR, where TL is the length of labeling RF pulse, TR is the repetition time of acquisition. The absolute CBF change simply equals to the CBF values obtained at hypercapnia condition minus the CBF values derived at normocapnia condition.

4.3 Materials and Experiment Design

4.3.1 Animal preparation and experiment procedures

There were nine male Sprague-Dawley rats weighing 299 ± 59 g included in the present study. Initially, the rat was anesthetized and intubated using 5% (v/v) isoflurane in N_2O:O_2 (60/40) gas mixture. The femoral artery and femoral vein were catheterized for physiological monitoring and blood sampling. After the surgical operation, the rat was placed in a home-built cradle incorporating ear bars and a bite bar to reduce head movement and to ensure proper positioning inside the MRI scanner. The animal anesthesia was maintained at 2% isoflurane. The mild transient hypercapnia was introduced by switching to a gas bag filled with 6% (or 3%) CO_2, 34% O_2, 58% N_2O and 2% isoflurane for about 10 minutes. The hypercapnia studies were repeated two to four occurrences in seven out of nine rats to test the reproducibility of absolute CBF increase with two different techniques. Rectal temperature was maintained at 37.0±0.5ºC with a home-made circulating/heating water blanket, and the inspired and expired gases and blood pressure were monitored constantly. The rate and volume of ventilation were adjusted to maintain normal blood gases. All surgical procedures and experimental protocols were approved by the Institutional Animal Care and Use Committee of University of Minnesota.

4.3.2 MRI experiment parameters

All MRI experiments were conducted on a 9.4T horizontal animal magnet (Magnex Scientific, Abingdon, UK) interfaced to a Varian INOVA console (Palo Alto,

CA, USA). A butterfly-shape surface coil (long axis of 2.8 cm and a short axis of 2.0 cm that is parallel to the animal spine) was used to collect both the SR-T_1 measurement and the CASL MRI data. A separate single loop coil (2.5cm × 1.2cm) was used for carotid arterial spin labeling to eliminate the magnetization effect between tissue water and macromolecules [89, 90]. The distance between labeling plane and the brain image was adjusted at about 2cm to reduce the interaction between the two coils.

Brain scout images were acquired using a turbo fast low angle shot (TurboFLASH) imaging sequence [67] with the following imaging acquisition parameters: TR = 10 ms, TE = 3.1 ms, image slice thickness = 2 mm, field of view (FOV) = 3.0 cm×3.0 cm; image matrix size = 128×128. Identical parameters were used for the anatomic carotid arterial labeling plane except for the echo time is 4ms. The labeling efficiency α_1 was measured using a 500ms RF inversion preparation at 0.5cm upstream of the carotid labeling plane followed by the TurboFLASH sequence at the carotid arterial labeling plane with TR and TE were 530ms and 4ms respectively. Specifically, the labeling efficiency was calculated from the signal intensity in the two-side carotid arteries with and without turning on the inversion RF power. For the CASL experiment, the duration of the RF labeling pulse (TL) was 2.2 sec and TR was 3 sec, resulting in a duty cycle as 0.73. Echo time is 30ms, FOV = 3.0 cm×3.0 cm and image matrix size = 64×64, resulting in a 0.47mm×0.47mm brain in plane resolution. The labeled and control brain images (slice thickness is 2mm) were acquired in an interleaved fashion. In addition, the labeling pulse was also applied at a plane equilateral symmetry to the brain image plane to balance the off-resonance effect of the static spins in the brain

image plane. For the SR-T_1 measurement experiment, the global saturation was achieved with an adiabatic 90º pulse (4 ms pulse width) followed by three orthogonal crush gradients with 3 ms length. Gradient-echo (GE) EPI (TE = 21 ms; FOV = 3.0cm×3.0cm; image matrix size = 64×64; single slice coronal image with 2 mm thickness) combined with the saturation-recovery preparation was used to image T_1^{app} with nine T_{SR} values of 0.008, 0.1, 0.2, 0.3, 0.4, 0.5, 1.4, 3 and 10 seconds. Both the CASL sequence and the SR-T_1 measurement were acquired during steady state of normocapnia and hypercapnia for about 2minutes, corresponding to 10 image volumes of the CASL approach and 8 image volumes of the SR-T_1 method.

4.3.3 Data analysis

MRI data analysis was performed using the STIMULATE software package (Stimulate, Center for Magnetic Resonance Research, University of Minnesota, USA) [69] and the Matlab software package (The Mathworks inc., Natick, MA, USA). Region of interest (ROI) taken from the rat sensory cortex is used to perform the T_1^{app} regression analysis and to determine ΔR_1^{app}, by thus the ΔCBF according to Eq. (4.2). The least-square nonlinear curve fitting program using the Matlab software was applied to perform the T_1^{app} regression analysis. The regression accuracy was estimated by the sum squared error (sse) and the square of regression coefficient (R^2). Identical ROIs were used to calculate the absolute CBF and ΔCBF with CASL experiment according to Eq. (4.3).

The ΔCBF maps between hypercapnia and normocapnia were created on a pixel by pixel basis (pixel size 0.25×0.25×2mm³, with nearest neighbor interpolation) with two-dimensional median filtering and then overlapped on the anatomic image.

Correlation coefficient and its associated p value of ROI based ΔCBF values between the SR-T_1 method and the CASL method was calculated.

4.4 Results

The measured initial spin inversion efficiency α_1 is 0.76±0.02, which leads to the effective efficiency of the arterial spin labeling α as 0.56 according to equation (4.4). The degree of spin inversion α_1 measured in this study is consistent with previous reports, ranging from 0.71 to 0.82, [39](0.71), [89](0.81), [87](0.82). It has been demonstrated that the degree of inversion won't influence the CBF quantification as long as it is determined and accounted in the perfusion calculating model[83]

4.4.1 Consistent ΔCBF calculated with the SR-T_1 method and with the CASL technique

Figure 4.1 shows the linear fitting results of ΔCBF calculated with the SR-T_1 method verse ΔCBF obtained with the CASL technique in sensory cortex of a representative rat for four occurrences of hypercapnia. Both fitting results of pixel by pixel (Figure 4.1a) and mean value and standard deviation within ROI (Figure 4.1b) under four occurrences of hypercapnia reveal a strong (p-value<0.01) positive correlation between ΔCBF calculated with the SR-T_1 method and with the CASL approach. It also demonstrates that both techniques are very sensitive to the CBF change induced by varied level of CO_2 concentration. For instance, the CBF increases more under 6% CO_2 hypercapnia than under 3% CO_2 of hypercapnia.

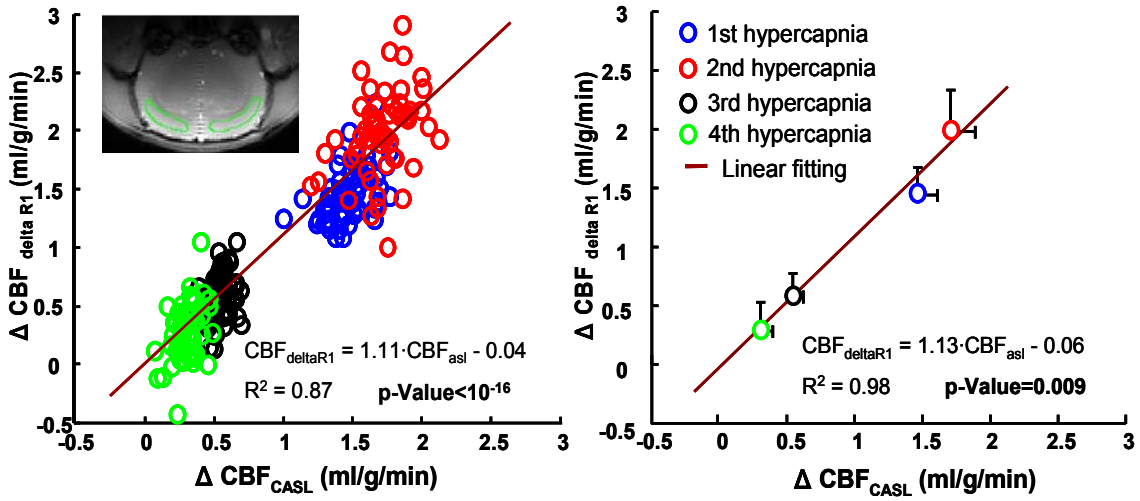

(a) (b)

Figure 4.1 Linear fitting results of brain cortex ΔCBF calculated with the SR-T_1 technique versus ΔCBF calculated with the CASL method in a representative rat for four occurrences of hypercapnia. (a) Pixel-wised linear fitting results of ΔCBF calculated with the SR-T_1 technique versus ΔCBF calculated with the CASL method in the ROI (within the green line) shown in anatomic brain image. (b) Linear fitting results of mean ΔCBF in ROI (shown in a) calculated with the SR-T_1 technique versus that calculated with the CASL method. Positive standard deviation bars for both ΔCBF calculated with the SR-T_1 technique and with the CASL method are shown. Different colors represent four occurrences of hypercapnia. 6% CO_2 was used in the 1st and 2nd occurrences of hypercapnia; 3% CO2 was used in the 3rd and 4th occurrences of hypercapnia. p values of ΔCBF between SR-T_1 method and CASL approach correlation coefficient are indicated in (a) (pixel by pixel wise) and (b) (mean ΔCBF) respectively.

Figure 4.2 displays anatomic image and ΔCBF maps created with the SR-T_1 technique and with the CASL method for four occurrences of hypercapnia. Repeatable, similar spatial pattern and magnitude of CBF increase are observed in the SR-T_1 method and with the CASL approach under the same degree of CO_2 inhalation. However, the less uniform pattern in the in deep region of rat brain is observed in the SR-T_1 method likely

due to the higher sensitivity of EPI sequence to the susceptibility effect than TurboFLASH imaging sequence used in CASL.

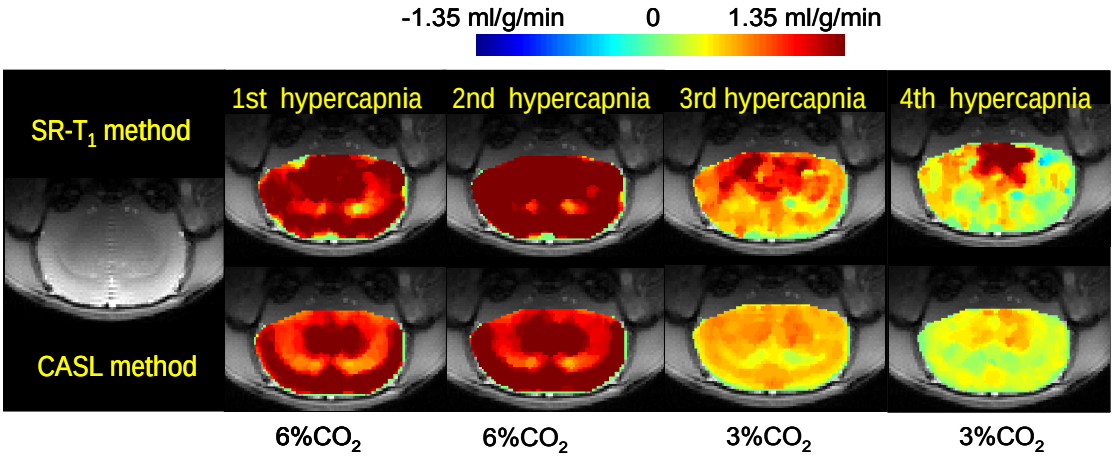

Figure 4.2 Anatomic image (first column) as well as ΔCBF maps created with the SR-T_1 technique (the upper row) and with the CASL method (the lower row) in a representative rat for four occurrences of hypercapnia. 6% CO_2 was used in the 1st and 2nd occurrences of hypercapnia; 3% CO2 was used in the 3rd and 4th occurrences of hypercapnia.

Figure 4.3a shows the excellent agreement between ΔCBF calculated with the SR-T_1 method and ΔCBF values obtained with the CASL method in cortex of the 9 rats with 20 occurrences of different level of hypercapnia included in this study. The consistency of the ΔCBF measurement was quantitatively evaluated and the Bland-Altman plot between the difference and the mean ΔCBF calculated with these two techniques is shown in figure 4.3b. The mean (black line) and the standard deviation (SD) of the difference between the ΔCBF calculated with these two techniques were 0.087 ml/g/min and 0.12 ml/g/min, respectively. The gray lines in figure 4.3b represent the limits of consistency

where 95% of the difference values are expected to be less than two SD. Clearly, almost all of the data points were within the range, demonstrating an excellent consistency between ΔCBF measured with these two techniques.

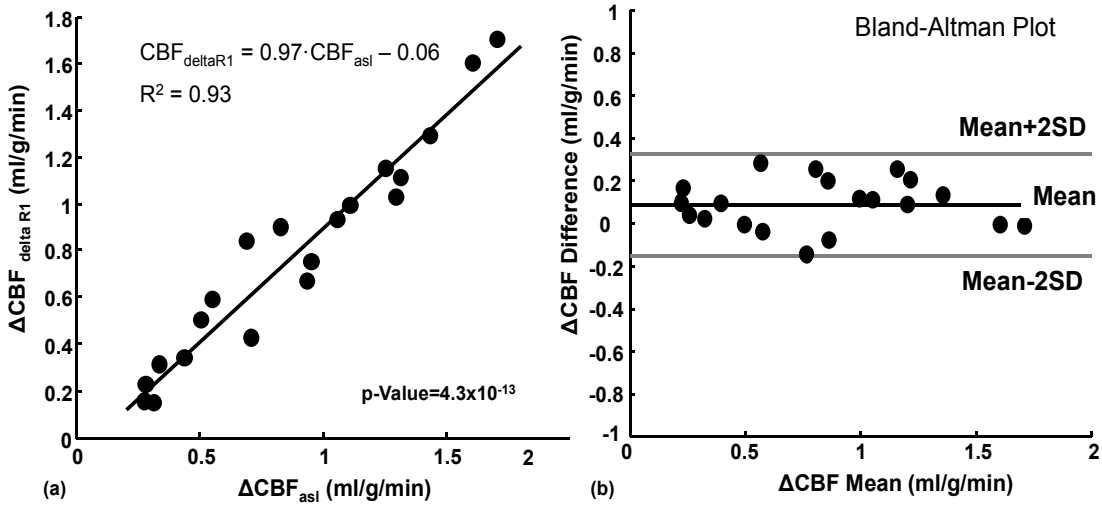

Figure 4.3 (a) Linear fitting results of brain sensory cortex ΔCBF calculated with the SR-T_1 technique versus ΔCBF calculated with the CASL method in 9 rats with 20 occurrences of hypercapnia. p value of ΔCBF between SR-T_1 method and CASL approach correlation coefficient is indicated. (b) The bland-Altman plot of the difference versus the mean values between the ΔCBF calculated with two different techniques. The black line indicates the mean (0.087 ml/g/min) of the difference of the ΔCBF calculated with these two techniques and the gray lines define the limits of agreement where 95% of the difference values are expected to be less than two standard deviation (SD = 0.12 ml/g/min).

4.4.2 R_1^{app} measured with the SR-T_1 method versus CBF computed with the CASL technique

Linear fitting result of R_1^{app} measured with the SR-T_1 method versus absolute CBF calculated from the CASL technique under both normocapnia and hypercapnia in a

typical rat is shown in Figure 4.4a. According to equation (4.1), the slope of the linear fitting in figure 4.4 can be used to derive the blood tissue partition coefficient for water λ and the extrapolated intercept of this fitting should represent the R_1^{int}. Figure 4.4b shows the linear fitting result of rat brain sensory cortex R_1^{app} measured with the SR-T_1 technique versus absolute CBF calculated with the CASL method for two to four occurrences of normocapnia and hypercapnia of eight rats.

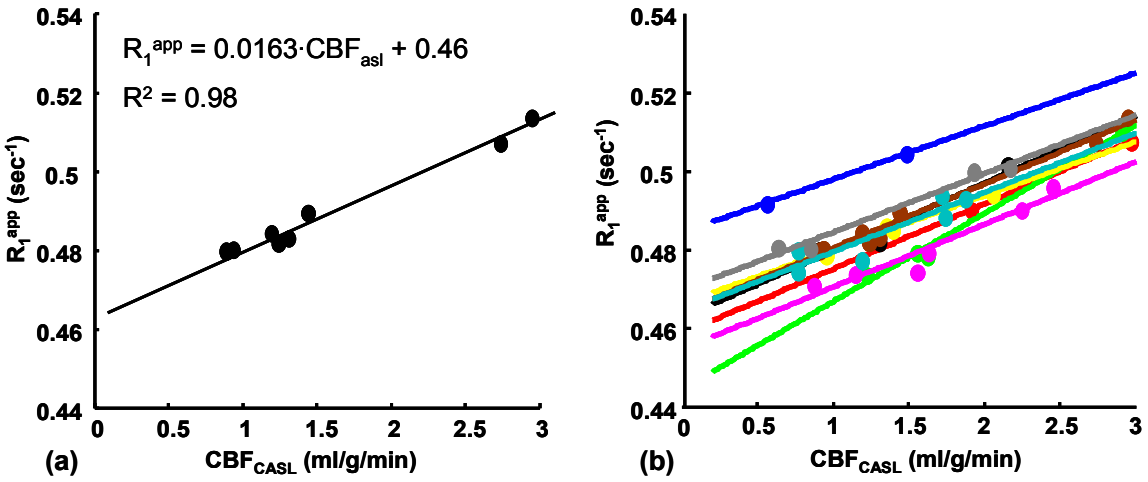

Figure 4.4 (a) Linear fitting results of rat brain sensory cortex R_1^{app} measured with the SR-T_1 technique versus absolute CBF calculated with the CASL method in a representative rat for four occurrences of normocapnia and hypercapnia. (b) Linear fitting results of rat brain sensory cortex R_1^{app} measured with the SR-T_1 technique versus absolute CBF calculated with the CASL method for two to four occurrences of normocapnia and hypercapnia of eight rats, each color represents one individual rat.

Table 4.1 summarizes the slopes, intercepts and R^2 of linear fitting for the SR-T_1 method versus absolute CBF calculated from the CASL technique under both normocapnia and

hypercapnia in 9 rats. From table 4.1, the mean value of R_1^{int} value and the estimated λ are 0.4628 s^{-1} and 1.02ml/g (1/0.0163 g/ml /60sec) respectively.

Table 4.1 Summary of mean and standard deviation of slopes and intercepts of linear fitting of brain sensory cortex R_1^{app} measured with the SR-T_1 measurement versus absolute CBF calculated with the CASL method in 9 rats under both normocapnia and hypercapnia conditions.

Subject No.	Slope (g/ml)	Intercept (s^{-1})	
1	0.0135	0.4845	----
2	0.0165	0.4587	----
3	0.0171	0.4628	0.98
4	0.0224	0.4445	0.99
5	0.0159	0.4547	0.92
6	0.0137	0.4664	0.98
7	0.0163	0.4642	0.98
8	0.0167	0.4644	0.95
9	0.0149	0.4696	0.97
Mean	0.0163	0.4628	0.97
Std	0.0026	0.0109	0.02

4.5 Discussion

We have proposed the SR-T_1 method for imaging rat brain absolute CBF change and validated it with simultaneous LDF measurement (relative CBF change) with both hypercapnic and ischemic rat model in 9.4T. This quantitative CBF measurement was further verified with two-coiled CASL MR technique by directly comparing the absolute perfusion increase in rat brain induced by hypercapnia in this current study. A good agreement is observed between the absolute CBF increase in the rat brain with the SR-T_1 method and with the CASL approach (Figure 4.1-4.3). First of all, the rat brain cortex shows a nice pixel-wised ΔCBF correlation (Figure 4.1) measured with these two

techniques under different level of transient mild hypercapnia. Moreover, the spatial pattern of the whole brain ΔCBF maps created with the SR-T_1 method and with the CASL approach is also very similar for the varied degree of hypercapnia although the deep region of the SR-T_1 method measured ΔCBF maps is less uniform due to the high demand of homogeneousness of the B_1 field of the EPI sequence (Figure 4.2). Furthermore, the amount of CBF increase correlates well with the concentration of CO_2 of the hypercapnia being used, i.e. the higher the CO_2 concentration, the CBF increases more. This phenomenon indicates that both the SR-T_1 method and the CASL technique are very sensitive for imaging perfusion. Meanwhile, it is also interesting to point out that the degree of CBF increase at different occurrences of hypercapnia is close but not exactly identical even at the same level of mild hypercapnia. For instance, in the same rat, the perfusion increases more for the second occurrence of the 6% hypercapnia, while it increases less for the second occurrence of the 3% hypercapnia when compared with the first occurrence of same level CO_2 concentration hypercapnia (Figure 4.1-4.3). This observation implies the complicated but delicate regulation and response of the live body when the challenge of the environment is encountered.

Based on the results of R_1^{app} measured with the SR-T_1 method and absolute CBF value calculated with the CASL approach, R_1^{int} as well as the blood tissue partition coefficient for water λ can be obtained through a linear fitting according to equation (4.1). Figure 4.4a shows such a fitting of R_1^{app} versus CBF under both normocapnia and hypercapnia conditions in a representative rat. The averaged R_1^{int} and λ for the total nine

rats are 0.4628 sec^{-1} and 1.02ml/g, respectively. Both of these two values obtained from this study is coincident with the previous report 0.5 sec^{-1} [62, 92, 93] and 0.90-0.98 ml/g [61, 94, 95] measured with variety of techniques.

These results have two aspects of impacts. To begin with, the absolute CBF potentially is able to be calculated through equation (4.1) with a straightforward T_1 measurement if the R_1^{int} is known. Therefore, the SR-T_1 method offers a simple and noninvasive tool to measure both absolute CBF and CBF changes in rat brain as long as the R_1^{int} is carefully determined. However, caution needs to be nevertheless exercised the R_1^{int} obtained in the present study is only valid in the normal rat brain at 9.4T due to the fact that R_1^{int} is pathology sensitive and magnetic field dependent. Secondly, the tissue blood partition coefficient for water λ is estimated with two noninvasive MR techniques in the present study and the value reasonably agrees with the values measured with Xenon-enhanced CT study and relative proton density imaging results. These findings, on the other hand, also demonstrate that the T_1 perfusion model is valid for CBF measurement and the CBF indeed could be viewed as an enhanced T_1 process.

4.6 Conclusion

The SR-T_1 method for imaging absolute CBF increase in rat brain induced by transient mild hypercapnia is further validated by the two-coil system CASL approach at 9.4T. It is also potentially capable of providing the baseline CBF of rat brain once the R_1^{int} is carefully determined. By thus both baseline CBF and CBF change can be measured through SR-T_1 method. Therefore, the SR-T_1 method should provide a simple,

reliable and noninvasive tool to image small animal brain perfusion and BOLD under both physiological and pathological conditions.

CHAPTER 5 Imaging Absolute CBF Change in Rat Brain with the SR-T_1 Method at 9.4T and 16.4T

5.1 Introduction

Cerebral blood flow (CBF) and its dynamic change are closely related to brain function, metabolism, and viability. Saturation-recovery T_1 (SR-T_1) measurement provides a simple and effective tool for monitoring rat brain CBF change and other useful information such as blood-oxygen-level dependent (BOLD) signal and basal CBF simultaneously[74, 86, 96]. It is well known that the proton longitudinal relaxation time T_1^{app} is a magnetic field dependent parameter, specifically, T_1^{app} increases when magnetic field strength goes up. In contrast, the alteration of CBF corresponding to physiological and/or pathological change should be magnetic field independent. In this study we were intrigued by the distinct property difference and field dependence between T_1^{app} and CBF change. The rat brain CBF increase induced by mild hypercapnia was measured using the SR-T_1 technique at both 9.4T and 16.4T to test whether it is consistent at different magnet field strengths. Meanwhile, CBF change was also measured and validated by continuous arterial spin labeling (CASL) technique in those rats performed with the SR-T_1 method at 9.4T.

5.2 Theory

5.2.1 Absolute CBF change calculation with the SR-T_1 measurement

See Chapter 4.2.1

5.2.2 Baseline CBF and absolute CBF change calculation with the CASL technique

See Chapter 4.2.2

5.3 Material and MRI Method

MRI experiments were performed at either a 9.4T/31cm or a 16.4T/26cm bore magnet interfaced with VNMRJ consoles (Varian, CA). Two identically sized 8-shaped surface coils (2.8cm×2cm) with different resonance frequency were used to acquire rat brain images. A separate 8-shaped coil (1cm diameter) was used for carotid arterial spin labeling for the 9.4T experiment [90]. The distance between the labeling plane and the brain image slice was adjusted to about 2cm to reduce the interaction between the tagging and head RF coils. Nine experiments of hypercapnia (6% CO_2, 34% O_2, 58% N_2O and 2% isoflurane) were conducted in 5 rats for comparing CBF change measured with the SR-T_1 method and the CASL technique at 9.4T. Another 5 rats with 8 occurrences of the same level of hypercapnia were carried out at 16.4T to compare ΔR_1 and ΔCBF values with those at 9.4T. All the R_1 images and CASL measurements were acquired before (i.e., normocapnia or control) and during hypercapnia condition when the animal physiology was within a normal range. Gradient echo EPI (TE=17ms; FOV=3.2×3.2cm; image matrix=64×64; 2 mm thickness) combined with the saturation-recovery

preparation was used for imaging T_1 with 32 varied T_{SR} values range from 0.011 to 12s for both 9.4T and 16.4T experiments. A modified TurboFLASH sequence (TE=30ms; TR=3sec; FOV=3.2×3.2cm; image matrix=64×64; 2 mm thickness) was used for the CASL experiment at 9.4T. The duration of the RF labeling pulse was 2.2 sec. MRI data analysis was performed using the Matlab software package. ROI data taken from the rat somatosensory cortex were used to perform the R_1 regression analysis and to determine the R_1, ΔR_1 and subsequently ΔCBF at both 9.4T and 16.4T. Absolute CBF and ΔCBF was also calculated with the CASL technique using the identical ROI as in the SR-T_1 method at 9.4T and compared with the ΔCBF calculated using the latter method. Finally, ΔCBF maps created with SR-T_1 method (both 9.4T and 16.4T) as well as ΔCBF maps calculated with CASL method (at 9.4T) were generated and then overlapped on the corresponding anatomic images.

5.4 Results

The average of absolute R_1 values of the rat brain cortex under the control condition at 9.4T and 16.4T were 0.496 and 0.420 s^{-1} respectively, corresponding to an 18% longer of T_1 at 16.4T than at 9.4T. However, no statistical difference ($p=0.28$) was found between ΔR_1s and by thus ΔCBF obtained at 9.4T and 16.4T despite of the significant R_1 discrepancy ($p<0.01$) between the two magnetic field strengths (See Table 5.1). The effective efficiency of the arterial spin labeling α used in Eq.4.3 was 0.59±0.01 (n=4), which led to a baseline CBF of 1.2±0.2 ml/g/min and it agrees well with most of previous reports [89, 97-99] of rat brain cortex under the similar anesthesia condition.

The measured cortex ΔCBF increases during hypercapnia measured by the SR-T_1 method and CASL method at 9.4T and 16.4T were also coincidently matched ($p>0.05$, One-way ANOVA).

Table 5.1 Summary of rat brain cortex R_1 under both normocapnia ($R_{1\text{-norm}}$) and hypercapnia ($R_{1\text{-hyper}}$) conditions as well as ΔR_1 ($R_{1\text{-hyper}}$ - $R_{1\text{-norm}}$) calculated with the SR-T_1 method (at both 9.4T and 16.4T); baseline CBF under normocapnia (CBF_{norm}) and hypercapnia (CBF_{hyper}) conditions obtained with the CASL method at 9.4T; and the CBF increase (ΔCBF) during hypercapnia computed with the SR-T_1 method (at both 9.4T and 16.4T) and the CASL method (at 9.4T). (Mean±SEM)

SR-T_1 Method	**16.4T (n=8)**	**9.4T (n=9)**	CASL Method	**9.4T (n=9)**
$R_{1\text{-norm}}$ (s^{-1})	0.420±0.002	0.496±0.004	CBF_{norm}(ml/g/min)	1.200±0.198
$R_{1\text{-hyper}}$(s^{-1})	0.440±0.002	0.514±0.004	CBF_{hyper}(ml/g/min)	1.990±0.228
Δ R_1(s^{-1})	0.020±0.001	0.018±0.002	----	----
Δ CBF(ml/g/min)	1.080±0.078	0.950±0.090	Δ CBF(ml/g/min)	0.790±0.084

Figure 5.1 shows a similar pattern and magnitude of CBF increase maps between normocapnia and hypercapnia conditions using both techniques at 9.4T and 16.4T magnet field strengths.

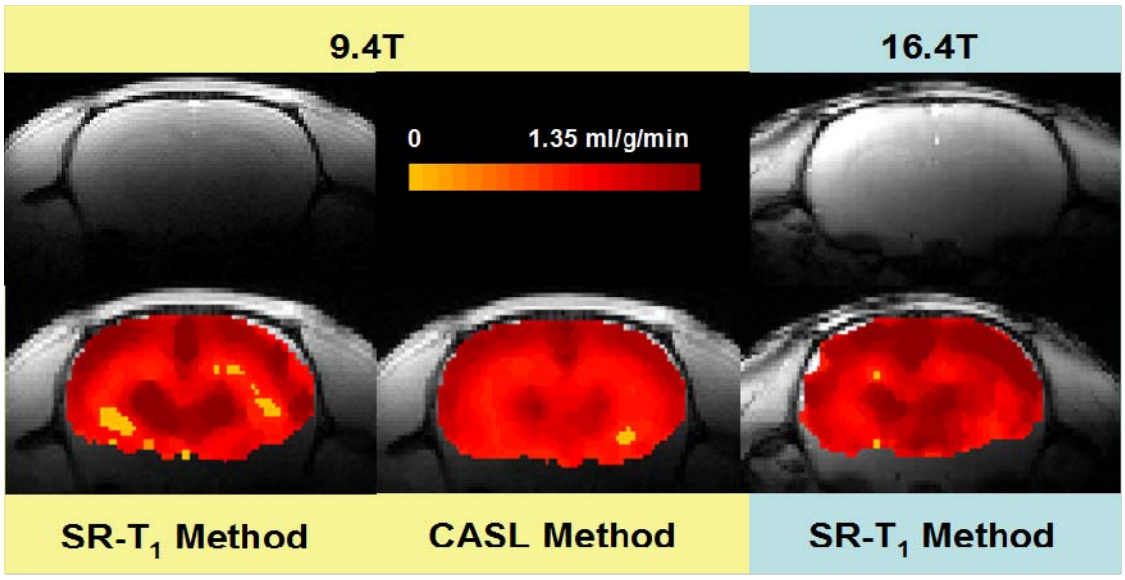

Figure 5.1 Coronal anatomic images and the increased CBF during hypercapnia (ΔCBF) maps of the rat brain created with the SR-T_1 method (at both 9.4T and 16.4T) and the CASL method (at 9.4T).

5.5 Discussion

Our measured rat brain cortex T_1 (2.38±0.01s) at 16.4T is consistent with previously reported 2.27s in the similar region of the rat brain at 16.4T [100], which is about 18% longer than the T_1 (2.02±0.01s) measured at 9.4T under normocapnia condition. The R_1 at 16.4T under hypercapnia condition is also significantly smaller than that at 9.4T ($p<0.01$). Interestingly, ΔR_1, however, shows no statistical difference between at 9.4T and at 16.4T. Consequently, the ΔCBF values calculated from ΔR_1 using Eq.4.2 should be the same regardless of the different field strength of magnet being used to obtain R_1. The field strength independence of ΔR_1, and thus ΔCBF at 9.4T and 16.4T is expected and on the other hand provides another piece of evidence of the validity of SR-T_1 method for quantifying CBF changes in the rat brain. In addition, the agreement of

the rat brain cortex ΔCBF during hypercapnia measured with the SR-T_1 method and with the CASL technique further proves that the SR-T_1 method truly reflects the CBF change. Moreover, the similarity of spatial patterns and magnitude of ΔCBF maps generated with the SR-T_1 method and the CASL technique indicates its effectiveness, sensitivity and accuracy, although the ΔCBF maps created with the SR-T_1 method shows more variation in the deep brain region with relatively poor EPI quality due to inhomogeneous B_0 and B_1 fields (see Figure 5.1). We compared ΔR_1 at the relatively high field strength in this study, however, there should be no hurdle to apply the SR-T_1 method at lower field strength since the concept is the same. In addition, the absolute CBF could also be obtained [96]once the R_1^{int} is known (according to Eq.4.1). It is worth pointing out that R_1^{int}, like R_1, is a field dependent value, which needs to be determined at a given field strength (by extrapolation R_1 when CBF approaches zero). [96]

5.6 Conclusion

In conclusion, our overall data demonstrate that R_1^{int} and R_1 values are magnetic field dependent physical parameters; while ΔR_1s and ΔCBF in response to physiological and pathological change are field independent as we speculate. Secondly, the SR-T_1 method for quantifying absolute CBF change in the rat brain has been further verified at 16.4T. It should provide a valid, simple and efficient way to image CBF change and potentially baseline CBF in the rat brain under both physiological and pathological perturbations.

CHAPTER 6 Large Enhancement of Perfusion Contribution on fMRI Signal

Abstract

The perfusion contribution to the total fMRI signal was investigated using a rat model with mild hypercapnia at 9.4T, and human subjects with visual stimulation at 4T. It was found that the total fMRI signal change could be approximated as a linear superposition of "true" blood oxygenation level dependent (BOLD; T_2/T_2*) effect and the blood flow-related (T_1) effect. The latter effect was significantly enhanced by using short repetition time and/or large RF pulse flip angle and became comparable to the "true" BOLD signal in response to a mild hypercapnia in the rat brain, resulting in an improved contrast-to-noise ratio (CNR). Bipolar diffusion gradients suppressed the intravascular signals but had no significant effect on the flow-related signal. Similar results of enhanced fMRI signal were observed in the human study. The overall results suggest that the observed flow-related signal enhancement is likely originated from perfusion, and this enhancement can improve CNR and the spatial specificity for mapping brain activity and physiology changes. The nature of mixed BOLD and perfusion-related contributions in the total fMRI signal also has implication on BOLD quantification, in particular, the BOLD calibration model commonly used to estimate the change of cerebral metabolic rate of oxygen.

Keywords: Functional MRI (fMRI), BOLD contrast, Cerebral Blood Flow, Perfusion-weighted MRI, Neuroimaging

6.1 Introduction

The underlying mechanism and quantification of the blood oxygenation level dependence (BOLD) signal are of great interest, yet still under intense research. The magnitude of BOLD signal measured by functional MRI (fMRI) is the result of complex interplay among three physiology changes of cerebral blood flow (CBF), cerebral blood volume (CBV) and cerebral metabolic rate for oxygen consumption ($CMRO_2$) [37, 101-103]. From the standpoint of the magnetic resonance physics, BOLD associated with the susceptibility change will affect the transverse relaxation times (T_2) or apparent T_2 (T_2*), thus, resulting in a signal change in the T_2/T_2*-weighted MRI. In contrast, the CBF change and inflow effect associated with the stimulus-induced blood circulation change will affect the apparent longitudinal relaxation time (T_1) of the brain tissue water, in particular, when the blood water exchanges rapidly with the brain tissue water through capillaries. The T_1 change can result in a MRI signal variation under the MRI acquisition condition with short repetition time (TR) and/or a relatively large radiofrequency (RF) pulse flip angle, because of so-called magnetization saturation effect. Under this circumstance (an acquisition condition for most fMRI studies), the total fMRI signal change elevated by brain stimulation or physiology change depends on not only T_2/T_2*-sensitive BOLD effect but also T_1-sensitive flow-related effect. The relative contributions between them depend on many factors, such as magnetic field strength, types of MRI pulse sequence, MRI acquisition parameters, vessel architectures and orientation inside

the magnet, and blood velocity [102, 104-109]. Nevertheless, it is still not fully understood whether the flow-related component could significantly contribute to the total fMRI signal change, and if it could, how much contribution is from micro-vascular blood circulation or perfusion change?

The primary goals of this study were: i) to quantitatively investigate the relative contributions of 'true" BOLD effect and flow-related effect to the total fMRI signal increase detected by gradient-echo echo planar imaging (GE-EPI) in the rat brain cortex induced by mild hypercapnia (6% CO_2) at 9.4T; ii) to identify the major source of the flow-related signal contribution to the total fMRI signal change induced by hypercapnia; and iii) to further test the flow-related contribution to fMRI signal change with varied TRs in the human primary visual cortex during visual stimulation at 4T.

6.2 Theory

GE-EPI is one of the most popular MRI sequences used to perform fMRI studies due to its rapid imaging acquisition and high BOLD contrast-to-noise ratio. The theory described herein focuses on GE-EPI pulse sequence, nevertheless it can be extended to other types of MRI sequences (e.g., spin-echo EPI). The GE-EPI signal intensity, S(GE), can be described as:

$$S(GE) = S_0 \cdot \exp(-TE \cdot R_2^*) \cdot \sin(\alpha) \frac{1-\exp(-TR \cdot R_1)}{1-\cos(\alpha) \cdot \exp(-TR \cdot R_1)} \qquad (6.1)$$

where $R_2^*(=1/T_2^*)$ is the apparent transverse relaxation rate which is sensitive to the susceptibility effect and BOLD; $R_1(=1/T_1)$ is the apparent longitudinal relaxation rate which is sensitive to flow-related signal changes; α is the flip angle of excitation readout

RF pulse; TE is the echo time; S_0 is the GE-EPI signal intensity when TE=0, α= 90° and under fully relaxed condition (TR ≥ $5T_1$). It is known that the cerebral blood circulation changes during brain stimulation or under the hypercapnia condition could induce not only the true BOLD effect but also an increase in R_1 due to rapid magnetization exchange between labeled and non-labeled water spins [32, 33, 37, 38, 110]. The shortened T_1 (or accelerated R_1) process in the brain tissue water associated with the blood flow increase leads to a reduction in the saturation effect on the measured MRI signal under the MRI acquisition condition with relatively short TR and/or large α, subsequently resulting in an extra increase in GE-EPI signal intensity which is superimposed onto the total fMRI signal. When TR>>4-5 T_1 and TE>0, the term of exp(-TR×R_1) approaches to zero and Eq.(6.1) can be rewritten as:

$$S(GE) = S_0 \cdot \exp(-TE \cdot R_2^*) \cdot \sin(\alpha) \tag{6.2}$$

under this condition, *S(GE)* becomes independent on R_1 and it is solely determined by R_2* and its change mainly reflects a "true" BOLD effect.

In the following section, we discussed the quantity of GE-EPI signal change induced by hypercapnia, though the same relationship can be applied to other situations, e.g., brain activation. The total GE-EPI signal change (SC_{total}) can be quantified by the GE-EPI signals acquired under control (normocapnia, S_{ctrl}) and hypercapnia (S_{hyper}) condition according to Eqs. (6.3) to (6.4):

$$SC_{total} = \frac{S_{hyper}}{S_{ctrl}} \tag{6.3}$$

$$= \frac{S_0 \cdot \exp(-TE \cdot R_2^{*}') \cdot \sin(\alpha) \dfrac{1-\exp(-TR \cdot R_1')}{1-\cos(\alpha)\cdot\exp(-TR \cdot R_1')}}{S_0 \cdot \exp(-TE \cdot R_2^{*}) \cdot \sin(\alpha) \dfrac{1-\exp(-TR \cdot R_1)}{1-\cos(\alpha)\cdot\exp(-TR \cdot R_1)}}$$

$$= \exp[-TE(R_2^{*}' - R_2^{*})] \cdot \frac{[1-\exp(-TR \cdot R_1')]\cdot[1-\cos(\alpha)\cdot\exp(-TR \cdot R_1)]}{[1-\exp(-TR \cdot R_1)]\cdot[1-\cos(\alpha)\cdot\exp(-TR \cdot R_1')]} \tag{6.4}$$

$$= SC_{BOLD} \cdot SC_{Flow} \tag{6.5}$$

where R_2*' and R_1' are the apparent transverse relaxation rate and the apparent longitudinal relaxation rate, respectively, measured under the hypercapnia condition. The first term in Eq. (6.4) only depends on the R_2* change, thus, reflects the relative "true" BOLD contribution (i.e., the term of SC_{BOLD} in Eq. (6.5)) to the total GE-EPI signal change. In contrast, the second term in Eq. (6.4) relies on R_1 and its change, thus, reflects the flow-related contributions from in-flow effect and/or perfusion change (i.e., the term of SC_{Flow} in Eq. (6.5)). Under the fully relaxed condition ($SC_{Flow} \approx 1$), the total GE-EPI signal change measured between normocapnia and hypercapnia conditions relies only on BOLD effect and it equals to the "true" BOLD signal change (i.e., SC_{BOLD} in Eq. (6.5)).

However, for the TR regime of << $5T_1$, the total GE-EPI signal change becomes sensitive to both BOLD-related (R_2*) and flow-related (R_1) effects. The relative contributions between these two physiology effects depend on GE-EPI acquisition parameters, in particular, TR and α. Eq. (6.5) can be further approximated by Eq. (6.6) when the percent signal changes caused by BOLD effect (ΔS_{BOLD}) and flow-related effect

(ΔS_{Flow}) during hypercapnia are in a small range of few percents and the cross term of $\Delta S_{BOLD} \cdot \Delta S_{Flow}$ becomes negligible:

$$\begin{aligned} SC_{total} &= SC_{BOLD} \cdot SC_{Flow} = (1 + \Delta S_{BOLD}) \cdot (1 + \Delta S_{Flow}) \\ &= 1 + \Delta S_{BOLD} + \Delta S_{Flow} + \Delta S_{BOLD} \cdot \Delta S_{Flow} \\ &\cong 1 + \Delta S_{BOLD} + \Delta S_{Flow} \end{aligned} \tag{6.6}$$

Equation (6.6) suggests that the total GE-EPI signal change during hypercapnia can be simply considered as the linear addition of the percentage signal changes contributed from BOLD and flow-related effects. Nevertheless, the flow-related R_1 change could be attributed to two sources: one is perfusion change that is desired for fMRI mapping and another one is undesired in-flow effect from large vessels (e.g., arteries).

It is of great importance to examine if the major flow-related contribution to the total GE-EPI signal change induced by physiology perturbation is from perfusion or large vessels. One effective way to test this question is to apply diffusion-weighting bipolar gradients incorporated into the GE-EPI imaging sequence, thus, to suppress the in-flow effect in the large vessels with higher blood velocity but with negligible effects on the perfusion at the capillary level [111-113]. Several studies have demonstrated that the diffusion-weighted fMRI with an adequate diffusion gradient strength has the characteristic of selectively attenuating the intravascular fMRI signal from moving water spins in both arterial and venous sides, thus more closely reflecting the BOLD responses in capillary beds. As a result, it is been suggested that diffusion-weighted images help to improve the spatial and temporal accuracy for mapping neuronal activation [77, 79]. The

degree of the attenuation (A) on the measured GE-EPI signal can be quantified by Eq(3.1) and (3.2) and the explanation of parameters therein.

Since a large *b* factor tends to significantly suppress the MRI signal contribution from large vessels with fast blood flow velocity [77, 80], the measured fMRI signal becomes more dominant by smaller arterioles, capillaries and brain tissue. Moreover, it has been demonstrated that the fMRI signal acquired at high magnetic field with high *b* factors (>1000 $s \cdot mm^{-2}$) and a relative long TE had negligible contributions from large vessels, and thus extravascular (or tissue) component becomes a dominant contribution.

In the present study, a large *b* factor up to 1019 $s \cdot mm^{-2}$ was applied to measure diffusion-weighted GE-EPI data under normocapnia and hypercapnia conditions at 9.4T. The fMRI results with zero and higher b factors were compared for testing major source of flow-related signal contribution to the total GE-EPI signal change measured in the absence of diffusion weighting gradients.

6.3 Materials and Methods

6.3.1 Animal Preparation and MRI Measurements

The male Sprague-Dawley rats were anesthetized and intubated using 5% (v/v) isoflurane in a N_2O:O_2 (60/40) gas mixture. Both femoral arteries and the left femoral vein were catheterized for physiological monitoring and blood sampling. After the surgical operation, the rat was placed in a home-built cradle incorporating ear bars and a bite bar to reduce head movement and ensure proper positioning inside an animal MRI scanner. The animal anesthesia was maintained at 2% isoflurane. Rectal temperature was

maintained at 37.0±0.5ºC by a circulating water heating blanket. The inspired and expired gases and blood pressure were monitored constantly. The rate and volume of ventilation were adjusted to maintain normal physiology condition determined by blood gas data.

The MRI measurements were performed under control (normocapnia) condition and stable hypercapnia condition, which was induced by switching to an inhalation bag with mixed gases (6% CO_2, 34% O_2, 58% N_2O and 2% isoflurane) for 20-30 minutes.

Animal MRI experiments were conducted on a 9.4T horizontal animal magnet (Magnex Scientific, Abingdon, UK) interfaced to a Varian INOVA console (Varian, Palo Alto, CA, USA). A butterfly-shape surface coil (long axis of 2.8 cm and short axis of 2.0 cm that is parallel to the animal spine) was used to collect all MRI data. Scout images were acquired using a turbo fast low angle shot (TurboFLASH) imaging sequence with the acquisition parameters: TR = 10 ms, TE = 4 ms, image slice thickness = 1 mm, field of view (FOV) = 3.2 cm×3.2 cm; image matrix size = 128×128. The single-shot GE-EPI pulse sequence was applied for collecting fMRI data using the acquisition parameters of FOV=3.2cm×3.2cm; matrix size = 64×64; three continuous, coronal image slices with 1 mm slice thickness; TE: 22-24 ms; 30 ms for acquiring each EPI slice and no extra delay between sequential, multiple-slice EPI acquisitions; and six variable TRs (1.1, 2.1, 3.1, 5.1, 8.1 and 12.1 s) arranged in a randomized fashion. A number of GE-EPI with varied RF pulse power was scanned under fully relaxed condition. These image data were used for two purposes: to optimize the GE-EPI signal-to-noise ratio (SNR) in the region of interest and to quantify the spatial profile of RF pulse flip angle, α, used in Eqs. (6.1) to (6.4). The GE-EPI sequence was further incorporated to the global saturation recovery

pulse segment using a non-slice-selective half-passage adiabatic RF pulse followed by spoiling gradients for imaging apparent T_1 with nine saturation-recovery times (T_{SR}: 0.008, 0.1, 0.2, 0.3, 0.4, 0.5, 1.4, 3, 10 s). One of the advantages of saturation recovery T_1 measurement method is that there is no waiting time needed among sequential imaging acquisitions with varied recovery times because the initial magnetization is always forced to approach zero after the saturation preparation. This merit can lead to relatively high temporal resolution, for instance, approximately 16 s in this study for obtaining one entire T_1 image volume.

Bipolar diffusion gradients in three dimensions were also inserted between the GE-EPI excitation pulse and data acquisition, i.e., within the gradient echo time. Three *b* factors (0, 518, 1019 $s \cdot mm^{-2}$) were achieved by adjusting the diffusion gradient strength up to 45 gauss/cm. Duration of diffusion gradient, δt, was 2.5 ms and the time delay between the bipolar diffusion gradients, *T*, was 3.6 ms.

All animal experiments were conducted under the protocol approved by the University of Minnesota Institutional Animal Care and Use Committee.

6.3.2 Human Visual Stimulation MRI Measurements

Six healthy human subjects (three males and three females, 23-49 years old) were recruited in this study and one subject participated twice on different days. The fMRI experiments were performed on a 4T/90-cm bore human magnet (Siemens, Erlangen, Germany) system with the Varian INOVA console (Varian Inc., Palo Alto, CA, USA) using a single-loop RF surface coil (10 cm diameter) located near the occipital lobe. The

subjects laid supine in the magnet and the head motion was limited with a foam-padded head holder. During the fMRI activation task periods, an 8-Hz, full-field reversal checkerboard visual stimulation was displayed on a mirror housed a comfortable distance above the subject's eyes. Scout images were acquired using a T_1-weighted TurboFLASH imaging sequence (TR=10 ms, TE=3.8 ms, slice thickness=5 mm, image matrix size = 128×128, FOV=20cm×20cm). Based on the anatomic images, five continuous, coronal slices covering most of the calcarine fissure of the human primary visual cortex (V1) were selected to acquire fMRI data using the GE-EPI sequence (TE=30 ms; FOV=20cm×20cm; image matrix=64×64; 5 mm thickness; 100 ms for acquiring each EPI slice and no extra delay between sequential, multiple-slice EPI acquisitions) with varied TRs. The block-paradigm fMRI studies consisted of four control periods and three task periods were carried out in an interleaved way. Fifteen images volumes were performed in each period for TR = 1.1 or 2.1 seconds fMRI experiments, while 10 images volumes each period for TR = 4.1 or 9.1 seconds fMRI experiments, resulting in an total acquisition time of 2, 4, 5 and 10 minutes for TR = 1.1, 2.1, 4.1, 9.1 seconds experiments, respectively. GE-EPI combined with the saturation-recovery preparation was used for imaging apparent T_1 with nine varied saturation-recovery times of 0.02, 0.1, 0.2, 0.3, 0.4, 0.5, 1.4, 3 and 10 s under both resting and stimulation conditions. Each T_1 image measurement took 1.6 minutes. In addition, a number of GE-EPI with varied RF pulse powers were also scanned under fully relaxed condition to determine the flip angle, α, in the primary visual cortex.

All human experiments were conducted under the protocol approved by the

University of Minnesota Institutional Review Board.

6.3.3 Data Processing, MRI Signal Simulation and Statistics

All the MRI data analysis was performed using the STIMULATE software package (Stimulate, Center for Magnetic Resonance Research, University of Minnesota, USA) [69] and the Matlab software package (The Mathworks inc., Natick, MA, USA). For the animal experiments, fourteen rats (body weight: 345±73g) having normal physiology condition and showing positive BOLD change during hypercapnia were analyzed and summarized. Nonlinear least-square fitting program using the Matlab software was applied to perform the T_1 regression analysis, and small delays between multiple fMRI slices acquisitions were accounted for determining the saturation-recovery times. Regression accuracy was estimated using the sum squared error (sse) and the square of regression coefficient (R^2).

For the human studies, the fMRI activation maps were generated using the period cross correlation method with the boxcar reference function and a cross correlation coefficient of ≥ 0.4 [114]. The brain region of interest (ROI) covering the activated pixels in the visual cortex based on the fMRI maps measured with shortest TR (= 1s) were used to perform the R_1 regression, comparison of GE-MRI signal percent increases among the fMRI data with varied TRs and to determine the excitation flip angle α in the primary visual cortex.

Flow-related signal change (i.e., SC_{Flow} in Eq. (6.5)) in the rat brain as a function of TR ranged from 0 to 13 s, flip angle α ranged from 40 to160°, and R_1' increasing from 0.485 to 0.52 s^{-1} (based on the experimental data of rat brain tissue at 9.4T [41, 62, 93,

115] was simulated according to the second term of Eq. (6.4) without taking the susceptibility (R_2*) contribution into account. Saturation recovery T_1 (R_1) data taken from a ROI located in the rat sensory cortical region excluding large surface vessels and sinus vein were used to perform the R_1 regression analysis. The inter-subject averaged T_1 (R_1) value under normocapnia conditions, T_1' (R_1') value under hypercapnia conditions and α value in the identical ROI used for calculating R_1 and R_1' were applied to simulate and predict total GE-EPI signal change as a function of TR according to Eq. (6.4) assuming $SC_{BOLD} = 1$.

The GE-EPI signal intensities measured with varied TR under normocapnia and hypercapnia conditions were averaged from multiple GE-EPI pixels within the ROI for each animal, and the outcomes were used to calculate the total GE-EPI signal change induced by hypercapnia as a function of TR according to Eq. (6.3)**.** The average flip angle of α within the ROI was numerically determined from a number of GE-EPIs with a serial of RF power acquired under fully relaxed condition. Finally, the simulated TR dependence of flow-related signal contribution was regressed using the least square error fitting method to the experimental results of the total fMRI BOLD change for comparison.

Contrast-to-noise ratio (CNR) for determining the total GE-EPI signal change induced by hypercapnia is defined as:

$$CNR = \frac{S_{hyper} - S_{ctrl}}{\sigma_0} \tag{6.9}$$

where S_{hyper} and S_{ctrl} are the signal intensity at a given TR under hypercapnia and normocapnia, respectively; σ_0 is the mean of standard deviation of background noise of control images and is TR independent. Contrast-to-noise ratio per unit measurement time (CNR*) is described as:

$$CNR* = CNR \cdot \sqrt{n} \tag{6.10}$$

where n is the number of repeated image acquisitions with a desired TR within a fixed period of measurement time. Both CNR and CNR* as a function of TR were calculated based on experimental GE-EPI data or simulated using known variables. For considering practical fMRI application for mapping brain physiology changes, σ_0 in Eq. (6.9) was replaced by the brain image signal fluctuation ($\sigma_{0\text{-}SF}$) that was measured under the normocapnia condition at a given TR with the same total acquisition time (one minute); and the calculated CNR ratio was denoted as CNR**.

Multiple ANOVA statistical analysis was performed to compare the total fMRI signal changes with varied TRs within ROI under different *b* factors. The results are presented as mean±standard deviation (SD) or standard error, and a *p* value of < 0.05 is considered to be statistically significant.

6.4 Results

Figure 6.1a displays the simulation results of flow-related signal increase (i.e., SC_{Flow} in Eq. (6.5)) and its dependence on TR, flip angle and R_1 change caused by hypercapnia based on the rat brain hypercapnia data measured at 9.4T. In general, shortening TR or increasing flip angle α and R_1' results in a larger percent signal change

owing to the consequential reduction of saturation effect following a flow increase during hypercapnia. Figure 6.1b shows the comparison results between the predicted total GE-EPI signal changes based on the simulation using the measured parameters (R_1, R_1', flip angle, "true" BOLD percentage change, i.e., SC_{BOLD} in Eq. (6.5)) and the experimentally measured total GE-EPI signal increase (i.e., attributing to both BOLD and flow-related components) induced by hypercapnia as a function of TR under three different diffusion-weighting conditions. This figure was generated in two steps. First, the total fMRI signal changes were calculated according to Eq. (6.3) using the directly measured GE-EPI data under varied diffusion weighting as a function of TR (i.e., full cycles in Fig. 6.1b). Secondly, the flow-related signal change as a function of TR was simulated and predicted by using the experimentally measured values of average $\alpha(=103\pm18°)$, R_1 and R_1' (see Table 3.1) according Eq. (6.4) under each diffusion-weighting condition; then this predicted signal change was superposed on the "true" BOLD signal that was measured with a long TR of 12.1 s ($> 5T_1$), resulting in the predicted plots under varied diffusion weighting conditions as a function of TR (i.e., solid lines in Fig. 6.1b). There is a good agreement between the experimental results and predicted results under three diffusion-weighting conditions. These comparison results support the rationale that the total GE-EPI signal change induced by hypercapnia could be well described as a linear combination of the "true" BOLD signal and the flow-related signal as described by Eq. (6.6).

The highlighted blue area drawn in Fig. 6.1b illustrates one example of the flow-related signal increase above the "true" BOLD signal measured under nearly fully relaxed

condition in the absence of diffusion weighting gradients (i.e., $b = 0$). The relative signal contribution from the flow-related component increased substantially when shortening TR, and it became comparable to the "true" BOLD at TR ≈ 1 s.

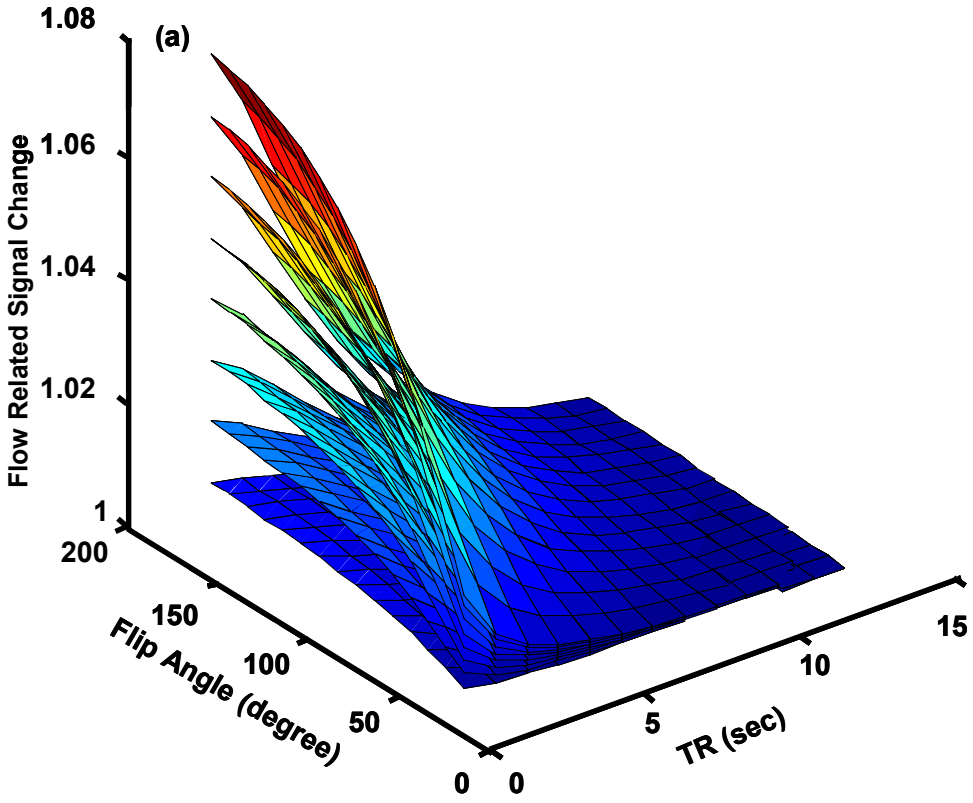
(a)
Flow Related Signal Change
1.08
1.06
1.04
1.02
1
200
150
100
50
0
Flip Angle (degree)
0
5
10
15
TR (sec)

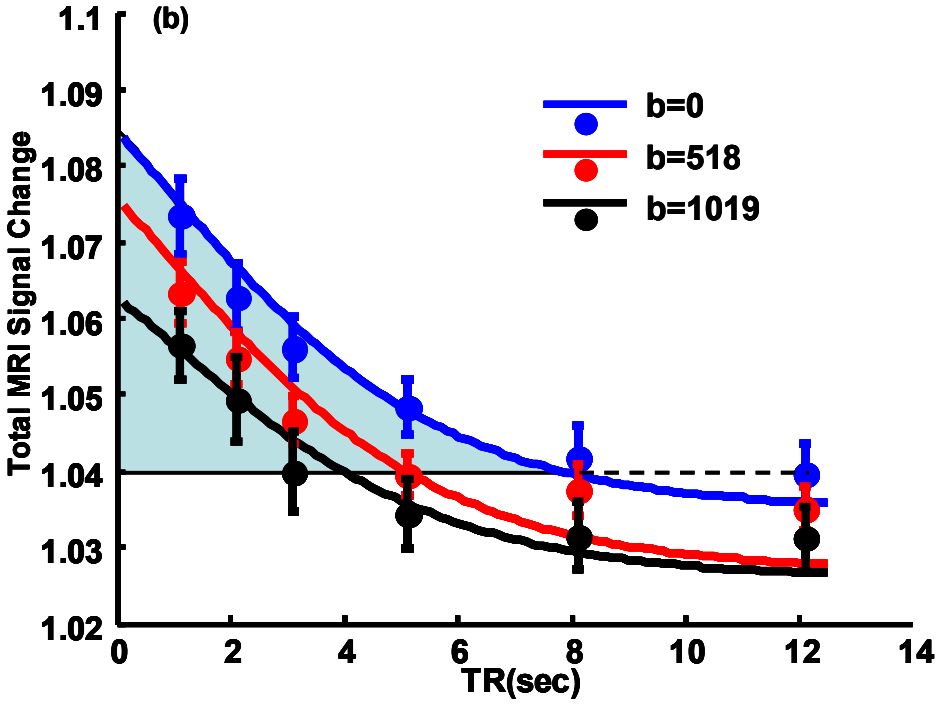
(b)
Total MRI Signal Change
1.1
1.09
1.08
1.07
1.06
1.05
1.04
1.03
1.02
b=0
b=518
b=1019
0
2
4
6
8
10
12
14
TR(sec)

Figure 6.1 (a) Simulation results of flow-related signal increase (SC_{Flow}) as a function of TR, flip angle and ΔR_1. Simulation parameters: R_1=0.48 s^{-1}; bottom layer R_1'=0.485 s^{-1}; top layer R_1'=0.52 s^{-1}; layer incremental step ΔR_1=0.005 s^{-1}; flip angle ranges from 40 to160°. (b) Comparison of total fMRI signal (SC_{total}) changes elevated by hypercapnia as a function of TR between the GE-EPI measurement results (full cycles and standard error bars, n=21 for b=0 $s \cdot mm^{-2}$, n=18 for b=518 $s \cdot mm^{-2}$ and n=11 for b=1019 $s \cdot mm^{-2}$) and the predicted results (color lines) using the experimentally measured R_1 and R_1' values as well as flip angle $\alpha=103^0$ according to Eq. (6.3). The light blue area under the solid blue line represents the increased signal contribution from perfusion and possibly inflow effect in the absence of the bipolar diffusion gradients.

Due to the application of diffusion gradients, the total GE-EPI signal changes at a given TR were statistically different among three *b* factors ($p \leq 0.04$ based on multiple ANOVA statistical analysis). Specifically, when the *b* factor increased, the total GE-EPI signal change reduced approximately in a parallel manner for different TRs. This trend is also evident in Fig. 6.2a, which shows a coronal anatomical brain image and its corresponding percent change maps of total GE-EPI signal increase during hypercapnia with varied diffusion gradient strengths and TRs from a representative rat. The measured total GE-EPI signal increase became smaller when the diffusion gradient strength was large at a given TR or when TR was longer at a fixed diffusion gradient strength. For example, the BOLD signal measured at TR = 12 s in the rat brain was higher in the absence of diffusion gradient than that with the application of bipolar diffusion gradients (see Figs. 6.1b and 6.2a). Nevertheless, no matter whether the diffusion gradient was applied, the total GE-EPI signal change increased more with TR = 1 sec than that with TR = 5 sec and 12 sec. Figure 6.2b shows the discrepant trend of the total GE-EPI signal change as a function of TR at different depth of cortical region of interest from the

cortical surface. It indicates that the total GE-EPI signal change in the deep cortical region is more sensitive to TR than that of superficial cortical region mixed with large vessels. This result suggests a different extent of susceptible behavior of fMRI signal as a function of TR between superficial large vessels and capillaries in the brain tissue.

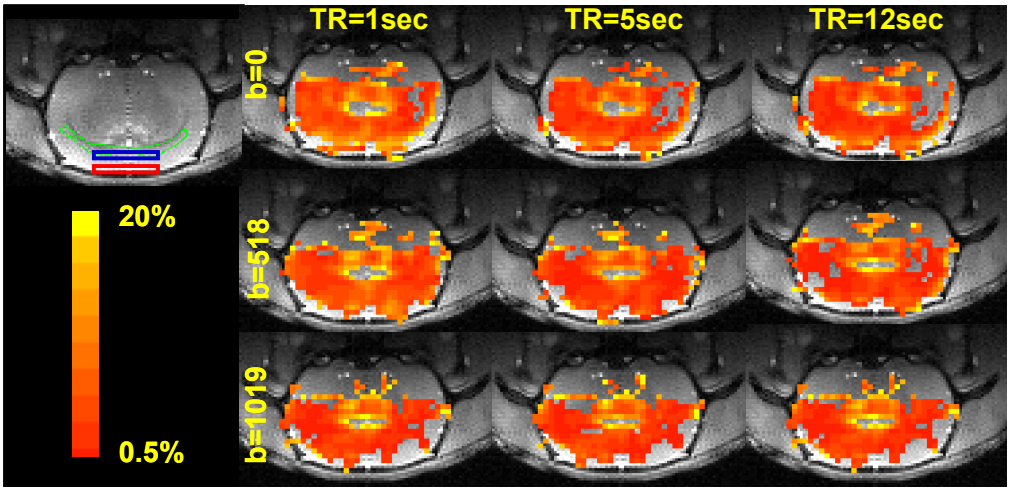

(a)

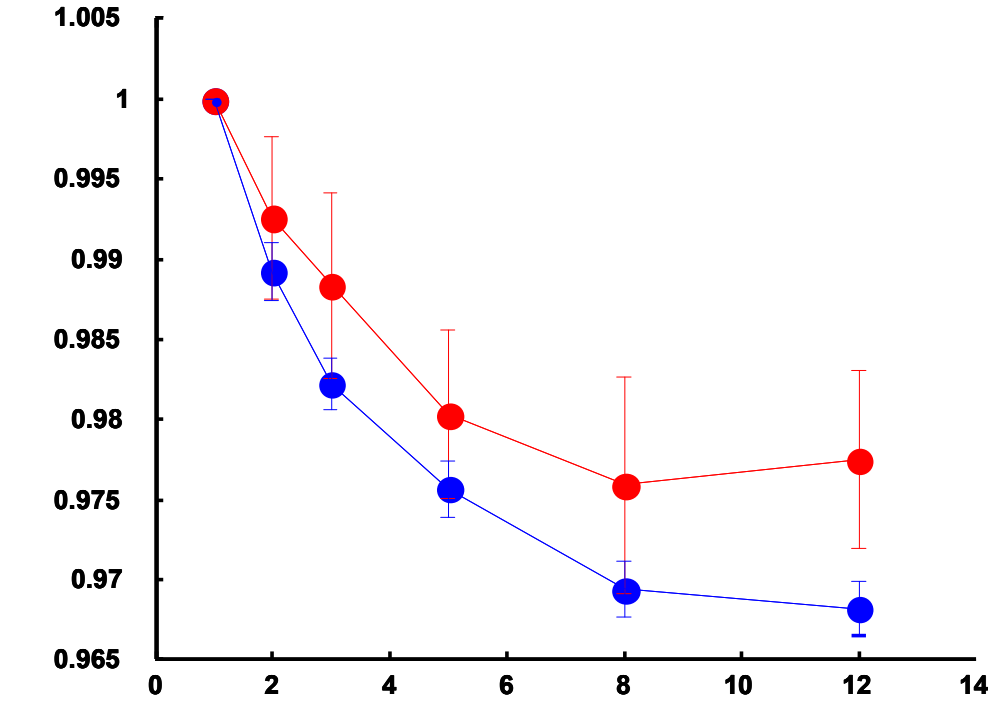

(b)

Figure 6.2 (a) Coronal anatomic brain image and its GE-MRI percent change maps during hypercapnia

with varied b factors and TRs in a representative rat. The region of interest enclosed in the green line resided in the coronal anatomy image was used to derive R_1 and fMRI signal change. The blue and red boxes indicate the deep and surface cortical ROIs used in (b). (b) MRI signal change ratio (normalized by the ratio at TR = 1 s) and standard error bars (n=14) during hypercapnia as a function of TR at different ROI layers.

Chapter 3 Table 3.1 summarizes the mean and standard deviation results of the apparent longitudinal relaxation rates measured during normocapnia (R_1) and hypercapnia (R_1') using three different diffusion-weighting *b* factors. It shows R_1 significantly increased ($p<0.001$) during hypercapnia in the presence or absence of diffusion gradients, however, no statistical difference was found among the three conditions with varied diffusion-weighting factors either for normocapnia (R_1, $p = 0.80$) or hypercapnia (R_1', $p = 0.29$) condition. These results indicate that the macro-vascular flow contribution to the measured R_1 is negligible for the rat brain at 9.4T.

Figure 6.3a shows the averaged CNR, CNR* and CNR** results based on the GE-EPI measurements under the hypercapnia condition with different TRs. If one assumes that image noise was theoretically independent of TR [109], highest CNR appeared at moderate TR (~3 sec, see the blue bars in Figure. 6.3a). However, shorter TRs had a significant advantage for gaining a higher CNR acquired per unit time (i.e., CNR*, see the red bars in Figure. 6.3a) through signal averaging, even though the gain could be slightly compromised by the physiological fMRI signal fluctuation (i.e., CNR**, see the yellow bars in Figure. 6.3a). For example, CNR* at TR = 1s was 3.7 times higher than that at TR = 12 s, in contrast, CNR** was 2.2 times. This observation is not surprising since CNR* was determined by the thermal noise (σ_0), while CNR** was determined by

the sum of thermal and physiological noises ($\sigma_{0\text{-}SF}$). Nevertheless, both CNR* and CNR** show the similar dependence on TR.

Figure 6.3b shows the simulation results of CNR and CNR* as a function of TR, suggesting a similar trend as the experiment results as displayed in Figure. 6.3a. These figures indicate that the optimal CNR* peak appears around TR = 1s. When TR is shortened than 1s, CNR* could further benefit from more signal averaging and enhanced flow-related signal increase, however the CNR* gain is unable to compensate the substantial loss of GE-EPI signal due to severe saturation effect by a very short repetition time.

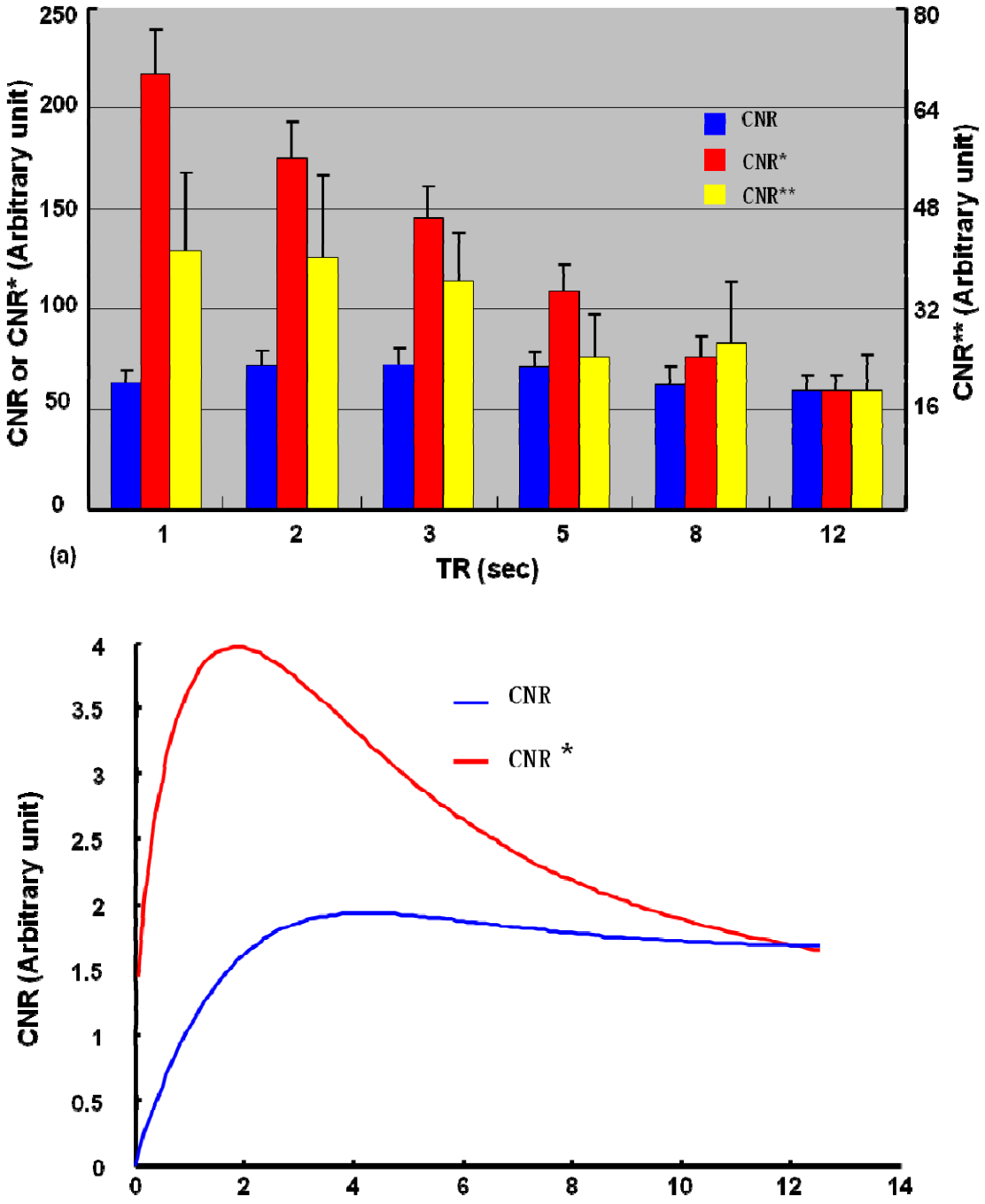

Figure 6.3 (a) Average results of CNR, CNR* and CNR** and their standard deviations (n=14 for CNR and CNR*; n=8 for CNR**) in the ROIs of rat sensory cortex at different TRs without the diffusion gradients. (b) Simulation results of CNR and CNR* versus TRs. Simulation parameters: TE: 23 ms; T_2* and R_1 during normocapnia are 27 ms and 0.48 s^{-1}; T_2*' and R_1' during hypercapnia are 28.3 ms and 0.50 s^{-1}; flip angle is 103°, TR starts from 0 to 12.5 s with a step of 0.1 s, standard deviation of background noise

was treated as an arbitrary constant. TR:repetition time; CNR, contrast-to-noise ratio; ROIs, region of interest, TE, echo time.

Figure 6.4a presents the five coronal fMRI activation maps of the human visual cortex in response to visual stimulation obtained with four TRs from a representative subject, showing a significant GE-EPI signal increase in the activated brain regions. It also indicates that both the number of activated pixels with the same statistical threshold and the percent change of total fMRI signal elevated by visual stimulation inside the ROI declined as TR increased. Figure 6.4b summarizes the average results showing the changes in total number of activated pixels and the percentage of GE-EPI signal increases at varied TRs and their standard error among the seven studies. The mean of total signal increase was 3.0%, 2.7%, 2.1% and 1.8% for TR = 1, 2, 4 and 9 s, respectively. The averaged flip angle for the activated pixels based on the fMRI maps acquired with TR = 1s was 85±3°. The averaged R_1 (or T_1) under control condition in those pixels was 0.625±0.007 s^{-1} (1.6 s), this value is consistent with previous reports [116, 117]. It changed to 0.629±0.007 s^{-1} (1.58 s) under the visual stimulation condition due to the elevated perfusion.

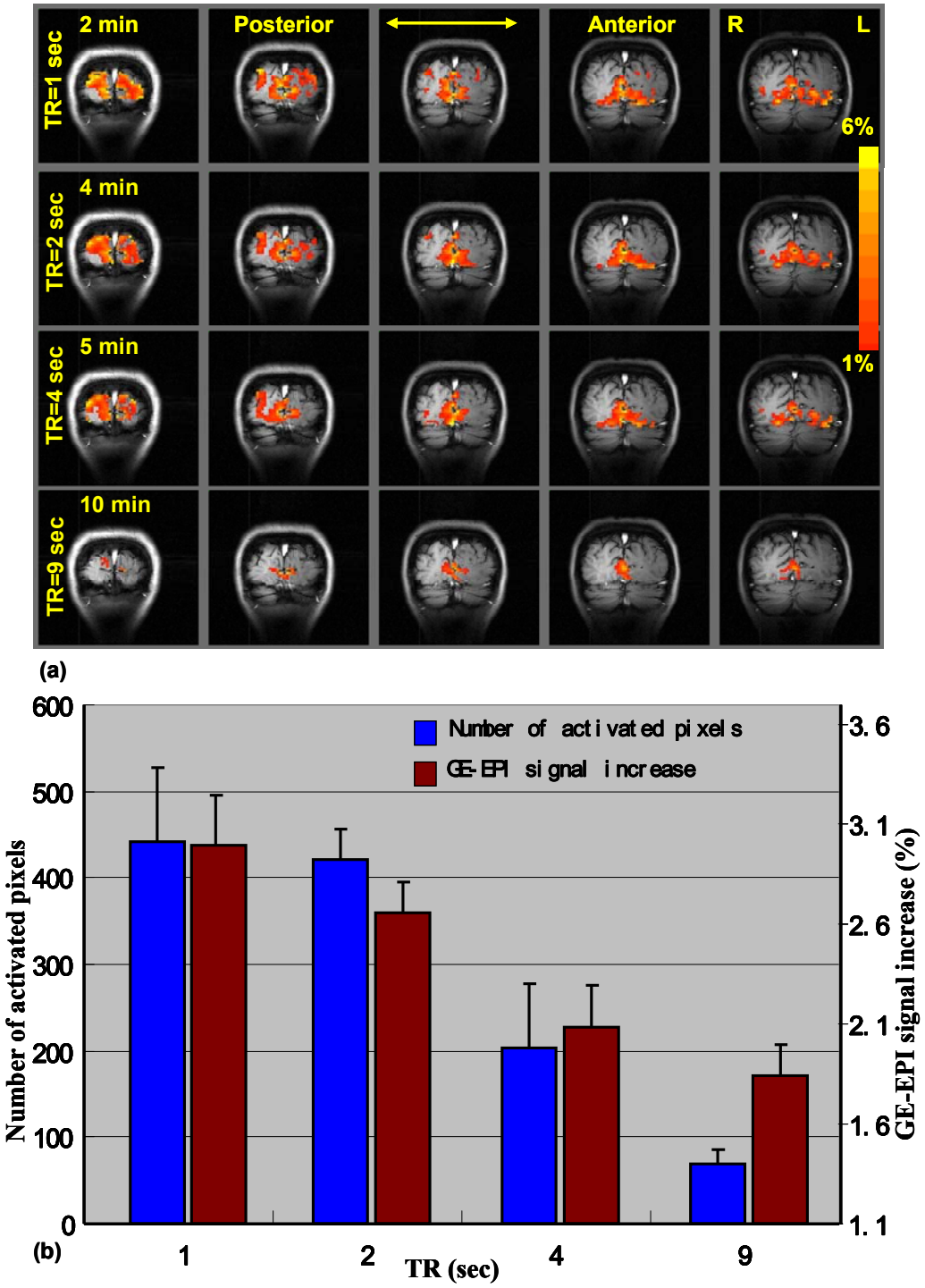

Figure 6.4 (a) Visual stimulation activation maps with varied TRs for continuous five fMRI slices in a representative human subject. The number of activated pixels and the magnitude of the total fMRI signal change decrease as TR increases. The total acquisition time for each TR is indicated on the top of images in the left column. (b) Summary of the number of total activated pixels and GE-EPI signal increase during

visual stimulation and their standard error bars as a function of TR (n=7).

6.5 Discussion and Conclusion

6.5.1 Enhancement of Flow-related Contributions to fMRI Signal using Short TR

The attenuated magnetization saturation effect is the main underlying mechanism for explaining the significantly enhanced flow-related contribution on the total GE-EPI signal increase as observed during hypercapnia/stimulation. Since the apparent longitudinal relaxation rate increased from approximately 0.48 s^{-1} at control to 0.50 s^{-1} (see Chapter 3 Table 3.1) in the rat cortex during hypercapnia, the longitudinal magnetization relaxed more rapidly (i.e., less saturated) during hypercapnia than normocapnia condition, resulting in an increase in the detected GE-EPI signal during hypercapnia when the GE-EPI was acquired under non-fully relaxed condition. Such a signal recovery can become substantial when a much short TR is applied. Consequently, the ratio of the GE-EPI signals between hypercapnia (or stimulation) and normocapnia (or control) conditions increases when TR shortens. This ratio change is attributed to the flow-related effect on R_1, since the "true" BOLD is independent of TR. This flow-related effect can become surprisingly significant. For instance, the total GE-EPI signal (percentage) increases measured with TR=1s (7.4%, 6.6% and 5.8% under *b* factor 0, 518 and 1019 $s \cdot mm^{-2}$, respectively) are approximately twice larger than that with a long TR of 12 s (4%, 3.6%, 2.8% under *b* factor 0, 518, 1019 $s \cdot mm^{-2}$, respectively). The differences in the GE-EPI signal percentage increases measured between short TR (= 1 second) and long TR (= 12 seconds) reflect the contribution from the enhanced flow-related

component, which is superimposed onto the "true" BOLD signal measured at TR = 12 seconds. When TR was 1 second, the flow-related signal increase accounted for 46%, 45%, and 52% of the total GE-EPI signal increase in response to hypercapnia under three diffusion-weightings *b* factors of 0, 518 and 1019 $s \cdot mm^{-2}$, respectively.

A similar result was observed in the human fMRI study using visual stimulation. Not only more activation pixels passed the statistic threshold when a short TR was used but also higher magnitudes of fMRI signal change were observed (Figure. 6.4). For instance, the total GE-EPI signal increase (3%) at TR = 1s is almost twice as large as that with TR = 9s (1.8%). This indicates a substantial flow-related contribution in fMRI signal with a short TR ($<< 5T_1$), which is a common case for the majority of human fMRI applications. This TR dependent flow-related effect could not only influence the total fMRI signals investigated in the present study but also possibly complicate other types of functional MRI measurements, for instance, using the Vascular-Space-Occupancy (VASO) technique for imaging cerebral blood volume change during brain activation [118]. A longer TR is preferred to accurately interpreting VASO contrast because the blood null times at different brain states are closer than that with short TRs.

6.5.2 Flow-related Contributions from Macro- and Micro-vascular Compartments

Close examination of R_1 and total GE-EPI signal changes induced by hypercapnia with various diffusion-weighting gradient strengths provides further evidence for supporting the notion that the flow-related contribution to the total GE-EPI signal increase is likely dominated by micro-vascular components including capillaries and

possibly some small arterioles and venules. This is evident from several lines as discussed in the following.

The magnitude of total GE-EPI signal change consistently decreases with the increased *b* factor. This result is in agreement with other fMRI reports from rat sensory stimulation study [119], cat visual stimulation study [120] to human visual stimulation study [105, 113, 121, 122]. This observation is not surprising because it is known that the bipolar diffusion gradients tend to suppress the macro-vascular fMRI signal contributions from both arteries and veins. It is interesting to note that although the intravascular water signal from veins becomes considerably small at 9.4T due to its short T_2^* ($\approx$ 9 ms, [123]) and a relatively long TE (=23 ms) applied to acquire the GE-EPI data in the present study, its contribution to the total GE-EPI signal change is not completely negligible at 9.4T. This is evident from the observation showing consistent, though small, suppression of "true" BOLD effect measured with a long TR ($> 5T_1$) in the presence of strong diffusion-weighting gradients as illustrated in Figures. 6.1b and 6.2a.

In contrast to the "true" BOLD dependence on the diffusion gradient strength, the flow-related signal behaves differently. The general relationship between the flow-related GE-EPI signal change and TR does not change significantly by the use of diffusion weighting gradients, even with a large *b* factor of 1019 $s \cdot mm^{-2}$ (see Figure. 6.1b and Figure. 6.2). In another word, the reduction of saturation effect due to the acceleration of apparent R_1 relaxation rate during hypercapnia is hardly being suppressed by the diffusion gradients at short TR, suggesting that the flow-related contribution is likely from micro-vascular compartment or capillary origin.

This notion is also supported by the results of R_1 measurements as summarized in Chapter 3 Tables 3.1. The R_1 values measured under both normocapnia and hypercapnia conditions were found to be independent of *b* factor (one way ANOVA p=0.80 at normocapnia and p=0.29 at hypercapnia). This result suggests that the inflow effect from macro-vascular compartment may not significantly influence the R_1 values and its change in the rat cortical regions in response to hypercapnia; otherwise the apparent R_1 values should be expected to decline as the diffusion-weighting increases for suppressing flowing water signals.

The stronger dependence of TR for the total GE-EPI signal increase in the deep cortical region than that of the superficial cortical region in response to hypercapnia shown in Figure. 6.2b also indicates that the flow-related enhancement dominantly originated from micro-vascular components. The absolute R_1 value of deep cortical region was significantly larger ($p < 0.01$) than that of surface cortical region under both normocapnia (0.475±0.002 s^{-1} vs. 0.457±0.002 s^{-1}, n=14) and hypercapnia (0.498±0.002 s^{-1} vs. 0.477±0.003 s^{-1}, n=14) conditions since the latter region made up of more large vessel blood water spins than the former region. Interestingly, the R_1 difference (ΔR_1) between the normocapnia and hypercapnia in the deep cortical region was also larger than that in the surface cortical region (0.023±0.002 s^{-1} vs. 0.021±0.002s^{-1}, n=14). This small but statistically significant ΔR_1 ($p = 0.02$) between these two brain regions was consistent with the simulation results in Figure. 6.1a, which shows that the larger ΔR_1 should lead to a larger GE-EPI signal increase. In fact, the difference in the trend of the normalized fMRI signal ratio (S_{hyper}/S_{ctrl}) as a function of TR between the deep cortical

region and the surface region shown in Figure. 6.2b could become larger if the fMRI signals in these two regions were acquired with the same flip angle, since the large flip angle in the surface area tends to "magnify" fMRI signal change.

The human baseline CBF value and its increase during visual stimulation can be estimated using a previously proposed method [74, 124] and the ΔR_1 value measured in the present study. Specifically, the absolute CBF increase (ΔCBF) was calculated according to:

$$\Delta CBF = \Delta R_1 \times \lambda \times C = 0.22 \text{ ml/g/min} \qquad (6.11)$$

where λ is the tissue blood partition coefficient for water (= 0.9ml/g), C is a unit conversion factor (=60 s/min) and ΔR_1=0.004 s^{-1} for the human visual stimulation study. This CBF increase was corresponding to a percentage CBF increase of 40-50% as reported in the literature, thus, resulting in a baseline CBF value of 0.43-0.54 ml/g/min that is coincident with the majority of results reported in the literature [1-3]. This comparison suggests a close relationship between R_1 and CBF. This also corroborates with the theory we deduced in Chapter 2, CBF change during the functional stimulation could be quantitatively calculated using SR-T_1 method.

The overall results support that the flow-related signal enhancement on the total fMRI signal is likely originated from the extravascular compartment and the perfusion change occurring at the capillary level, although the inflow effect from small arterioles near capillaries cannot be completely excluded.

6.5.3 Impact and Complication

The findings from this study have several impacts. Majority of fMRI applications are conducted with a relatively short TR for improving temporal resolution and gaining SNR and/or CNR through signal averaging. In the present study, we demonstrate that the shortening TR could significantly enhance the flow-related signal contribution to the total fMRI signal and increase CNR, thus, improving the fMRI sensitivity for mapping brain physiology and neuronal activity changes.

Moreover, fMRI signal acquired with short TRs could significantly improve the specificity for functional mapping of neuronal activity change because the flow-related signal enhancement is likely originated from capillary perfusion and/or small arteriole inflow effect (at least at high field), reflecting micro-vascular blood flow processing which is closer to the neuronal activation site than the draining veins. Therefore, fMRI should benefit substantially from the improvements in both CNR*/CNR** and functional mapping specificity due to the enhanced signal from micro-vascular contribution simply by using an optimal and short TR in combination with a relatively large RF pulse flip angle. One potential and interesting application is to detect the fMRI signal change dominated by the perfusion-related contribution by using ultra-short echo-time (UTE) image methods with negligible BOLD (or T_2/T_2*) contribution due to extremely short TE in combination with extremely short TR. This combination could provide perfusion-based fMRI maps without the use of artery spin labeling preparation.

This study reveals that the fMRI BOLD signal commonly detected with a relatively short TR does not only reflect the pure BOLD effect, but rather is composed of

the "true" BOLD (T_2/T_2*) and flow-related (T_1) components. This nature complicates BOLD quantification, in particular, to the BOLD calibration modeling commonly used to determine the relative change of the cerebral metabolic rate of oxygen consumption in response to brain stimulation based on the hypercapnia calibration [73]. If the total fMRI signal change contains significant contribution from flow-related signal or perfusion contribution that is usually not considered in the calibration, it will lead to an overestimation of "true" BOLD signal, ultimately, an underestimation of percent change of $CMRO_2$, although this error could be partially compensated by using the identical fMRI acquisition parameters for acquiring both hypercapnia calibration and functional activation data.

Several aspects of potential limitation need to be taken into account. First, the flow-related fMRI signal contribution measured in the brain might have dependence on the orientation of fMRI slices relative to the blood flow direction, for instance, the coronal fMRI slice in the rat brain is perpendicular to the blood flow direction in the large or medium sized vessels while it becomes parallel in the human brain. However, the flow-related fMRI signal enhancement observed in the present study was likely dominated by the micro-vascular component or perfusion in the capillaries, which could be approximately considered as random distribution in space, therefore it should not be sensitive to the orientation between blood flow direction and fMRI slices.

One possible confounding factor in determining the apparent T_1 (or R_1) values using the saturation-recovery approach is related to the arterial transit time, i.e., the traveling time of the blood water from the boundary between the saturated and non-

saturated regions to the fMRI slices. The water magnetization recovery after the saturation preparation may not simply follow the identical exponential recovery function when the saturation-recovery time is shorter than the arterial transit time, in which the exchange between the fresh flowing water spin and the tissue water in the fMRI slice has not occur, as compared to a saturation-recovery time longer than the arterial transit time. (see Chapter 2 Eq. 2.11 and 2.14) The arterial transit time is expected to be much shorter, especially for the rat brain, than the range of saturation-recovery times applied in the R_1 measurements. The RF surface coils were applied in this study and their RF saturation profiles were mainly limited to the brain, thus further shortened the effective artery transit time. When the saturation-recovery time is longer than the arterial transit time, the image signal follows an exponential recovery of R_1. In contrast, the signal recovery function becomes more complicated when the saturation-recovery time is shorter than the arterial transit time. Nevertheless, the R_1 regression based on a single exponential recovery function still provides a good approximation for the rat study owing to the short arterial transit time, prolonged and similar values of apparent brain tissue T_1 ($=1/R_1$) and intrinsic artery blood T_1 at high magnetic field. These facts reduced the R_1 measurement errors caused by the confounding factor. This is evident by the small sum squared errors (see chapter 1) of R_1 regression and excellent linearity showing in the semi-log plots (Figure 6.5) of the magnetization recovery signal versus saturation-recovery time.

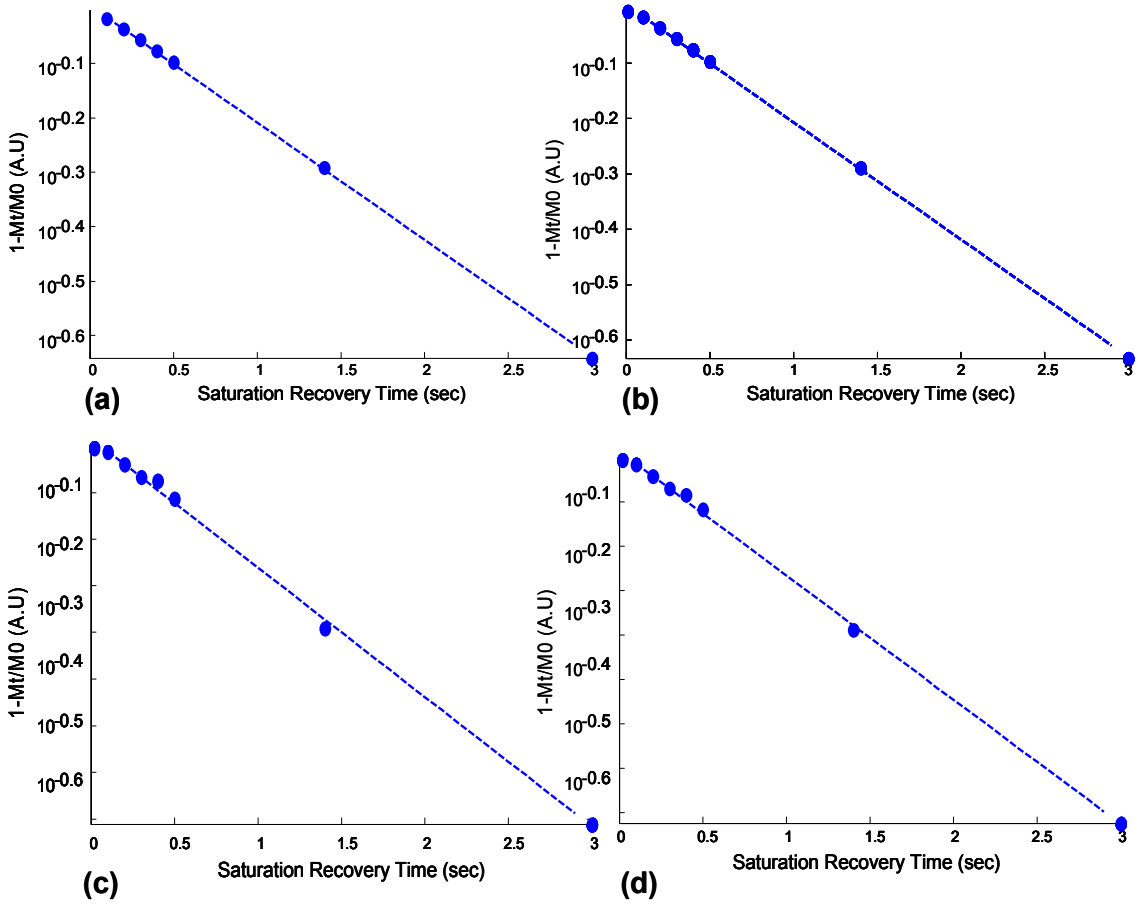

Figure 6.5 The semilog plots of GE-signal 1-S(t)/S_0 versus saturation recovery time. (a) and (b) show the data of two represent rats. (c) and (d) show the data of two represent human subjects. S(t) represents signal intensity at a certain saturation recovery time t; S_0 is the GE-EPI signal intensity when TE=0, α= 90° and under fully relaxed condition (TR ≥ $5T_1$).

Another potential confounding factor in quantifying the relative flow-related contribution in the total fMRI signal is related to multiple-slice fMRI acquisition. The slice-selective excitation RF pulse for obtaining multiple-slice EPIs could disturb the water spin magnetization within the EPI slice and cause a post-acquisition effect on the sequentially acquired EPI slices, in particular, when the delay time between the adjacent

EPI slice acquisitions is long. To reduce this confounding factor, we applied a short single-slice EPI acquisition time (30 ms for the rat study and 100 ms for the human study) to minimize the total acquisition time for collecting the entire multiple-slice EPI volume.

In summary, our study demonstrates that the flow-related contribution originated from extra-vascular component and perfusion can be utilized to significantly enhance fMRI signal and contrast-to-noise ratio, and to improve the spatial specificity for mapping activation sites by using optimal repetition time and RF pulse flip angle. The nature of mixed BOLD and flow-related contributions to the total fMRI signal has a crucial implication on BOLD quantification and $CMRO_2$ calculation. Finally, it should be feasible to separate and quantify the "true" BOLD and perfusion-related signals based on two fMRI measurements: one with a short TR and another under the full relaxation condition.

CHAPTER 7 A comparison Study of Imaging Absolute CBF Change in Transient MCAO Rat Brain Using the SR-T_1 Method and the CASL Technique

7.1 Introduction

Cerebral blood flow (CBF) and its dynamic change are extremely important to brain function, metabolism, and tissue viability associated with many diseases. The saturation-recovery T_1 (SR-T_1) method provides a noninvasive and effective tool for monitoring rat brain CBF change and other useful information as well such as blood-oxygen-level dependent (BOLD) signal and basal CBF simultaneously [74, 86, 96]. However, this method was only applied to either the normal rat brain or global four-vessel occlusion in the previous studies, and its efficacy, sensitivity and reliability in the preclinical diseased model has not been tested.

Stroke is one of the leading cerebral vascular diseases of death and long-term disability in the United States, and its animal model and clinical stroke trials are an active area of research. In this study, we aim to: i) imaging CBF increase in response to the mild hypercapnia in varied lesion regions of the middle cerebral artery occlusion (MCAO) rat brain with the SR-T_1 method, and compare it with that measured using the continuous arterial spin labeling (CASL) technique; ii) to differentiate the T_1 change caused by the blood flow deficit and the pathological evolution other than CBF deficit in the post-ischemic rat brain; iii) to study reperfusion damage of MCAO rat brain longitudinally by

combining varieties of techniques and image modalities, such as the T_2-weighted images, apparent diffusion coefficient (ADC) images, cerebral vascular reactivity (CVR) maps and Hematoxylin and eosin (H.E) stained histology of lesion rat brain.

7.2 Theory

7.2.1 Absolute CBF change calculation with the SR-T_1 measurement

See Chapter 4.2.1

7.2.2 Baseline CBF and absolute CBF change calculation with the CASL technique

See Chapter 4.2.2

7.2.3 ADC calculation

The degree of the attenuation (A) on the measured GE signal can be quantified by Eq. (3.1), therefore, the ADC value can be calculated by:

$$ADC = \frac{1}{b_1 - b_2} \cdot \ln \frac{S(b_2)}{S(b_1)} \qquad (7.1)$$

where b_1 and b_2 are two different diffusion weighting factors which is determined by incorporating the amplitude and timing parameters of the diffusion gradients according to Eq. (3.2). $S(b_1)$ and $S(b_2)$ are corresponding GE signal intensities.

7.2.4 CVR calculation

CVR is a valuable physiologic property of assessing brain arteries response to vasoactive challenge. It could be evaluated by positron emission tomography (PET) [125,

126], single-photon emission computed tomography (SPECT) [127, 128] and transcranail Doppler (TCD) ultrasonography[129-131]. More recently, it has also been assessed by fMRI BOLD response and ASL CBF calculation (Review paper and reference cited therein[132]). ASL-CBF based CVR [132, 133]can be computed by:

$$CVR_{ASL} = \frac{100}{CBF_{normo}} \cdot \frac{CBF_{hyper} - CBF_{normo}}{PetCO_{2\text{-}hyper} - PetCO_{2\text{-}normo}} \tag{7.2}$$

where CBF_{hyper} and CBF_{normo} are the CBF under hypercapnia and normocapnia conditions respectively, $PetCO_{2\text{-}hyper}$ and $PetCO_{2\text{-}normo}$ are the end-tidal CO_2 concentrations under hypercapnia and normocapnia conditions.

7.3 Material and MRI Method

7.3.1 MCAO rat model preparation

The rat MCAO model was induced with a transfemoral microwire approach. [134, 135] Briefly, under the guidance of fluoroscopy and through a femoral artery access, the microwire was navigated into the internal carotid artery (ICA) of the rat and occluded the tip of the right or left MCA for 1 hour. This MCAO model has the advantages of simplicity of operation, minimal invasion, reproducible outcome and high survive rate. Sham surgery was also performed with the similar procedure by inserting the microwire into the ICA and withdrawing the wire without actual occlusion. All surgical procedures

and experimental protocols were approved by the Institutional Animal Care and Use Committee of University of Minnesota.

7.3.2 Experiment protocols and MRI sequences and parameters

Ten MCAO rats (body weight: 384±45g) were scanned on day 1 and six of them were repeated on day 7 after 1-hour occlusion. T_2-weighted images and diffusion-weighted images were scanned under normocapnia condition (34% O_2, 64% N_2O and 1.8% isoflurane) only. The rat CBF change was induced with the mild hypercapnia (6% CO_2, 34% O_2, 58% N_2O and 1.8% isoflurane) and was measured with both the SR-T_1 method and the CASL technique directly. All the R_1 images and CASL based CBF measurements were acquired before (i.e., normocapnia or control) and during hypercapnia condition when the animal physiology was within a normal range. The rats were sacrificed on day 7 after the MRI scan and transcardially perfused with fixative 4% paraformaldehyde in phosphate buffered saline (PBS) for H.E. stained histology. The brain regions with partially and completely damaged neurons were carefully delineated by an experienced pathologist.

MRI experiments were performed at a 9.4T/31cm magnet interfaced with VNMRJ consoles (Varian, CA). A butterfly-shape ^1H surface coil (long axis of 2.8 cm and short axis of 2.0 cm that is parallel to the animal spine) was used to collect all MRI data. A separate 8-shaped coil (1cm diameter) was used for carotid arterial spin labeling experiment [90]. The distance between the labeling plane and the brain image slice was adjusted to about 2cm to minimize the interaction between the tagging and head RF coils.

The T_2-weighted images were acquired with a fast spin echo sequence (TE=10ms; TR=4sec; FOV=3.2×3.2cm; matrix=256×256; thickness=1 mm; 8 echo train length). Bipolar diffusion gradients in three dimensions were inserted between the GE excitation pulse and data acquisition to obtain the diffusion images (TE=14ms; TR=250ms; FOV=3.2×3.2cm; image matrix=128×128; 1 mm thickness). Two *b* factors (b_1=10.8 and b_2=1007 $s \cdot mm^{-2}$) were used for obtaining apparent diffusion coefficient (ADC) maps according to Eq.7.1 with δt = 2.5 ms and T = 3.6ms.

Gradient echo EPI (TE=17ms; FOV=3.2×3.2cm; image matrix=64×64; 1 mm thickness) combined with the saturation-recovery preparation was used for imaging T_1 with 32 varied T_{SR} values range from 0.011 to 12s. A modified TurboFLASH sequence (TE=30ms; TR=3sec; FOV=3.2×3.2cm; image matrix=64×64; 1 mm thickness) was used for the CASL experiment. The duration of the RF labeling pulse was 2.2 second. The absolute CBF change equals to the CBF values obtained at hypercapnia condition minus the CBF values derived at normocapnia condition.

7.3.3 Data processing and statistics

MRI data analysis was performed using the Matlab software package. ROIs data taken from the rat somatosensory cortex, peripheral area of lesion (ADC and R_1 values decrease on day 1 and ADC value normalizes on day 7) and core lesion region (ADC and R_1 values decrease on day1 and ADC value increases on day 7) at the ipsilateral (or lesion) side as well as the homologous ROIs of contralateral (normal or control) side were used to perform the R_1 regression analysis and to determine R_1, ΔR_1 and subsequently delta CBF (ΔCBF). Baseline CBF and ΔCBF was also calculated with the

CASL technique using the identical ROIs as in the SR-T_1 method and compared with the ΔCBF calculated using the latter method. Finally, the T_1 images, CBF images generated with the CASL technique, ΔCBF maps created with the SR-T_1 method as well as the CASL technique, ADC and CVR maps that overlapped on the corresponding anatomic images were generated for each animal at each scan time. Paired t-test was applied to compare R_1, ADC, CBF, ΔCBF obtained between the different ROIs at the lesion side and the corresponding ROIs at the contralateral side, as well as ΔCBF calculated with both the SR-T_1 method and the CASL technique. One-way ANOVA and multiple comparison procedure were carried out to compare R_1, CBF, ΔCBF values calculated among varied lesion regions at either the lesion or control side.

7.4 Results

7.4.1 T_2-weighted images, ADC images, R_1 images, CBF and CBF change images in MCAO rat brain on day 1 and day 7 after the occlusion

Figure 7.1 show three continuous brain slices of the T_2-weighted images, ADC images, R_1 images and CBF images (under both normocapnia and hypercapnia conditions), delta CBF images induced by hypercapnia generated with the SR-T_1 method as well as with the CASL technique in two representative rats scanned on day 1 (a and b) and days 7 (c and d) post-occlusion. In general, the lesion area looks similar in all these image modalities. The T_2-weighted images show hyper-intensity on mostly the subcortex and some cortex area at the lesion side on both day 1 and day 7 post-occlusion. Compared with the T_2-weighted images on day 1, the hyper-intensity lesion area on day 7

appears smaller, the intensity is less uniform and the margin is less clear, which indicates the absorption and improvement of the pathological process. The characteristics (uniformity and margin of the lesion) of the R_1 images are similar to T_2-weighted images, except for the intensity of lesion area showing hypo-intensity instead of hyper-intensity in the T_2-weighted images.

On day 1 of the 1 hour post-occlusion, ADC in the peripheral and core area is decreased, however, its value in the peripheral area is recovered and ADC in the core area increases on day 7 of post-occlusion. Interestingly, the peripheral lesion area of the ipsilateral side shows higher CBF than the control side under normocapnia condition in some of the MCAO rats on day 1 after the occlusion, however, such area does not respond to the hypercapnia challenge. In addition, for the CBF images acquired on day 7, the peripheral lesion area of the ipsilateral side reveal more prominent CBF than the control side under the normocapnia and starts to respond to hypercapnia. The delta CBF values (Table 7.1) and spatial pattern of delta CBF images calculated with the SR-T_1 and CASL methods are very consistent on day 1 and reasonably close on day 7 after the occlusion. The delta CBF images between hypercapnia and normocapnia conditions created with either the SR-T_1 method or with the CASL technique represents the vascular response to vasoactive challenge (CO_2), showing the compromised CBF increase area mainly locates in the peripheral and core lesion area, no matter the baseline CBF of these lesion areas is higher or lower than the control side. However, its size shown in delta CBF images seems larger (extends to the somentosensory cortex more) than the lesion region displayed in the T_2-weighted images, ADC images and even R_1 images at day 1

after the occlusion. On day 7 after the occlusion, this compromised CBF increase area appears much smaller than shown on day 1.

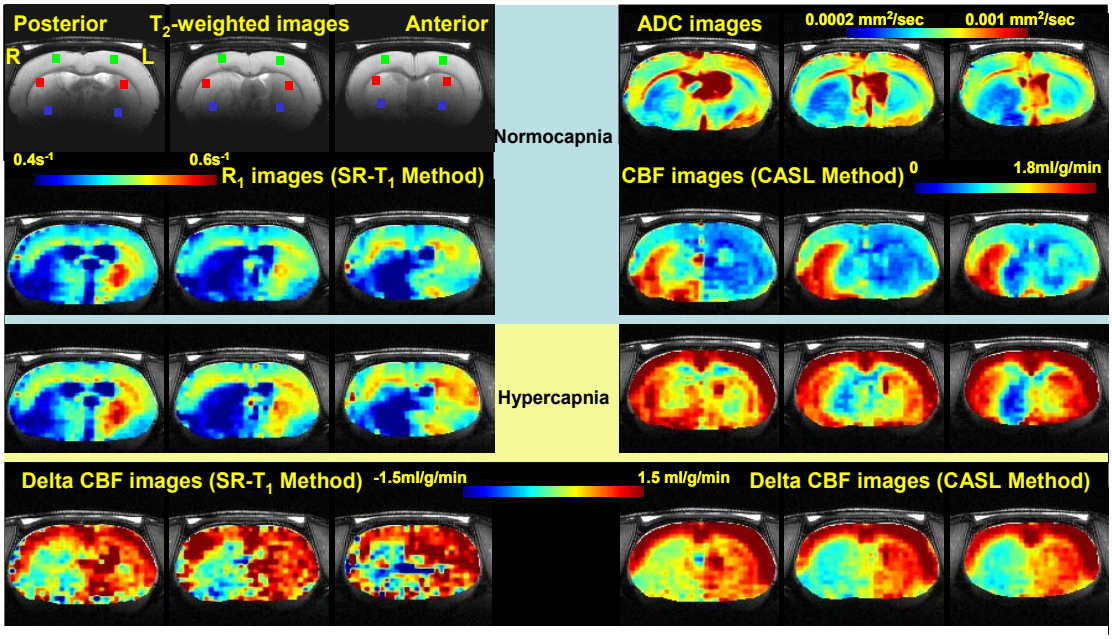

(a)

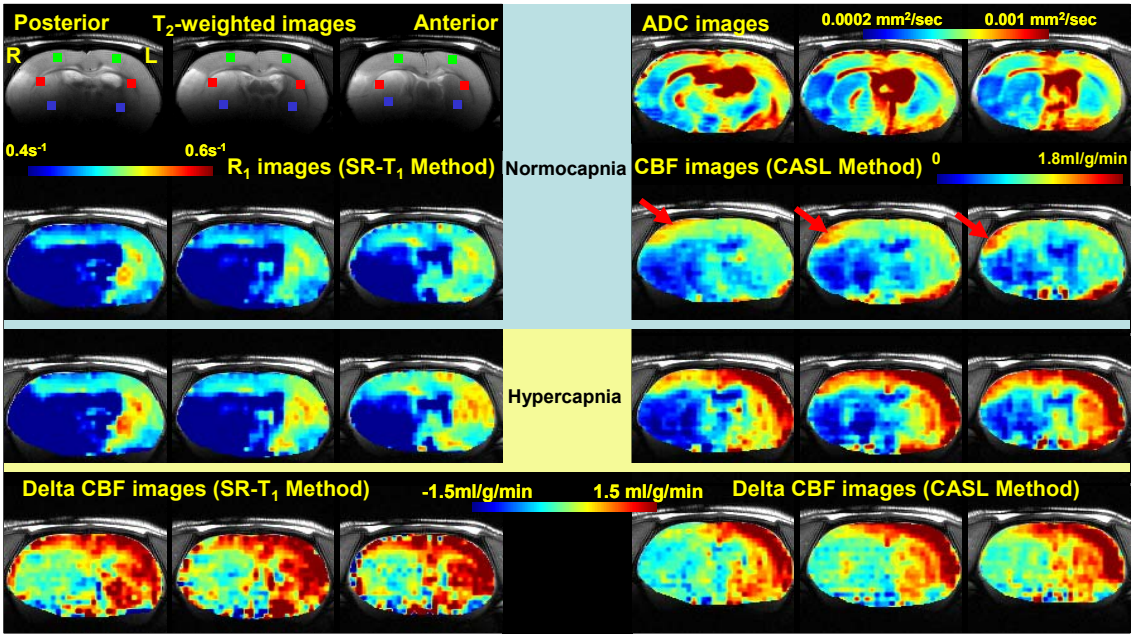
Posterior
T2-weighted images
Anterior
R
L
ADC images
0.0002 mm²/sec
0.001 mm²/sec
0.4s-1
0.6s-1
R1 images (SR-T1 Method)
Normocapnia
CBF images (CASL Method)
0
1.8ml/g/min
Hypercapnia
Delta CBF images (SR-T1 Method)
-1.5ml/g/min
1.5 ml/g/min
Delta CBF images (CASL Method)

(b)

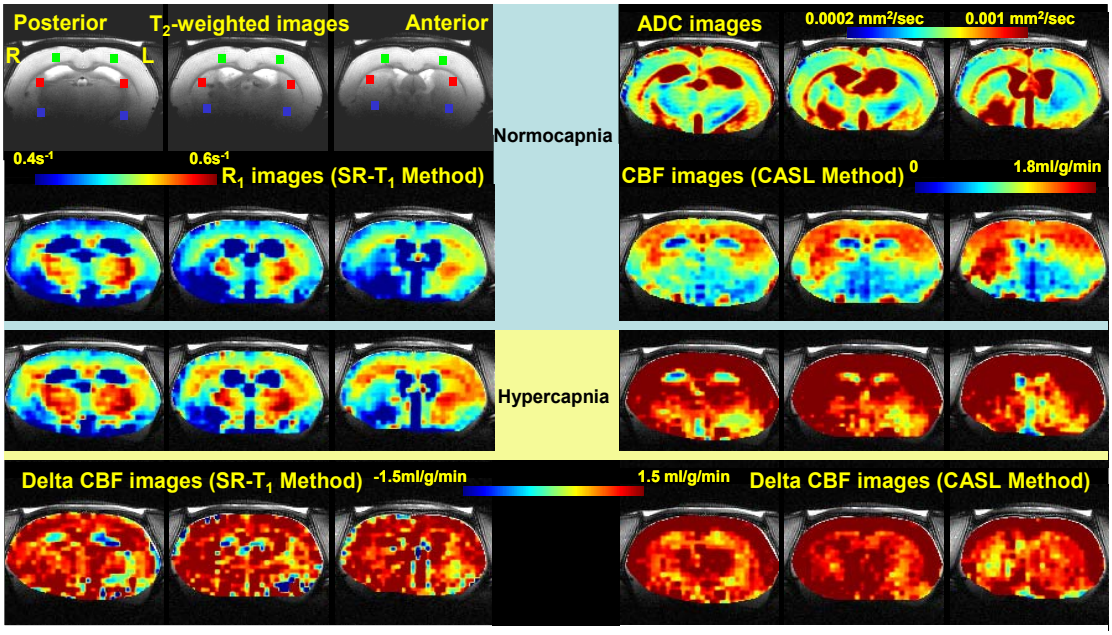
Posterior
T2-weighted images
Anterior
R
L
ADC images
0.0002 mm²/sec
0.001 mm²/sec
0.4s-1
0.6s-1
R1 images (SR-T1 Method)
Normocapnia
CBF images (CASL Method)
0
1.8ml/g/min
Hypercapnia
Delta CBF images (SR-T1 Method)
-1.5ml/g/min
1.5 ml/g/min
Delta CBF images (CASL Method)

(c)

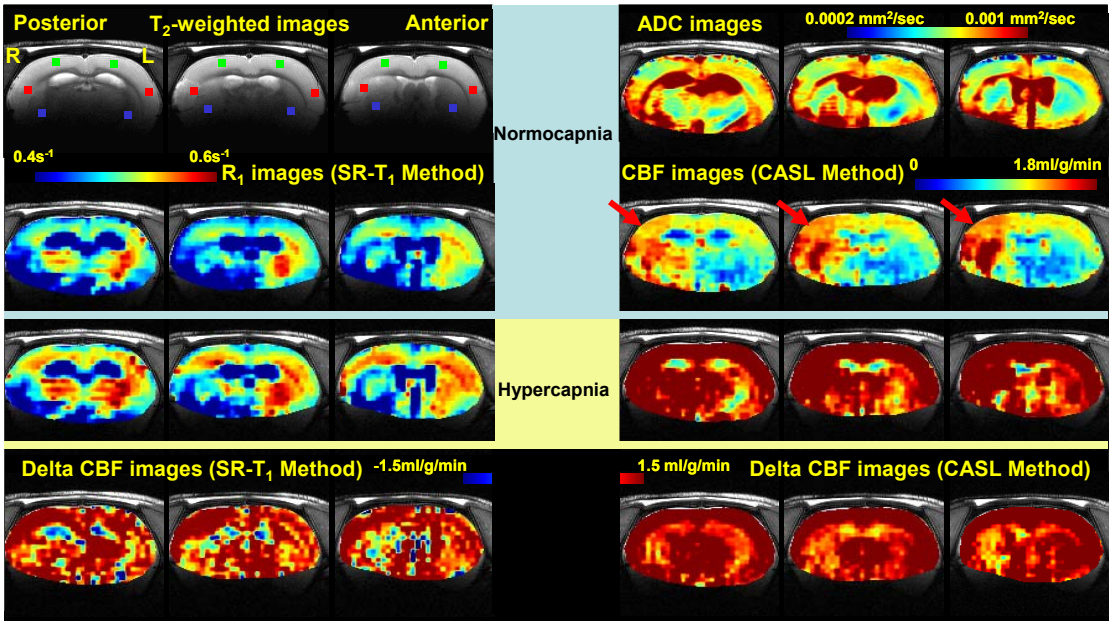

(d)

Figure 7.1 Three continuous coronal brain slices of the T_2-weighted images, ADC images, R_1 and CBF images (under both normocapnia and hypercapnic conditions), delta CBF images induced by hypercapnia generated with the SR-T_1 method as well as with the CASL technique in two representative rats scanned on day 1(a and b) and day 7(c and d) after 1 hour MCA occlusion. The color squares overlapped on the T_2-weighted images are symbolic ROIs at cortex, peripheral lesion area and core lesion area at ipsilateral (lesion) side and corresponding ROIs of the contralateral (control) side.

7.4.2 R_1, delta R_1, CBF, CBF change and ADC values in varied lesion ROIs in MCAO rat brain on day 1 and day 7 after the occlusion

The average of absolute R_1 values of the rat brain cortex, peripheral lesion area and core area measured on day 1 (and day 7) after 1 hour MCA occlusion are 0.492±0.015, 0.448±0.035 and 0.382±0.036 s^{-1} (and 0.488±0.009, 0.486±0.030 and 0.424±0.047 s^{-1} on 7 days) under the normocapnia condition at 9.4T respectively; while

R_1 values in the corresponding area at the control side are 0.495±0.009, 0.519±0.011 and 0.507±0.019 s^{-1} (and 0.489±0.008, 0.515±0.016 and 0.526±0.046 s^{-1} on day 7) respectively. The discrepancy of the R_1 values between the lesion side and the control side reflects the underlying pathophysiology change and therefore the brain tissue spin-lattice relaxation time alteration at the lesion side subsequent to the CBF disturbance.

Figure 7.2 shows on day 1 (n=10) and day 7 (n=6) after the occlusion the mean and standard deviation of R_1, delta R_1 (a and b for day 1 while e and f for day 7), CBF and delta CBF (c and d for day 1 while g and h for day 7) at cortex (17±8 pixels), peripheral area (12±8 pixels) and core lesion (8±4 pixels) on both lesion side (a, c, e and g) and control side (b, d, f and h). On day 1 after the occlusion, there are statistic significant difference of R_1, delta R_1, CBF and delta CBF in cortex, peripheral area and core lesion area between lesion side and control side, except for the cortical R_1 under normocapnia condition and cortical as well as peripheral baseline CBF under both normocapnia and hypercapnia conditions. On day 7 after the occlusion, statistic significant difference is found only between the R_1 of the core area at the lesion side and that in its homologous ROI at the control side. When comparing either R_1 or CBF among different regions at the lesion side under normocapnia condition on both day 1 and day 7 post-occlusion, R_1 shows statistic difference among varied lesion region while no significantly statistic difference is found in the baseline CBF, indicating that the R_1 images are potentially more sensitive to the extent of lesion than CBF images. Clearly, the delta R_1 and delta CBF at the lesion side are significant smaller than that at the

control side on day 1 after the occlusion; and the pattern of delta R_1 and delta CBF is consistent at both lesion side and control side.

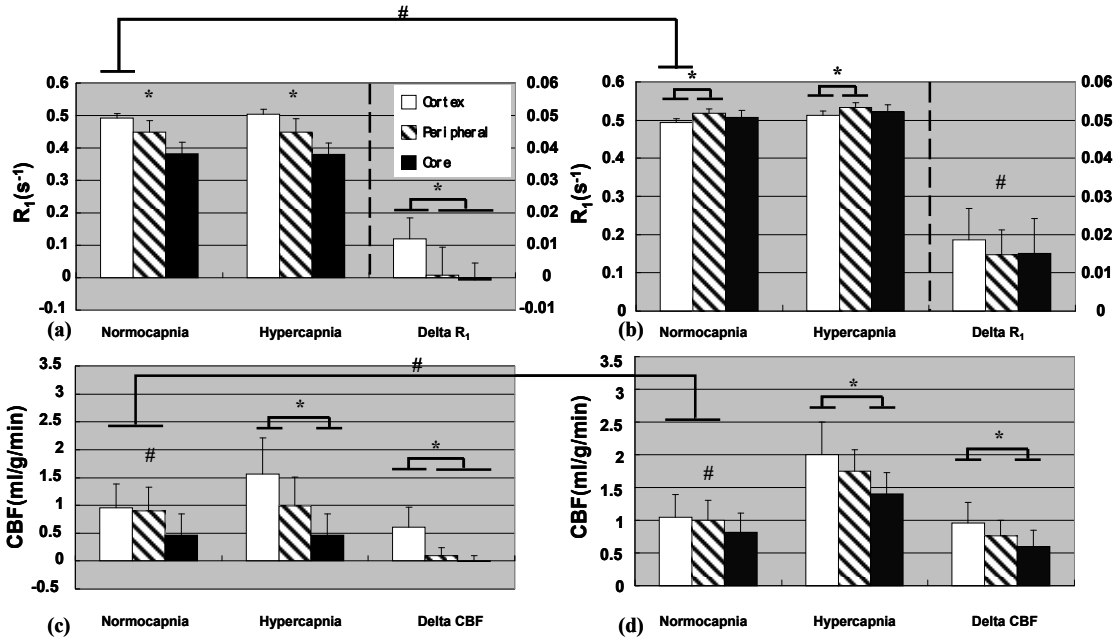

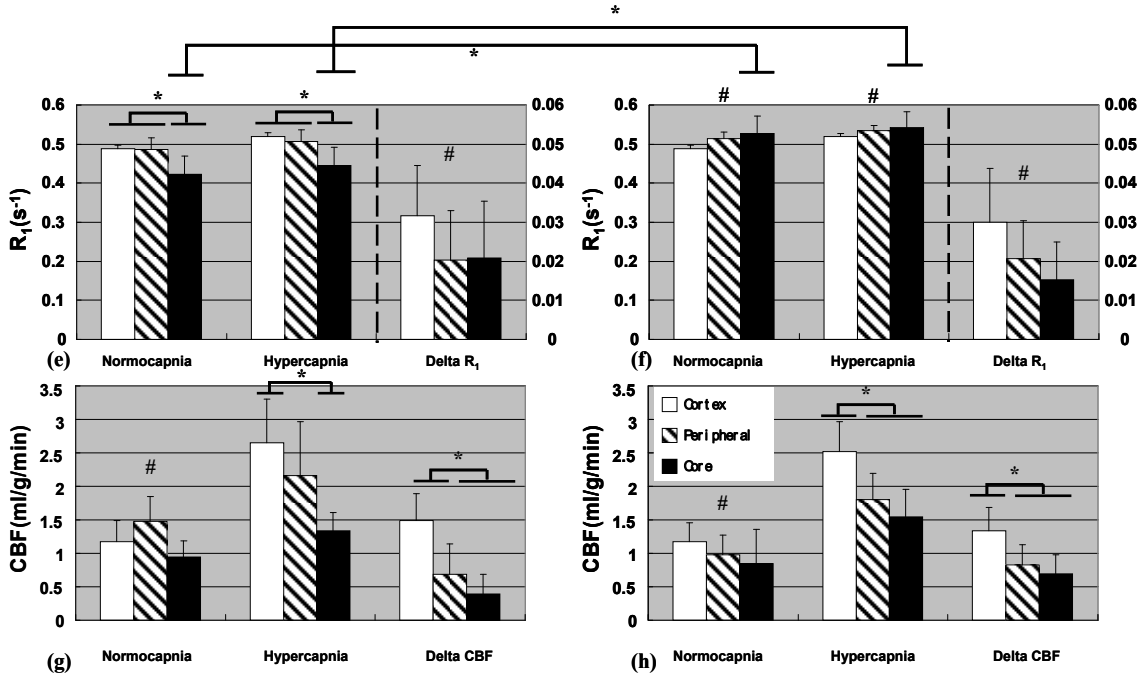

Figure 7.2 Mean and standard deviation of R_1, delta R_1 (a and b for day 1 while e and f for day 7), CBF and delta CBF (c and d for day 1 while g and h for day 7) at cortex, peripheral area and core lesion on both lesion side (a, c, e and g) and control side (b, d, f and h).
means P>0.05, no statistical difference * means p<0.05

Table 7.1 summarizes mean and standard deviation of the delta CBF induced by hypercapnia calculated with the SR-T_1 method and the CASL technique in the MCAO rat brain measured on day 1 (n=10) and day 7 (n=6) after 1 hour MCA occlusion. There is a good agreement between the delta CBF values measured with these two approaches in the different ROIs at both ipsilesional and contralateral side on day 1 and day 7 after the occlusion. Paired t-test is used to compare delta CBF values computed with these two methods and the p value ranges from 0.10 to 0.74.

Table 7.1 Summary of mean and standard deviation of the delta CBF change induced by mild hypercapnia calculated with the SR-T_1 method and the CASL technique at different ROIs in the MCAO rat brain

measured on day 1 (n=10) and day 7 (n=6) after 1 hour occlusion.

Time after the occlusion	ROI	Delta CBF (ml/g/min) (SR-R_1 Method)		Delta CBF (ml/g/min) (CASL Method)	
		lesion side	control side	lesion side	control side
Day 1	Cortex	**0.65± 0.35**	**1.00± 0.44**	**0.61± 0.36**	**0.96± 0.32**
	Peripheral	**0.04± 0.47**	**0.80± 0.35**	**0.09± 0.14**	**0.76± 0.24**
	Core	**0.00± 0.29**	**0.82± 0.49**	**0.00± 0.09**	**0.60± 0.25**
Day 7	Cortex	**1.71± 0.70**	**1.62± 0.75**	**1.48± 0.41**	**1.34± 0.34**
	Peripheral	**1.10± 0.68**	**1.12± 0.52**	**0.69± 0.46**	**0.83± 0.30**
	Core	**1.12± 0.79**	**0.82± 0.53**	**0.40± 0.30**	**0.70± 0.28**

Figure 7.3 shows the mean and standard deviation of ADC at cortex, peripheral area and core lesion at both the lesion side and the corresponding areas at the control side on day 1 (n=10) and day 7 (n=6) after 1 hour occlusion. There is a significant ADC decrease in the peripheral lesion area and core area at the lesion side when comparing it with the ADC in the homologous control side on day 1 after the occlusion. In contrast, ADC is significantly higher in the core area at the lesion side than that at the control side on day 7 post-occlusion.

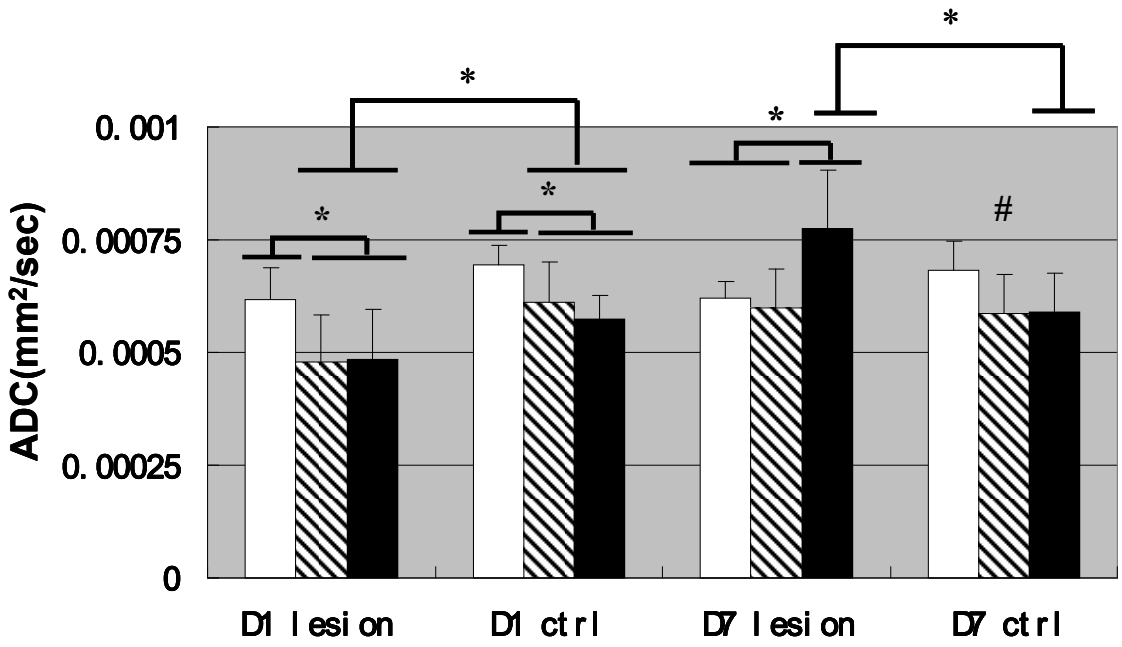

Figure 7.3 Summary of the mean and standard deviation of the ADC at cortex, peripheral area and core lesion at both the lesion side and control side on day 1 (D1, n=10) and day 7 (D7, n=6) after the 1 hour MCA occlusion.

7.4.3 CVR maps on day 1 and day 7 after the occlusion and H.E. histology images on day 7 post-occlusion of MCAO rat brain

Figure 7.4 shows the CVR images on day 1 and day 7 post-occlusion as well as the corresponding slices of H.E. histology images on day 7 of two representative rats. As we can see, the spatial pattern of the CVR images is comparable to the delta CBF images (Figure 7.1) generated with either the SR-T_1 method or the CASL technique. This is because the physical meaning of the ASL CBF based CVR images and delta CBF images basically are the same except that CVR images are further normalized by its baseline CBF under normocapnic condition as well as its end-tidal CO_2 concentration difference

between the hypercapnia and normocapnia conditions, therefore, the CVR images showing a better contrast than delta CBF images.

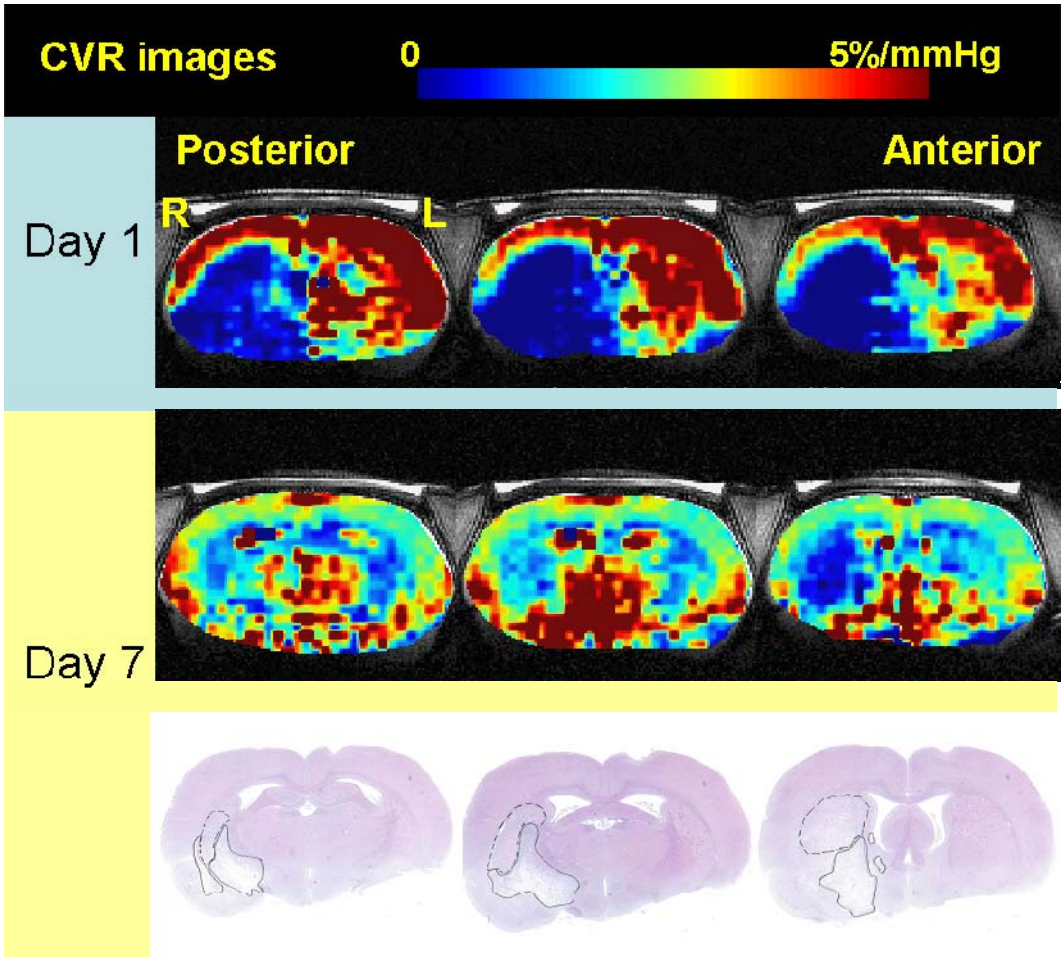

(a)

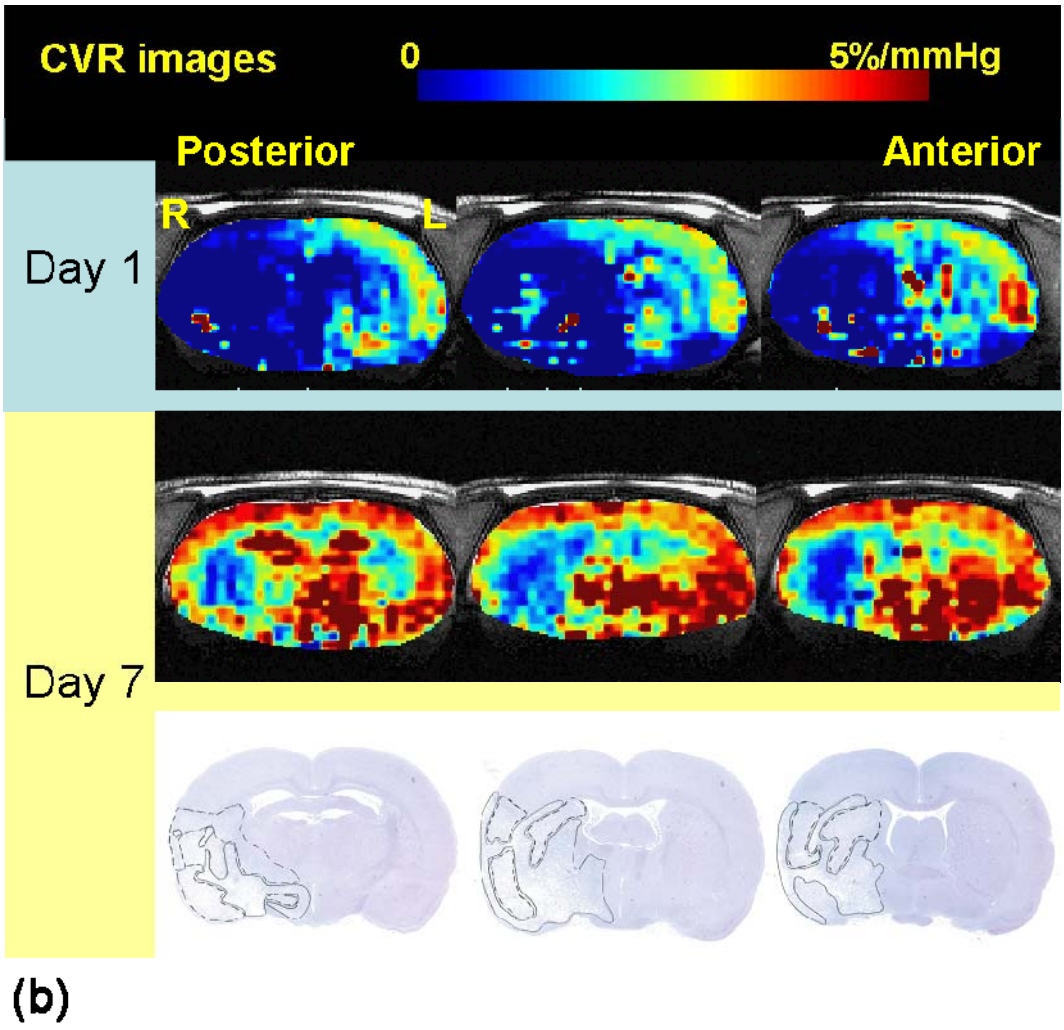

Figure 7.4 The ASL-CBF based CVR images on day 1 and day 7 post-occlusion as well as the corresponding slices of H.E. histology images on day 7 of two representative rats. The regions enclosed in the dash line indicate the partial neuron lesion brain tissue and the complete neuronal lesion brain tissue are enclosed in the solid dark line.

7.5 Discussion and Conclusion

7.5.1 Further validation of imaging CBF change with the SR-T_1 method

Imaging CBF change with the SR-T_1 method has been verified with the indirect laser Doppler flowmetry (LDF) of relative CBF measurement, direct CBF measurement using the CASL approach as well as at different magnet field strength (See Chapters 2-5) in normal or global lesion rat brains. The present study further demonstrates that the sensitivity and reliability of the SR-T_1 method for measuring CBF changes in preclinical MCAO rat brains.

First of all, there is an excellent agreement of CBF change induced by the mild hypercapnia measured with the SR-T_1 method and with the CASL technique in varied lesion regions at lesion side of the rat brain (Table 7.1), this is also true for the CBF change in the homologous ROIs at the control side. Paired t-test is used to compare the CBF change measured with the SR-T_1 method and with the CASL technique in a given ROI, no statistical difference was found between them and the p value ranges from 0.10 to 0.74. Moreover, the CBF change in varied lesion ROIs is distinct from the values in the corresponding ROIs at the control side, indicating the sensitivity of perfusion change computed with these two MRI methods. For example, the CBF increase measured with the SR-T_1 method and the CASL technique in the somatosensory cortex during hypercapnia at the lesion side is about 64% of that at the control side on day 1 after the occlusion. In contrast, there is almost no CBF change in the peripheral and core area at the lesion side when hypercapnia is induced on day 1 after the occlusion, suggesting the

impairment of the vascular response to CO_2 after the apparent MCA occlusion. However, on day 7 after the occlusion, the CBF increase in response to mild hypercapnia in the cortex of the lesion side shows 5-10% higher than that in the corresponding ROI at the control side. Besides, the vascular response in the peripheral area at the lesion side on 7 days increases significantly when compared with that on day 1 after the occlusion, which is supported by the fact that the delta CBF enhancement is comparable to the control side. This observation indicates the improved cerebrovascular reactivity as the gradual progression of the post-ischemic pathological evolution.

It is worth to point out that the absolute value of the delta CBF increase calculated with the SR-T_1 method appears larger than that computed with the CASL technique, we speculate several aspects might have caused this phenomenon. First, it could be due to the omission of temperature related T_1 or R_1 change (see supplementary materials) during the hypercapnia of the CBF increase calculation. The temperature increase during mild hypercapnia could lead to an exaggerated R_1 under hypercapnia condition, which results in the overestimated delta R_1 and therefore delta CBF. In addition, the weighting function of the influence of the enhanced exchange spin in the lesion area might be different for these two techniques at a chronic stage of post-ischemia associated with pathology evolution, which could also cause the discrepancies of the calculated delta CBF values. Third, it is also likely results from the underlying histopathological evolution, such as migration of macrophage cells to the lesion area, reactive gliosis and vascular proliferation [136, 137] on day 7 after the occlusion, all of these histopathological progression might have dramatically changed the properties of local tissue, for instance,

blood-tissue water partition coefficient λ. Therefore, the calculated delta CBF using the SR-T_1 method according to Equation 4.2 might have been overestimated. However, all these speculations need more thorough investigation in future. Nevertheless, the delta CBF measured with the SR-T_1 method and with the CASL technique does not reach the statistical significant difference ($p>0.05$) even at day 7 after the occlusion, which demonstrates that the SR-T_1 method is still valid and genuinely reflects the CBF change.

In addition, the spatial pattern and magnitude of the delta CBF images created with the SR-T_1 method is consistent with those generated with the CASL technique (Figure 7.1 and 7.2), although the former images appear less uniform in the deep brain region with the relatively poor EPI quality due to inhomogeneous B_0 and B_1 fields. In summary, the SR-T_1 method should be able to noninvasively and reliably image CBF change in an absolute scale induced by pathological conditions associated with cerebrovascular diseases.

7.5.2 Differentiate perfusion related R_1 and pathology based R_1 in MCAO rat brain

The apparent R_1 ($1/T_1$) value of both the lesion side and the control side we measured in the MCAO rat brain is consistent with that reported in a previous transient MCAO mice study at 9.4T [41] , although they did not evaluate it in the varied extent of injury area separately. The spatial pattern of R_1 images correlates well with the T_2-weighted images and ADC images on both day 1 and day 7 post-occlusion (see Figure 7.1). However, it shows disassociation when comparing the R_1 images with perfusion images. For instance, in the peripheral lesion area, the R_1 in the lesion side decreases to

86% (or 94%) of that in the homologous area at the control side on day 1 (or on day 7) of post-occlusion no matter CBF in this area is hyper-perfused or hypo-perfused. The R_1 in the core area of the lesion side is about 75% on day 1 (or 81% on day 7) post-occlusion of that in the corresponding region at the control side. In another word, the R_1 value decrease in the peripheral lesion area and core area due to the pathological alteration (including CBF deficit) induced by 1-hour transient ischemia accounts for 14% and 25% on day 1 (6% and 19% on day 7) post-occlusion of its inherent apparent R_1^{app}. This percentage is significantly higher than 4.7% obtained during acute 1-minute occlusion using four-vessel occlusion model (see Chapter 2), indicating dominant mechanisms other than the CBF deficit contribute to the change of tissue R_1 in the present study. If the CBF related R_1 effect is removed (essentially R_1^{int} instead of R_1^{app} in this case) in the current experiment, this percentage value solely attributed by pathological evolution other than CBF deficit would change to 14% and 24% on day 1 (8% and 20% on day 7) post-occlusion in the peripheral lesion area and the core area respectively. These results suggest that the R_1 decrease at a late stage (day 1 and day 7) after the occlusion is mainly dominated by the brain tissue property change instead of CBF deficit because the percentage changes of R_1^{int} and R_1^{app} are very close.

Conventional T_1-weighted images are generally considered less useful for detecting acute ischemic stroke due to their poor sensitivity. This is not surprising because the R_1 change is about 25% of its normal value even at the extreme case and this discrepancy will become less susceptible in the T_1/R_1 -weighted images. However, quantified T_1 (or R_1) images provide better contrast and several groups have reported

early (even within a few minutes after the occlusion) decrease of R_1 (i.e. increase of T_1) in focal cerebral ischemic models [39-42]. This early change of R_1 might be related to the CBF deficit [39], locally reduced dissolved O_2, a change of water environment [138, 139], early development of vasogenic edema and/or the increased water content even before the Blood-Brain Barrier (BBB) breaks down [41, 140, 141]. The data we show herein is on day 1 and day 7 after the transient ischemic attack, where the time window has been long enough to allow all the above mentioned mechanisms occur. Figures 7.1 and 7.4 show that on day 7 the lesion area in R_1 images coincides well with the final lesion area delineated by the pathologist, demonstrating a good correlation between the R_1 hypo-intensity and the tissue damage determined by histological damage. At some extent, R_1 image is more sensitive and specific than CBF image to determine the lesion of the tissue because the baseline CBF can be either increased or decreased depending on the severity of the lesion as well as stages of the ischemic progression etc. This can be partially demonstrated in Figure 7.2, no statistic difference is found among the CBF values of cortex, peripheral and core regions at the lesion side on both day 1 and day 7; in contrast, R_1 values among varied lesion regions are statistically different, revealing that the R_1 images are more sensitive to the extent of lesion and show more consistency than CBF images under normocapnia condition. How R_1 or T_1 is quantitatively related to the fate of the injured tissue needs further investigation. Nevertheless, quantified R_1 or T_1 images should be able to provide sensitive and reliable information and help early detection, vascular reactivity assessment and tissue damage determination caused by ischemic cerebrovascular disease.

7.5.3 Spatial and temporal characteristics of hyperperfusion and cerebrovascular reactivity

Some tissue property changes subsequent to pathological change during the stroke, for example, T_1 (or R_1), arterial transit time, more freely exchanged water due to the disrupted blood brain barrier (BBB) (increased permeability) could lead to the overestimation of CBF. However, the absolute CBF we calculate based on Eq.4.3 have already considered the T_1 change due to the occlusion by using the measured T_1 (or R_1) maps under different conditions (either normocapnia or hypercapnia). In terms of transit time, a 400ms post labeling delay was also incorporated into the CASL acquisition. Moreover, our observation of hyper-perfusion after the occlusion are consistent with other group's studies of performing the same duration of MCA occlusion and imaging in the similar time window [42, 142, 143]. The phenomenon of hyper-perfusion was also confirmed by carrying out the dynamic susceptibility contrast (DSC) technique by Nakamura and Shen et al. Therefore, hyper-perfusion we observed in the transient ischemic tissue is a generally existing fact, less likely to be artificial.

There are two types of hyper-perfusion observed in this study: one type (type 1) is not associated with any corresponding T_2-weighted and ADC image abnormality. It usually locates in the cortex of the lesion side and it is found in some MCAO rats (3 out of 10) on both day 1 and day 7 after 1 hour transient occlusion. Figure 7.1b and d (slightly higher CBF in the cortex at the lesion side than the homologous region of the control side, indicates by the red arrows) is such an example. Its CVR is vaguely compromised on day 1 but recovered on day 7 post-occlusion (Figure 7.4b). Moreover,

there is no actual tissue damage shown in its corresponding histology images (Figure 7.4b). This incidence is likely caused by the surgery procedure itself because the similar phenomenon is also seen in the sham surgery rats (data not shown). Most likely, it results from the temporary blood vessel dysfunction induced by the operation and then followed by an instantaneous reversal of blood circulation after withdrawal of the microwire.

Another type (type 2) of hyper-perfusion we have detected in this study is associated with the corresponding hyperintensity of T_2-weighted images, decreased R_1 and ADC images on day 1 post-occlusion, which usually is seen in the peripheral lesion area at the lesion side in 6 out of 10 rats on day 1 post-occlusion. Figure 7.1a shows such type of hyper-perfusion in one representative rat. This observation is in coincidence with Shen et al.'s previous study of 60-minute MCAO rats scanned at 24 hours after the occlusion[42]. However, we observed persistent hyper-perfusion of peripheral lesion area than the control side almost exclusively in all rats on day 7 post-occlusion (n=6), while they reported hyper-perfusion resolved by day 7 in most animals. The discrepancies might be due to the surgery procedure for animal model, local blood pressure during the surgery preparation, efficiency of recanalization as well as the severity of the ischemic attack. It is also interesting to point out that these hyper-perfused areas show normalized ADC on day 7 after the occlusion and partially neuron damage in the histology images. In contrast, core lesion area (mostly locates in the deep striatum of the rat brain in the present study) which shows decreased CBF and ADC on day1 and a reversed ADC value on day 7 of post-occlusion, indicating the disruption of cell membrane and the increased extracellular water content in these lesion area. Moreover, these areas also correlate well

with the complete neuron death area indicated in the histology image (Figure 7.1 and 7.4). The conventional diffusion-perfusion mismatch (normal ADC with CBF deficit) developed in the acute phase [144-146] was not evidently seen in our present studies, which more focused on the post-ischemic reperfusion stage.

Interestingly, the CVR induced by mild hypercapnia in these hyper-perfusion areas is significantly declined just as the core lesion areas compared to the homologous ROIs at the control side on day 1 and keep being compromised on day 7 of post-occlusion (see Figure 7.4) although it does show some degree of improvement than that on day 1. The final tissue damage areas shown in the histology images seem to correlate well with the day 7 CVR diminished region. More specifically, hyper-perfused area on day 7 of post-occlusion more localized in the partially neuron dead brain tissue (dash line enclosed area in Figure 7.4) and the hypo-perfused area is more confined in the completely neuron dead tissue region (solid line enclosed area in Figure 7.4). It has been reported that the maximally vasodilated non-necrotic tissue with compromised vascular responsive capacity showed an increased oxygen extraction fraction (OEF) and the vascular response capacity and OEF was negatively correlated [147]. The hyper-perfused peripheral area with compromised vascular capacity observed in the current study, therefore, might indicate the existence of some potentially living neuron. All the observation is consistent with the notion that late reperfusion usually related to some extent of damage [42, 148] although its final fate is not completely clear. The overall results also indicate that baseline CBF can be very complicated due to its dynamic

variation during the entire ischemic evolution but hyper-perfusion area generally seems to have a better outcome than persistent hypo-perfusion region.

The impaired vascular response regions displayed in day 1 CVR images show the largest lesion size than all the other image modalities, but the actual damaged areas (both solid and dash line enclosed areas) defined by the histology images obviously are much smaller than these regions (Figure 7.1 and 7.4). It implies and corroborates that the process of vascular response toward the ischemic attack is very rapid and the involved impaired hemodynamic area or volume is much more extensive than the actual neuronal lesion area. At a relative earlier stage of post-ischemic reperfusion, for example, 24 hours of the post-occlusion, the lesion size of the decreased ADC area appears to be minimal and spatially correlates well with the final lesion areas in histology images, while the size of abnormal area of R_1 and CBF images is in between. Therefore, when combining ADC and CVR images, three different regions subsequent to the ischemic attack can be identified: impaired vascular reactivity region determined by the compromised CVR; true neuronal lesion region defined by the decreased ADC and the mismatch region defined by the compromised CVR but with normal ADC value represents the potentially viable and intact neuron region. The third region (mismatch region) shows recovered ADC, CVR values and intact histology on day 7 even without any treatment intervention in this experiment. It would be of great importance and very interesting to further explore whether these mismatched regions could serve as the prospective treatment target and accelerate the associated pathological progression and improve the clinical symptoms.

7.5.4 Clinical relevance, limitations of the study and future prospects

According to Centers for Disease Control and Prevention (CDC), Stroke is a leading cause of death (killing nearly 130,000 Americans each year) and long-term disability in the United States [149, 150]. Of all strokes, 87% are ischemic in nature and 10% are intracerebral hemorrhagic strokes. [150]. Clinically, if the onset of stroke symptoms is within 3-4.5 hour and the hemorrhage as well as absolute contradictions of anticoagulation has been ruled out, thrombolytic treatment will be applied. On the one hand, recanalization of occluded cerebral vessels early enough can help to restore the function of salvageable tissues, on the other hand, reperfusion may also lead to the production of free radicals and toxins, increase microvasular permeability, aggravate edema, increase the risk of hemorrhage and secondary cell death [151-153]. Therefore, noninvasive, reliable and serial imaging methods or protocols are valuable of not only monitoring the progression of the ischemic injury and understanding the underlying pathophysiology evolution, but also determining stage of post-ischemia and even correspondingly adjust the treatment plan.

The present study focuses on the post-ischemic reperfusion injury since different imaging modalities were acquired only on day 1 and day 7 after the occlusion. It demonstrates that R_1 and delta R_1 images are useful (Figures 7.1 and 7.4) for determining the lesion area and CBF changes induced by vasoactive challanges, it should have no major hurdle to implement in clinical studies with reasonable temporal and spatial resolution within the limited and precious workup time. It is well known that the underlying mechanisms of change of T_2, T_1 and ADC in MR images are severe

pathophysiological events such as vasogenic edema, increased water content, BBB leakage after the depleted the energy. Since the areas with hyper-perfusion (type 2) observed in this study correlate well with hyper-intensity of T_2-weighted images, decreased R_1 and ADC images on day 1 of post-occlusion, it implies that certain extent of brain tissue damage caused by the MCA occlusion in these areas. Nevertheless, there might be some lived neurons left because the corresponding areas in the histology images show partially neuron damage instead of complete neuron death. Therefore, it would be very exciting and important to further investigate whether these partially neuron damaged area could be the potential treatment target in response to proper intervention at this stage.

Unfortunately, there is no data of earlier time point after the occlusion, which could have made the information of the post-ischemic evolution more complete. Second, more delicate and dedicated histopathology could have correlated with a variety of imaging modalities and served a better assessment of the fate of the damaged tissue. For example, what does the partially dead region enclosed in the dash line in Figure 7.4 exactly mean? Could it possibly be saved when given the appropriate intervention? Or has it been on the path of being perished already and not salvageable at all? Does the hyper-perfusion seen in this model represent the vascular regeneration or simply dilation of the injured vessel due to the loss of its autoregulation? Third, more objective imaging analysis techniques are desired to improve the qualitative and quantitative investigation.

Metabolic imaging, for example, cerebral metabolic rate of oxygen ($CMRO_2$) imaging [154] [16, 155], ^{31}P magnetic resonance spectroscopy (MRS) combined with magnetization transfer (MT) [156] are able to noninvasively reveal the status of oxidative

metabolism and adenosine triphosphate (ATP) metabolic rate of the MCAO brain lesion tissue, which is better to correlate the severity of damage and the viability of the tissue than CBF images [154, 157]. When combined with conventional perfusion and diffusion images, it also provides a useful and powerful way to understand the underlying histopathological evolution. This is extremely important for longitudinal study of reperfusion on the development of infarctions and the evaluation of the efficacy of the treatment.

In conclusion, this study demonstrates that the SR-T_1 method is able to noninvasively and reliably measure the CBF change under pathological conditions, such as MCAO in rat brain. Therefore, it offers a sensitive, noninvasive and dynamic neuroimaging tool to assess CBF change as well as other important information under both physiological and pathological conditions. The R_1 image is a valuable image modality to detect early lesion, assess vascular reactivity and determine tissue damage caused by ischemic cerebrovascular disease. Post-ischemic absolute CBF can be either increased or decreased, depending on the time of scanning, severity of the lesion and efficiency of recanalization etc. Area with hyper-perfusion showing decreased vascular capacity seems to have a less extent of lesion than persistent hypo-perfusion region, but its final outcome is not completely clear. Compromised CVR area at the late stage (day 7 after the occlusion) correlates well with the lesion area in the histology image. Combination of varieties of MRI and MRS modalities could provide a useful and powerful way to investigate, understand the underlying mechanisms and monitor the efficacy of treatment for the cerebrovascular diseases.

CHAPTER 8 Conclusions and Future Prospects

In this chapter, major conclusions drawn from this thesis are summarized and some consideration of further technical investigation as well as future prospects of the application of the SR-T_1 MRI method are proposed and discussed.

8.1 Major Conclusions

CBF increase (or decrease) through rapidly spin exchange between blood water and brain tissue links to the acceleration (deceleration) of the cerebral tissue relaxation rate serves as the fundamental mechanism of the SR-T_1 MRI method of imaging CBF change. Associated with global (defined as the region covered by the RF coil in this thesis) saturation recovery combined with EPI sampling, the two-phase arterial spin model was described and validated with physiological (mild hypercapnia) and pathological (four-vessel occlusion) CBF change in rat brain at 9.4T. The estimated cortical rat brain baseline CBF using simultaneous LDF measurement and the SR-T_1 MRI method was consistent with the literature report under the similar anesthetic conditions. Moreover, close related but distinct BOLD dynamic change can be concurrently monitored in addition to the CBF change using the SR-T_1 method (Chapter 2).

Two confounding factors, the large vessel inflow effect and arterial transit time to the SR-T_1 method for imaging CBF change were investigated in Chapter 3. It demonstrated that there was no significant contamination of these two factors to the T_1 measurement and subsequent CBF change quantification with the SR-T_1 method.

The SR-T_1 method was further validated by directly comparing CBF change measured with MRI CASL technique in Chapter 4. It revealed that the CBF change measured with the SR-T_1 method was comparable with it calculated with the CASL technique. In addition to CBF change, the SR-T_1 method was also able to obtain absolute CBF as well once intrinsic relaxation time (T_1^{int}) is known.

Chapter 5 revealed that CBF increase induced by mild hypercapnia in rat brain was directly compared at two different magnetic fields: 9.4T and 16.4T. It proved the notion that CBF change (which calculated from the tissue T_1 at a given magnetic field) should be magnetic field independent although paradoxically T_1 itself is field dependent. Meanwhile, it also provided another piece of evidence of the validity of the SR-T_1 method for quantifying CBF changes.

The SR-T_1 method was carried out to quantitatively investigate the perfusion contribution to the total fMRI signal using a rat model with mild hypercapnia at 9.4T and human subjects with visual stimulation at 4T. It concluded that appropriately choosing the MRI parameters (short TR and large radiofrequency pulse flip angle) could help to achieve an improved fMRI contrast-to-noise ratio and spatial specificity for mapping brain activity and physiology changes (Chapter 6).

Finally, in Chapter 7, the SR-T_1 method was successfully applied to the rat MCAO model on day 1 and day 7 of post-ischemia and compared the CBF change with that calculated using the CASL technique in varied lesion regions of rat brain. It showed a good agreement of CBF change measured with these two techniques. The overall results demonstrated that the SR-T_1 method was able to noninvasively and reliably

measure the cerebral CBF change under pathological conditions. Additionally, the R_1 image provided a valuable image modality for early lesion detection, CBF change reactivity assessment and tissue damage determination caused by ischemic cerebrovascular disease. Various MRI modalities, associated with MRS and histological studies are very important to investigate and understand the mechanisms of reperfusion damage to the post-ischemic brain lesion as well as to evaluate the efficacy of the potential treatment.

In conclusion, the advantages of the SR-T_1 method are: i) simple setup and acquisition with one surface coil while does not need paired images; ii) imaging the parametric T_1/R_1 image, CBF change image and BOLD simultaneously; iii) reasonable temporal resolution, which is about 12 seconds. The disadvantages of the SR-T_1 method are: i) baseline CBF calculation is more challenging under pathological situations; ii) sensitive to B_0 and/or B_1 inhomogeneity with EPI sampling.

The technical comparison of pulsed arterial spin labeling (PASL), continuous arterial spin labeling (CASL) and the SR-T_1 method is summarized in table 8.1.

Table 8.1 The technical comparison of PASL, CASL and the SR-T_1 method.

	PASL	CASL	SR-T_1 Method
Paired Images	Y	Y	N
Parametric Images	N	N	Y
Baseline CBF	Y	Y	Feasible
Contamination Factors	Imperfection of tagging slab profile; artery transit delay; large vessel inflow effect	MT effect; artery transit delay; labeling efficiency as well as labeling magnetization decay	Imperfection of saturation boundary
Easiness of setup	Y	May need two separate coils	Y

8.2 Future Prospects

8.2.1 Technical consideration

The mechanisms of the SR-T_1 method could be further tested by saturation of the whole body using a volume coil. The T_1 measured by this way should be the intrinsic T_1 (T_1^{int}) instead of the apparent T_1 (T_1^{app}) and no change of T_1^{int} is expected even though CBF changes in response to the different physiological or pathological conditions. The baseline CBF could be calculated based on two measurements according to Eq. 4.1, one with whole body saturation the other with thin slab saturation. If T_1 changes measured with the whole body saturation when CBF is changed, mechanisms other than spin labeling need to be considered.

One interesting finding in MCAO rat brain on day 7 of post-occlusion is that the CBF change measured with the SR-T_1 method appears higher than that calculated with CASL technique (see Chapter 7). Several possibilities might have contributed to this observation. One is the temperature induced T_1 change during mild hypercapnia was not corrected (see supplementary materials), which could exaggerate the R_1 value during hypercania and therefore the subsequent CBF change. We could monitor temperature change by using a temperature probe to find out whether the temperature related R_1 change have caused the observed overestimation of CBF change with the SR-T_1 method. Another possibility could be the different weighting function for the influence of the enhanced exchange spin in the lesion area to the SR-T_1 method and the CASL technique at a late stage of the post-ischemic situation associated with the pathological evolution. Further investigation is needed to demonstrate this hypothesis.

The blood transit time (t_{tran}) in the brain is a very important physiology and/or pathology related parameter, which may potentially reflect the status of hemodynamic impairment in the cerebrovascular disease like ischemia and stroke. Usually it is inversely related to CBF. Another interesting project would be to estimate t_{tran} using the two-phase artery spin model derived in Chapter 2.

8.2.2 Future application and prospects

Cerebral Vascular Reactivity (CVR) could be evaluated using R_1 measured with the SR-T_1 method developed in this thesis with nomocapnia and hypercapnia experiments. Its quantification could employ the following equation:

$$CVR_{R_1} = \frac{100}{R_{1-normo}} \cdot \frac{R_{1-hyper} - R_{1-normo}}{PetCO_{2\text{-}hyper} - PetCO_{2\text{-}normo}} \quad (8.1)$$

where $R_{1\text{-hyper}}$ and $R_{1\text{-normo}}$ are the R_1 under hypercapnia and normocapnia conditions respectively, $PetCO_{2\text{-hyper}}$ and $PetCO_{2\text{-normo}}$ are the end-tidal CO_2 concentrations under hypercapnia and normocapnia conditions.

Figure 8.1 show the CVR images created with the SR-T_1 method and the ASL method in two of representative MCAO rats on day 1 after 1 hour occlusion as in Chapter 7 Figure 1. Similar response pattern is observed in CVR images created with these two techniques although their absolute scales are different, indicating the validity of the CVR assessment using the SR-T_1 method. The advantages of the SR-T_1 method are easy setup and acquisition with one surface coil, does not need paired images, simultaneous BOLD monitoring and reasonable temporal resolution.

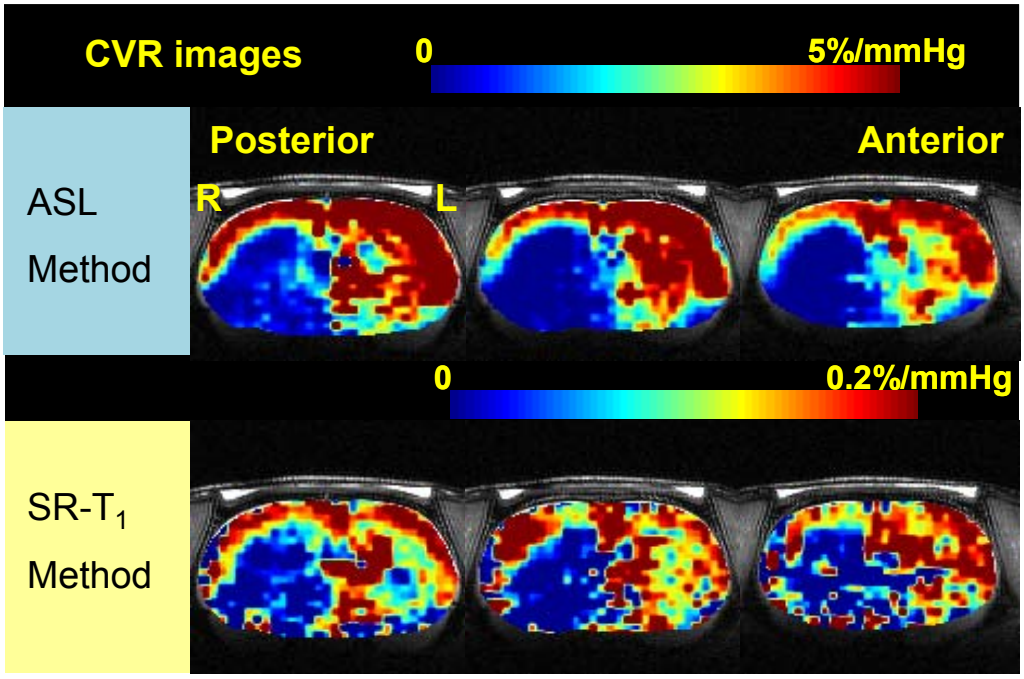

(a)

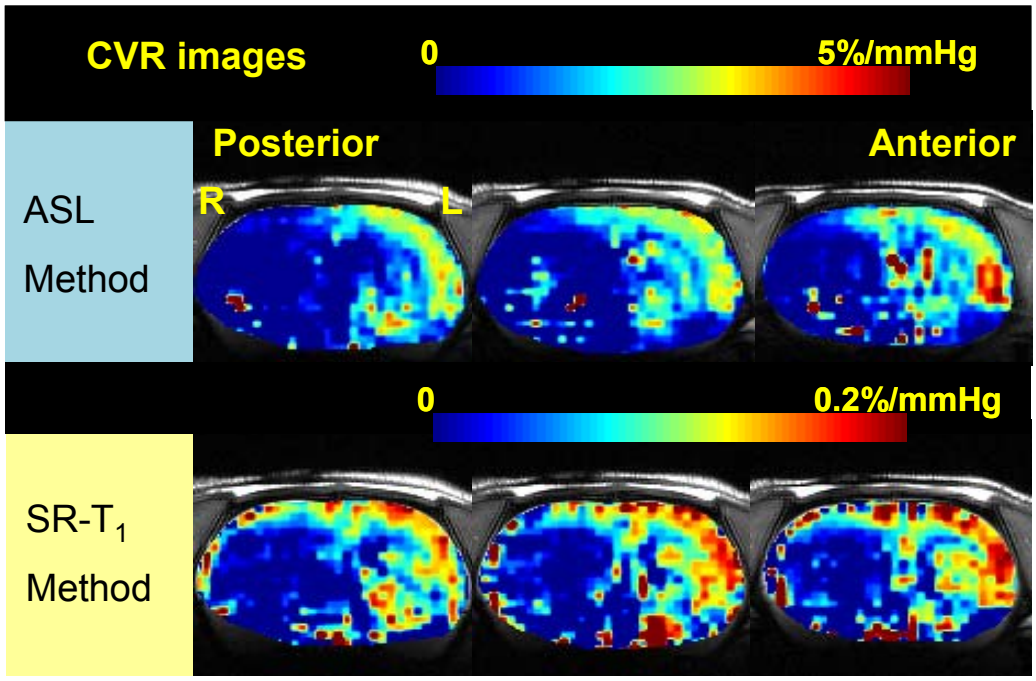

(b)

Figure 8.1 Three continuous slices of CVR images created with the SR-R_1 method and the ASL method in two representative MCAO rats on day 1 after 1 hour occlusion.

The SR-T_1 method potentially could also be applied to other diseases, for instance, traumatic brain injury (TBI). TBI is a serious and devastating public health problem in the United States. There are about 1.7 million incidences each year, which is one of the leading causes of death and permanent disability [158]. MRI imaging may play an important role in early detection, acute management and chronic surveillance of TBI [159-161]. Figure 8.2 shows three continuous slices of T_2-weighted images, R_1 images under both normocapnia and hypercapnia conditions as well as delta R_1 images between these two conditions scanned 3 hours after the right side blast incident in a representative rat brain. The R_1s of cortex (47 pixels of three slices) and subcortex (114 pixels of three

slices) at the lesion side are 0.464±0.014 s^{-1} and 0.472±0.014 s^{-1} respectively; showing significant smaller ($p<0.01$) than those values (the same number of pixels and ROIs in cortex and subcortex as the lesion side) at the control side, which are 0.477±0.015 s^{-1} and 0.484±0.012 s^{-1}. Moreover, the delta R_1s in response to hypercapnia in the cortex (0.011±0.006s^{-1}) and subcortex (0.011±0.006 s^{-1}) are also statistically smaller ($p<0.01$) than them in the control side (0.023±0.004s^{-1} in the cortex and 0.019±0.004s^{-1} in the subcortex). The small but significant decreased R_1 and delta R_1 is observed in the right (lesion side) cortex and subcortex compared to the left (control side) side even though there is no obvious lesion could be observed in T_2-weighted images, indicating tissue property change and reduced cerebral vascular reactivity. This is very preliminary data and more studies need to be done to test the sensitivity, reliability and understand the underlying mechanisms.

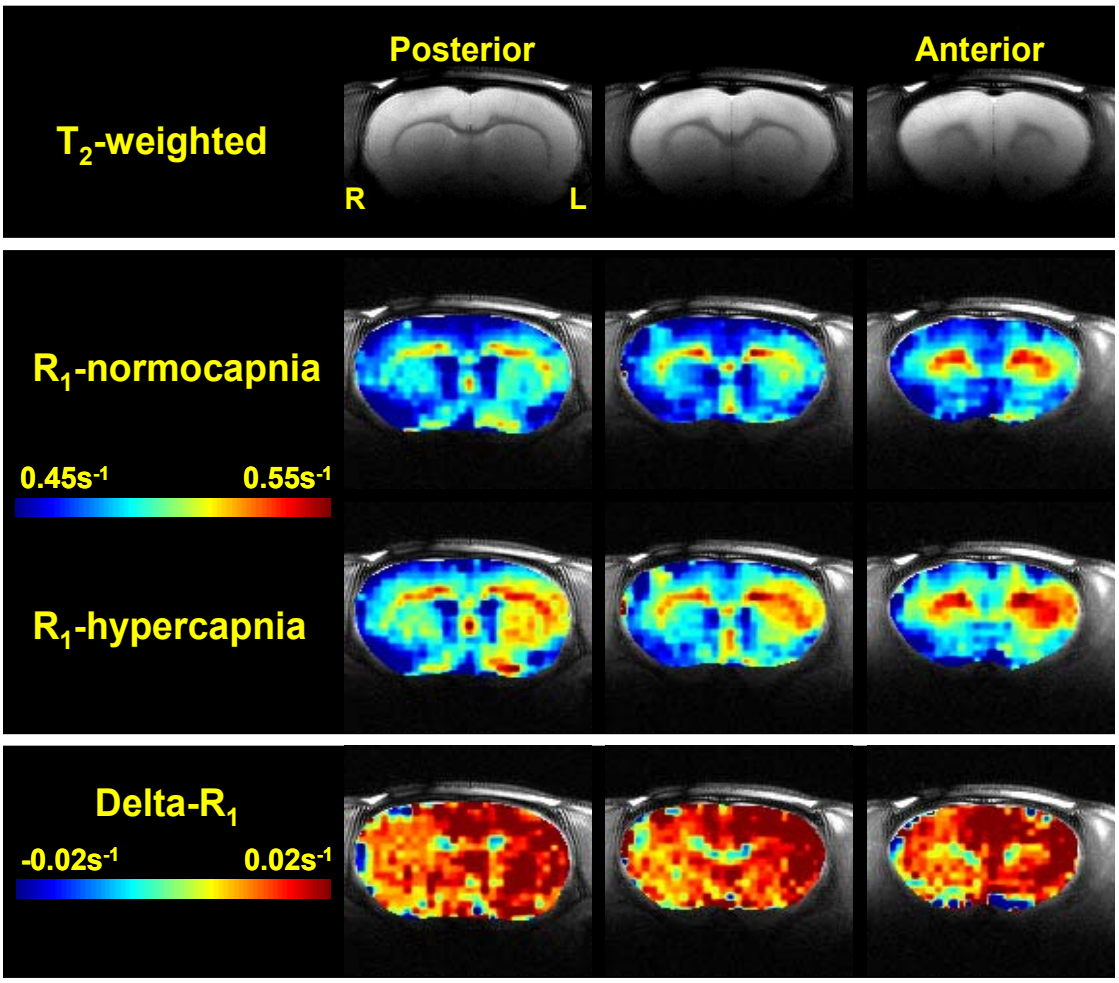

Figure 8.2 Three continuous slices of the T_2-weighted images, R_1 images under both normocapnia and hypercapnia conditions as well as the delta R_1 images between them scanned at 3 hours after the right side TBI incident in a representative rat brain. The R_1 and delta R_1 decreases in the right cortex and subcortex compared to the left side.

Finally, the SR-T_1 method could also be applied in human to image CBF change in response to functional brain stimulation [162] and varieties of diseases although it will be more challenging than the animal model due to its low baseline CBF, large size of head and long artery transit time. Nevertheless, the SR-T_1 method should enable an

alternative, noninvasive and useful neuroimaging tool to investigate CBF, CBF change and BOLD under physiological and pathological conditions.

SUPPLEMENTARY MATERIALS

Confounding effect of brain temperature change on T_1^{app} measurement

It is known that the longitudinal relaxation time (rate) T_1^{app} (R_1^{app}) is sensitive to temperature change [53-56]. The transient hypercapnia or ischemia perturbation can induce a change not only in CBF but also in the brain temperature because of the temperature difference between the cardiac and brain bloods [163]; both of these changes can attribute to the measured value of ΔR_1^{app} (see Eq. 2.15).

The baseline CBF in rat brain under normocapnia is 1.29ml/g/min from the Table 2.2 and blood tissue partition coefficient λ is 0.9ml/g, thus, CBF/λ=0.024s^{-1}. The R_1^{app} value of rat brain is 0.48 s^{-1} from our study, the relative CBF contribution to the R_1^{app} value can be estimated by 0.024 s^{-1}/0.48 s^{-1} = 5% and it only counts for several percent. It is critical to find out how much R_1 change is contributed from a temperature change during the CBF perturbation with saturation-recovery (SR)-T_1 MRI measurement and how it affects the quantification of CBF change.

The quantitative relation between T_1^{app} and temperature (T) can be described by:

$$T_1^{temp} = T_1^{'}(\infty)e^{-\frac{E_a}{\kappa T}} \tag{S.1}$$

where T_1^{temp} is the temperature-dependent longitudinal relaxation time; $T_1^{'}$ is the T_1^{temp} value when T=∞; E_a is the activation energy related to the T_1 relaxation process, κ is the Boltzmann constant. It has been demonstrated that under normal physiological conditions

there is an approximated relationship given by [53]:

$$T_{1,PC}^{temp} - T_{1,RC}^{temp} = m \cdot (T_{PC} - T_{RC}) \quad \text{(S.2)}$$

or

$$\Delta T_1^{temp} = m \cdot \Delta T \quad \text{(S.3)}$$

where the subscript "PC" and "RC" stands for Perturbation Condition and Reference Condition respectively; m is the tissue-specific T_1^{temp} dependence coefficient on the brain temperature. Within a small range of brain temperature change induced by physiological or pathological perturbation, Supplementary Eq. (S.3) can be further simplified as:

$$\Delta R_1^{temp} \cong m' \cdot \Delta T \quad \text{(S.4)}$$

where m' stands for a tissue-specific R_1^{temp} dependence coefficient on the brain temperature change. This relationship and m' can be determined through the regression of varied ΔT and ΔR_1^{temp} values measured in the absence of perfusion (e.g., complete cardiac arrest with CBF=0). Consequently, the constant m' can be used to determine ΔR_1^{temp} during and after physiological/pathological perturbation if the brain temperature change caused by the perturbation can be measured. ΔR_1^{temp} can be applied for further correction in order to precisely quantify ΔCBF by the SR-T_1 MRI method.

Supplement Results

Animal physiology

Physiological data of the experiment measured before the induction of perturbation and before KCl injection are summarized in Supplementary Table S.1. No significant changes

in pCO_2, pO_2 and heart rate were observed. There was, however, a statistically significant decrease in pH and mean arterial blood pressure (MABP) between these two measurements.

Supp Table S.1 Physiological data obtained prior to hypercapnia and before KCl injection (mean ± SE; n = 12) *significantly different from the value measured prior to hypercapnia; $p<0.05$.

	pCO_2(mmHg)	pO_2(mmHg)	PH	MABP (mmHg)	Heart rate (beat/min)
Prior to hypercapnia	31.2 ± 1.7	147.9 ± 7.2	7.497 ± 0.011	97.9 ± 3.6	367.8 ± 8.0
Prior to KCl injection	32.6 ± 1.5	171.6± 12.2	7.385 ± 0.023*	80.5 ± 6.2*	367.3 ± 14.5

Temperature changes in rat brain during the perturbations and determination of tissue-specific T_1^{temp} (m) or R_1^{temp}(m')

The maximal change of brain temperature increased 0.93±0.09ºC (n=3) during the transient hypercapnia perturbation; and decreased 0.26±0.02ºC (n=5) during the acute ischemia perturbation compared with the control condition before the induction of any perturbation. Supplementary Figure S.1 (a) and (b) show the averaged changes of brain temperature induced by the hypercapnia and ischemia perturbation, respectively, measured during (Stage 2 or **S2**), and after the perturbation (Stages 3 to 5 or **S3**, **S4** and **S5**; as measured approximately 4.8, 10.5 and 14.5 minutes after the termination of hypercapnia; and 2.0, 3.6 and 4.9 minutes after the termination of ischemia, respectively) compared to the control condition (Stage 1 or **S1**). The averaging time of measuring the temperature for S2, S3, S4 and S5 were 2.5, 6.5, 4.6 and 3.2 minutes for the hypercapnia

study; 1.0, 1.8 1.4 and 1.2 minutes for the ischemia study. The brain temperature increased significantly during all the post-perturbation stages as well as during the hypercapnia perturbation. In contrast, it dropped during the ischemia perturbation owing to the reduction of blood supply. These brain temperature changes led to the variation in R_1 (i.e., ΔR_1^{temp}), which can be determined according to Supplementary Eq. (S.4) if the constant of m' can be determined.

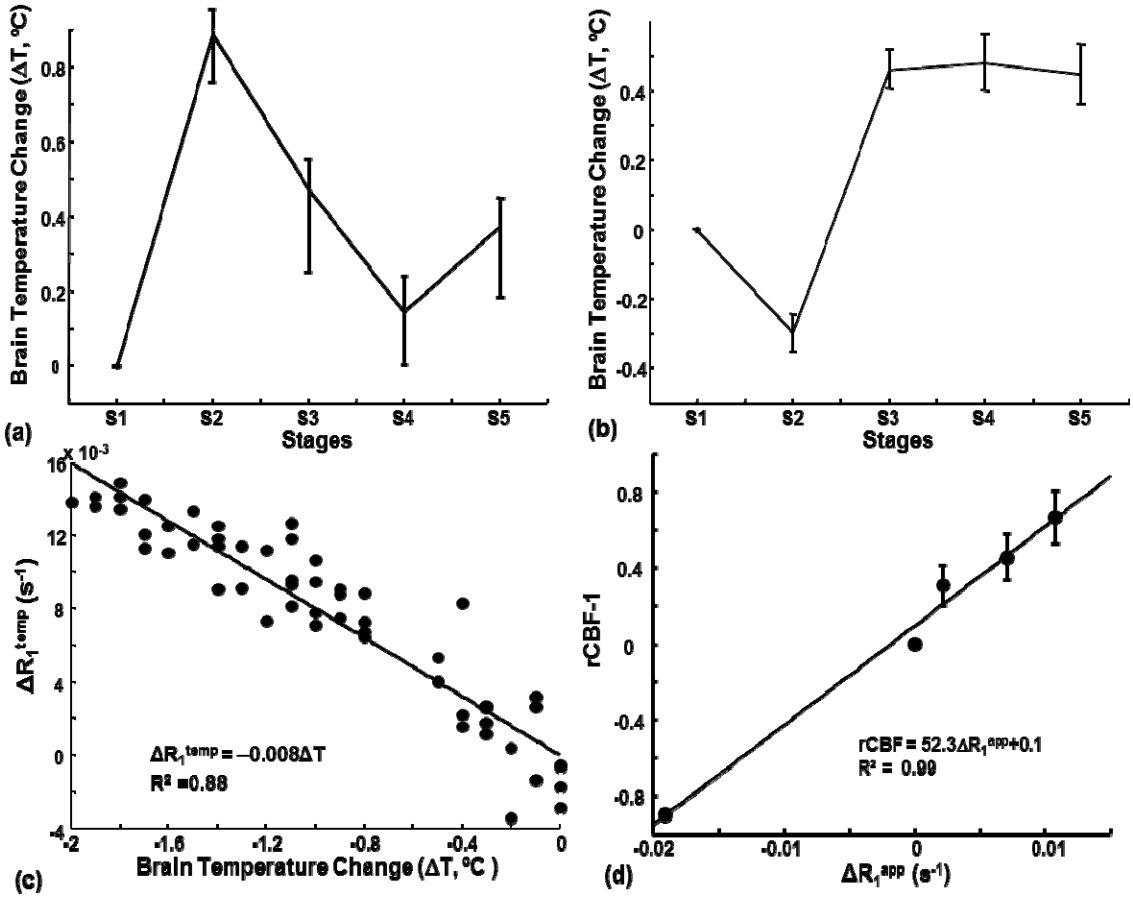

Supp Figure S.1 (a) and (b) Averaged brain temperature changes and standard error bars measured during (Stage 2: S2) and after (Stages 3, 4 and 5: S3, S4 and S5) the induction of (a) 7-minute hypercapnia (n=3) and (b) one-minute ischemia (n=5) perturbation. (c) The inverse correlation between the temperature dependent R_1 change (ΔR_1^{temp}) and brain temperature change (ΔT) measured after the KCl injection (i.e.,

CBF=0) from a representative rat. (d) Correlation between the averaged ΔR_1^{app} measured by the saturation-recovery-T_1 MRI method versus (rCBF-1). The vertical bars indicate the standard error of the mean (SEM) (n=5).

The temperature dependence coefficient, m defined in Supplementary Eq. (3) or m' defined in Supplementary Eq. (S.4), was measured in this study via quantifying the relationship between ΔR_1^{temp} and its corresponding brain temperature change (ΔT) during the cardiac arrest induced by potassium chloride (KCl) bolus injection, in which ΔR_1^{temp} was solely determined by ΔT. Supplementary Figure S.1c illustrates one measurement result from a representative rat and the linear regression for calculating m'.

The averaged m was 36.1±8.7 (ms/ºC) and m' was -0.007±0.002 (s^{-1}/ºC) (averaged R^2 = 0.6±0.15; n=5). The ΔR_1^{temp} values were calculated using the m' constant and the four ΔT values measured during Stages 2 to 5 as illustrated in Supplementary Figures. S.1a and S.1b, ultimately, they were used to calculate ΔR_1^{CBF} and ΔCBF according to Eq. (2.16) in the main chapter 2. The results indicate that the ΔT_1^{temp} in the rat cortex could count for 15.3%, 3.2% and 19.9% of the contribution to the total ΔT_1^{app} measured under the hypercapnia, ischemia and the first post-perturbation stage (i.e., Stage 3 or **S3**) after the ischemia perturbation, respectively.

Confound effect of brain temperature change on T_1^{app} measurement

Supplementary Figure S.2 depicts the high-temporal resolution (~12 s per data point without the averaging of repeatedly measured GE-EPI data) time courses of relative R_1 (rR_1 defined by $R_{1,PC}/R_{1,RC}$) measurements before the temperature correction (rR_1^{app})

and after the temperature correction (rR_1^{CBF}), showing a difference between them for both (a) hypercapnia and (b) ischemia studies. Therefore, the confound effect of brain temperature change was corrected in this study though it was small.

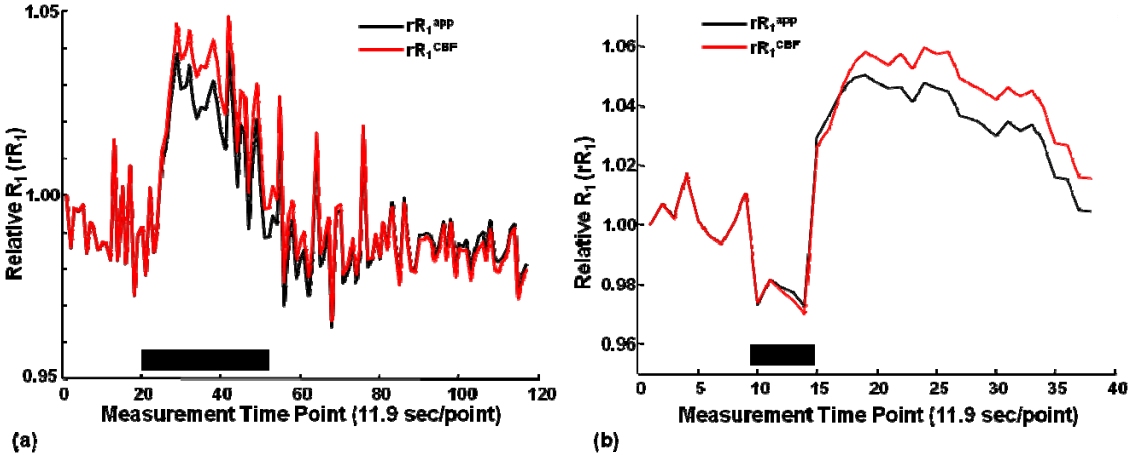

Supp Figure S.2 Time courses of relative R_1^{app} (rR_1^{app}; black lines) and R_1^{CBF} (rR_1^{CBF}; red lines) measured by the saturation recovery-T_1 MRI method before, during and after (a) hypercapnia and (b) ischemia perturbation from a representative rat (data extracted from a region of interest). The black bar indicates the duration of (a) hypercapnia (7 minutes) and (b) ischemia (one minute).

Supplementary Figure S.3 summarizes the averaged results as measured during different stages. In this figure, the time course of rCBF measured by LDF serves as a reference that was used to compare its temporal tendency and correlation with the SR-T_1 MRI results of rR_1^{app} and rR_1^{CBF} measured under the transient hypercapnia (Supplementary Figure. S.3a) and acute ischemia (Supplementary Figure. S.3b) perturbation. It is clearly evident that rCBF has a better temporal correlation with rR_1^{CBF} after temperature correction than rR_1^{app} across all post-perturbation stages. This is supported by the results of correlation coefficient (CC) analysis as summarized in Supplementary Table S.2. A slightly higher CC value was observed for the rR_1^{CBF}-rCBF

time course correlation for all individual measurements compared to the rR_1^{app}-rCBF time course correlation, nevertheless the averaged CC values between the two comparisons did not reach statistical significance. These results indicate that correcting the effect of brain temperature change on the apparent T_1^{app} rate can improve the correlation between the rCBF and rR_1^{CBF} measurements. On the other hand, they also suggest that both rR_1^{app} and rR_1^{CBF} have a good correlation with rCBF and can directly reflect the CBF change in response to perturbations, though rR_1^{CBF} is more accurate than rR_1^{app}. This is not surprising owing to the fact that CBF dominates the change of T_1^{app} or R_1^{app}; and temperature effect on T_1^{app} or R_1^{app} only accounts for less than 20% of ΔT_1^{app} even the perturbations applied in this study resulted in substantially large brain temperature changes.

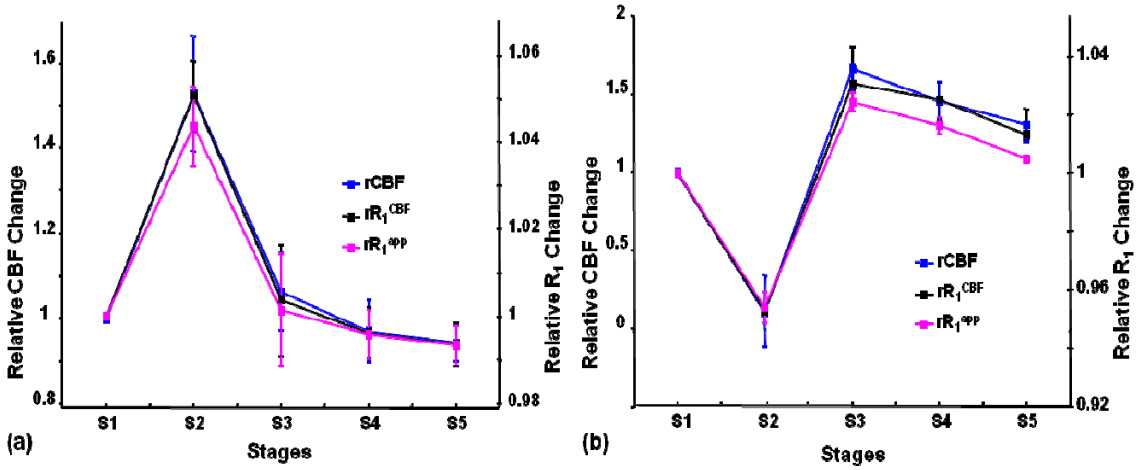

Supp Figure S.3 Comparison of temporal responses of rR_1^{app}, rR_1^{CBF} based on ROI analysis results and rCBF measured under (a) 7-minute hypercapnia (n=3), (b) the one-minute ischemia (n=5) perturbation condition, respectively. The first data point on the left side represents the control stage (S1) and serves as a reference for normalization of other data points. The second data point stands for the averaged results measured under (a) hypercapnia or (b) ischemia perturbation (i.e., Stage 2 or S2). The third, fourth and fifth data points present the measurement results during three post-perturbation stages (S3, S4 and S5). The

vertical lines indicate the standard error of the mean (SEM).

Supp Table S.2 Temporal correlation coefficient (CC) between rCBF and rR_1^{CBF} measurements ($CC_{rR1CBF,rCBF}$) as well as CC between the rCBF and rR_1^{app} measurements ($CC_{rR1app,rCBF}$) under hypercapnia and ischemia conditions based on the data analysis of region of interest located in the surface cortical region.

	Ischemia (n=5)		Hypercapnia (n=3)	
No.	$CC_{rR_1^{CBF},rCBF}$	$CC_{rR_1^{app},rCBF}$	$CC_{rR_1^{CBF},rCBF}$	$CC_{rR_1^{app},rCBF}$
1	0.960	0.929	0.970	0.963
2	0.983	0.968	0.985	0.974
3	0.964	0.962	0.996	0.995
4	0.946	0.937		
5	0.992	0.991		
Mean ± SE	0.969 ± 0.008	0.958 ± 0.011	0.984 ± 0.008	0.977 ± 0.010
Paired t-test	p = 0.10		p = 0.17	

Supplemental Discussion and Conclusion

Though it is well documented that a rapid CBF change can lead to the brain temperature change and the water T_1^{app} relaxation processing is sensitive to brain temperature, to our best knowledge, this study presents the first investigation aiming to quantify the brain temperature effects on both T_1^{app} and CBF measurements during physiology/pathology conditions at 9.4T. This was accomplished through the

simultaneous measurements of T_1^{app}/CBF/brain temperature changes during the course of physiological/pathological perturbation.

It has been reported that the blood T_1 varies linearly with 1/T over the range of 0º-40º, suggesting a possible linear relationship between $R_1(1/T_1)$ versus the brain temperature [54]. Our results (e.g., Supplementary Figure S.1c) are consistent with the relationship. The temperature dependent coefficient of m as measured in this study was 36.1 ± 8.7 (ms/ºC). This m value can be converted to 1.6% of T_1^{app} per ºC, which is in excellent agreement with the value of 1.4% of T_1^{app} per ºC reported in the literature [164].

The effect of brain temperature change on T_1^{app} and ΔCBF measurements depends on the type of perturbation. The rat brain temperature decreased 0.26 ± 0.02ºC during the ischemia perturbation; and its effect attributes only 3.2% of the total change in ΔT_1^{app}; in contrast, the maximum brain temperature increased 0.93 ± 0.09ºC and attributes ~15.3% of ΔT_1^{app} during the hypercapnia perturbation. Similar to the hypercapnia, the temperature effect could also attribute 19.9 % of the measured ΔT_1^{app} during the initial post-ischemia stage (**S3**). Nevertheless, the perfusion change attributes more than 80% of the total T_1^{app} change. As a result, the imaged ΔR_1^{app} is dominated by ΔCBF and it provides a sensitive index reflecting the perfusion change in the brain tissue. This notion is confirmed by the statistical comparison results as summarized in Supplementary Table 1.2, suggesting that both ΔR_1^{app} and ΔR_1^{CBF} have an excellent correlation with the absolute CBF changes in either ischemia or hypercapnia perturbations. Although ΔR_1^{CBF} has a slightly better correlation with rCBF than ΔR_1^{app}, there was no statistically

significant difference between them, presumably, a small confound effect of brain temperature change on the ΔR_1^{CBF} values (<20%) could be approximately ignored, even when substantial brain temperature changes occurred during either the global ischemia or 10% CO_2 hypercapnia perturbation. In addition, a strong and positive correlation is shown between (rCBF-1) and ΔR_1^{app} during the whole ischemia experiment in Supplementary Figure S.1d. With the slope derived from Supplementary Figure S.1d, a baseline CBF value at reference condition can be estimated as CBF_{RC} = (60sec/min)· λ(ml/g)/ 52.3 (sec) = 1.03 ml/g/min using Eqs. (2.15) and (2.16) in chapter 2. This baseline CBF value is close to the value we obtained by employing R_1^{CBF} and the literature reported values (chapter 2 Table 2.2). Therefore, for most physiological/pathological applications with technical difficulties in measuring the brain temperature change as well as the chronic disease with slow temperature change, the ΔR_1^{app} image should provide a reasonable approximation reflecting the absolute CBF change.

Reference

1. Raichle, M.E., et al., *Brain blood flow measured with intravenous $H_2{}^{15}O$. II. Implementation and validation.* J Nucl Med, 1983. **24**(9): p. 790-8.
2. Zhu, X.H., et al., *Simultaneous oxygenation and perfusion imaging study of functional activity in primary visual cortex at different visual stimulation frequency: quantitative correlation between BOLD and CBF changes.* Magn Reson Med, 1998. **40**(5): p. 703-11.
3. Kim, T., et al., *Arterial versus total blood volume changes during neural activity-induced cerebral blood flow change: implication for BOLD fMRI.* J Cereb Blood Flow Metab, 2007. **27**(6): p. 1235-47.
4. Chalela, J.A., et al., *Magnetic resonance perfusion imaging in acute ischemic stroke using continuous arterial spin labeling.* Stroke, 2000. **31**(3): p. 680-7.
5. Detre, J.A. and J. Wang, *Technical aspects and utility of fMRI using BOLD and ASL.* Clin Neurophysiol, 2002. **113**(5): p. 621-34.
6. Ota, M., et al., *Abnormalities of cerebral blood flow in multiple sclerosis: a pseudocontinuous arterial spin labeling MRI study.* Magn Reson Imaging, 2013. **31**(6): p. 990-5.
7. Kety, S.S. and C.F. Schmidt, *The Nitrous Oxide Method for the Quantitative Determination of Cerebral Blood Flow in Man: Theory, Procedure and Normal Values.* J Clin Invest, 1948. **27**(4): p. 476-83.
8. Lassen, N.A. and D.H. Ingvar, *The blood flow of the cerebral cortex determined by radioactive krypton.* Experientia, 1961. **17**: p. 42-3.
9. Obrist, W.D., et al., *Determination of regional cerebral blood flow by inhalation of 133-Xenon.* Circ Res, 1967. **20**(1): p. 124-35.
10. Austin, G., et al., *Description and early results of an intravenous radioisotope technique for measuring regional cerebral blood flow in man.* Eur Neurol, 1972. **8**(1): p. 43-51.

11. Obrist, W.D., et al., *Regional cerebral blood flow estimated by 133-xenon inhalation.* Stroke, 1975. **6**(3): p. 245-56.
12. Bruce, D.A., et al., *Regional cerebral blood flow, intracranial pressure, and brain metabolism in comatose patients.* J Neurosurg, 1973. **38**(2): p. 131-44.
13. Huang, S.C., et al., *Noninvasive determination of local cerebral metabolic rate of glucose in man.* Am J Physiol, 1980. **238**(1): p. E69-82.
14. Heiss, W.D., et al., *Regional kinetic constants and cerebral metabolic rate for glucose in normal human volunteers determined by dynamic positron emission tomography of [18F]-2-fluoro-2-deoxy-D-glucose.* J Cereb Blood Flow Metab, 1984. **4**(2): p. 212-23.
15. Phelps, M.E., J.C. Mazziotta, and S.C. Huang, *Study of cerebral function with positron computed tomography.* J Cereb Blood Flow Metab, 1982. **2**(2): p. 113-62.
16. Zhu, X.H., et al., *In vivo measurement of CBF using (17) O NMR signal of metabolically produced H2 (17) O as a perfusion tracer.* Magn Reson Med, 2013. **70**(2): p. 309-14.
17. Zhu, X.H., et al., *Simultaneous and noninvasive imaging of cerebral oxygen metabolic rate, blood flow and oxygen extraction fraction in stroke mice.* Neuroimage, 2013. **64**: p. 437-47.
18. Rudolph, A.M. and M.A. Heymann, *The circulation of the fetus in utero. Methods for studying distribution of blood flow, cardiac output and organ blood flow.* Circ Res, 1967. **21**(2): p. 163-84.
19. Yang, S.P. and J.A. Krasney, *Cerebral blood flow and metabolic responses to sustained hypercapnia in awake sheep.* J Cereb Blood Flow Metab, 1995. **15**(1): p. 115-23.
20. Frerichs, K.U. and G.Z. Feuerstein, *Laser-Doppler flowmetry. A review of its application for measuring cerebral and spinal cord blood flow.* Mol Chem Neuropathol, 1990. **12**(1): p. 55-70.

21. Meyerson, B.A., et al., *Bedside monitoring of regional cortical blood flow in comatose patients using laser Doppler flowmetry.* Neurosurgery, 1991. **29**(5): p. 750-5.
22. Chan, K.H., N.M. Dearden, and J.D. Miller, *Transcranial Doppler-sonography in severe head injury.* Acta Neurochir Suppl (Wien), 1993. **59**: p. 81-5.
23. Steiger, H.J., et al., *Transcranial Doppler monitoring in head injury: relations between type of injury, flow velocities, vasoreactivity, and outcome.* Neurosurgery, 1994. **34**(1): p. 79-85; discussion 85-6.
24. Jobsis, F.F., *Noninvasive, infrared monitoring of cerebral and myocardial oxygen sufficiency and circulatory parameters.* Science, 1977. **198**(4323): p. 1264-7.
25. McCormick, P.W., et al., *Regional cerebrovascular oxygen saturation measured by optical spectroscopy in humans.* Stroke, 1991. **22**(5): p. 596-602.
26. Carter, L.P., *Surface monitoring of cerebral cortical blood flow.* Cerebrovasc Brain Metab Rev, 1991. **3**(3): p. 246-61.
27. Villringer, A., et al., *Dynamic imaging with lanthanide chelates in normal brain: contrast due to magnetic susceptibility effects.* Magn Reson Med, 1988. **6**(2): p. 164-74.
28. Rosen, B.R., et al., *Perfusion imaging with NMR contrast agents.* Magn Reson Med, 1990. **14**(2): p. 249-65.
29. Detre, J.A., et al., *Perfusion imaging.* Magn Reson Med, 1992. **23**(1): p. 37-45.
30. Williams, D.S., et al., *Magnetic resonance imaging of perfusion using spin inversion of arterial water.* Proc Natl Acad Sci U S A, 1992. **89**(1): p. 212-6.
31. Edelman, R.R., et al., *Qualitative mapping of cerebral blood flow and functional localization with echo-planar MR imaging and signal targeting with alternating radio frequency.* Radiology, 1994. **192**(2): p. 513-20.
32. Kim, S.G., *Quantification of relative cerebral blood flow change by flow-sensitive alternating inversion recovery (FAIR) technique: application to functional mapping.* Magn Reson Med, 1995. **34**(3): p. 293-301.
33. Kwong, K.K., et al., *MR perfusion studies with T1-weighted echo planar imaging.* Magn Reson Med, 1995. **34**(6): p. 878-87.

34. Wong, E.C., R.B. Buxton, and L.R. Frank, *A theoretical and experimental comparison of continuous and pulsed arterial spin labeling techniques for quantitative perfusion imaging.* Magn Reson Med, 1998. **40**(3): p. 348-55.
35. Wong, E.C., R.B. Buxton, and L.R. Frank, *Quantitative imaging of perfusion using a single subtraction (QUIPSS and QUIPSS II).* Magn Reson Med, 1998. **39**(5): p. 702-8.
36. Calamante, F., et al., *Measuring cerebral blood flow using magnetic resonance imaging techniques.* J Cereb Blood Flow Metab, 1999. **19**(7): p. 701-35.
37. Kwong, K.K., et al., *Dynamic magnetic resonance imaging of human brain activity during primary sensory stimulation.* Proc Natl Acad Sci U S A, 1992. **89**(12): p. 5675-9.
38. Schwarzbauer, C., S.P. Morrissey, and A. Haase, *Quantitative magnetic resonance imaging of perfusion using magnetic labeling of water proton spins within the detection slice.* Magn Reson Med, 1996. **35**(4): p. 540-6.
39. Calamante, F., et al., *Early changes in water diffusion, perfusion, T_1, and T_2 during focal cerebral ischemia in the rat studied at 8.5 T.* Magn Reson Med, 1999. **41**(3): p. 479-85.
40. Grohn, O.H., et al., *On- and off-resonance T(1rho) MRI in acute cerebral ischemia of the rat.* Magn Reson Med, 2003. **49**(1): p. 172-6.
41. Barber, P.A., et al., *Early T1- and T2-weighted MRI signatures of transient and permanent middle cerebral artery occlusion in a murine stroke model studied at 9.4T.* Neurosci Lett, 2005. **388**(1): p. 54-9.
42. Shen, Q., et al., *Spatiotemporal characteristics of postischemic hyperperfusion with respect to changes in T1, T2, diffusion, angiography, and blood-brain barrier permeability.* J Cereb Blood Flow Metab, 2011. **31**(10): p. 2076-85.
43. Frackowiak, R.S., et al., *Quantitative measurement of regional cerebral blood flow and oxygen metabolism in man using 15O and positron emission tomography: theory, procedure, and normal values.* J Comput Assist Tomogr, 1980. **4**(6): p. 727-36.

44. Stern, M.D., *In vivo evaluation of microcirculation by coherent light scattering.* Nature, 1975. **254**(5495): p. 56-8.
45. Dirnagl, U., et al., *Continuous measurement of cerebral cortical blood flow by laser-Doppler flowmetry in a rat stroke model.* J Cereb Blood Flow Metab, 1989. **9**(5): p. 589-96.
46. Wadhwani KC, R., *Blood flow in the central and peripheral nervous system. In laser-Doppler blood flowmetry (öberg PA, ed).* 1988: Boston, MA: Kluwer Academic. pp 265-288.
47. Fabricius, M. and M. Lauritzen, *Laser-Doppler evaluation of rat brain microcirculation: comparison with the [14C]-iodoantipyrine method suggests discordance during cerebral blood flow increases.* J Cereb Blood Flow Metab, 1996. **16**(1): p. 156-61.
48. Kramer, M.S., et al., *Comparison of cerebral blood flow measured by laser-Doppler flowmetry and hydrogen clearance in cats after cerebral insult and hypervolemic hemodilution.* Neurosurgery, 1996. **38**(2): p. 355-61.
49. Buxton, R.B., E.C. Wong, and L.R. Frank, *Dynamics of blood flow and oxygenation changes during brain activation: the balloon model.* Magn Reson Med, 1998. **39**(6): p. 855-64.
50. Kim, S.G. and K. Ugurbil, *Comparison of blood oxygenation and cerebral blood flow effects in fMRI: estimation of relative oxygen consumption change.* Magn Reson Med, 1997. **38**(1): p. 59-65.
51. Lythgoe, M.F., et al., *Acute changes in MRI diffusion, perfusion, T_1, and T_2 in a rat model of oligemia produced by partial occlusion of the middle cerebral artery.* Magn Reson Med, 2000. **44**(5): p. 706-12.
52. van der Toorn, A., et al., *T_1 and T_2 relaxation times of the major ^{1}H-containing metabolites in rat brain after focal ischemia.* NMR Biomed, 1995. **8**(6): p. 245-52.
53. Quesson, B., J.A. de Zwart, and C.T. Moonen, *Magnetic resonance temperature imaging for guidance of thermotherapy.* J Magn Reson Imaging, 2000. **12**(4): p. 525-33.

54. Parker, D.L., et al., *Temperature distribution measurements in two-dimensional NMR imaging.* Med Phys, 1983. **10**(3): p. 321-5.
55. Dickinson, R.J., et al., *Measurement of changes in tissue temperature using MR imaging.* J Comput Assist Tomogr, 1986. **10**(3): p. 468-72.
56. Botnar, R., *Temperature sensitive MR sequences.* 1998.
57. Ogawa, S., et al., *Oxygenation-sensitive contrast in magnetic resonance image of rodent brain at high magnetic fields.* Magn Reson Med, 1990. **14**(1): p. 68-78.
58. Ogawa, S., et al., *Brain magnetic resonance imaging with contrast dependent on blood oxygenation.* Proc. Natl. Acad. Sci. USA, 1990. **87**: p. 9868-9872.
59. Mansfield, P., *Multi-planar image formation using NMR spin echoes.* J. Phys. C, 1977. **10**: p. L55-L58.
60. Ackerman, J.J., et al., *Mapping of metabolites in whole animals by 31P NMR using surface coils.* Nature, 1980. **283**(5743): p. 167-70.
61. Herscovitch, P. and M.E. Raichle, *What is the correct value for the brain--blood partition coefficient for water?* J Cereb Blood Flow Metab, 1985. **5**(1): p. 65-9.
62. Tsekos, N.V., et al., *Quantitative measurements of cerebral blood flow in rats using the FAIR technique: correlation with previous iodoantipyrine autoradiographic studies.* Magn Reson Med, 1998. **39**(4): p. 564-73.
63. Barbier, E.L., et al., *Perfusion imaging using dynamic arterial spin labeling (DASL).* Magn Reson Med, 2001. **45**(6): p. 1021-9.
64. Zhang, W., et al., *Measurement of brain perfusion by volume-localized NMR spectroscopy using inversion of arterial water spins: accounting for transit time and cross-relaxation.* Magn Reson Med, 1992. **25**(2): p. 362-71.
65. Dobre, M.C., K. Ugurbil, and M. Marjanska, *Determination of blood longitudinal relaxation time T_1 at high magnetic field strengths.* Magn Reson Imaging, 2007. **25**(5): p. 733-5.
66. Sugio, K., et al., *A model of bilateral hemispheric ischemia--modified four-vessel occlusion in rats.* Stroke, 1988. **19**(7): p. 922.
67. Haase, A., et al., *FLASH imaging. Rapid NMR imaging using low flip angle pulses.* J. Magn. Reson., 1986. **67**: p. 258-266.

68. Pulsinelli, W.A. and J.B. Brierley, *A new model of bilateral hemispheric ischemia in the unanesthetized rat.* Stroke, 1979. **10**(3): p. 267-72.
69. Strupp, J.P., *Stimulate: A GUI based fMRI analysis software package.* Neuroimage 3:S607, 1996.
70. Bell, B.A., L. Symon, and N.M. Branston, *CBF and time thresholds for the formation of ischemic cerebral edema, and effect of reperfusion in baboons.* J Neurosurg, 1985. **62**(1): p. 31-41.
71. Iwama, T., et al., *Proton NMR studies on ischemic rat brain tissue.* Magn Reson Med, 1992. **25**(1): p. 78-84.
72. Young, W., et al., *Regional brain sodium, potassium, and water changes in the rat middle cerebral artery occlusion model of ischemia.* Stroke, 1987. **18**(4): p. 751-9.
73. Davis, T.L., et al., *Calibrated functional MRI: mapping the dynamics of oxidative metabolism.* Proc Natl Acad Sci U S A, 1998. **95**(4): p. 1834-9.
74. Wang, X., et al. *Simultaneous Imaging of Absolute CBF Change and BOLD with Saturation-Recovery-T1 MRI Approach under Ischemia and Hypercapnia*. in *ISMRM 17th Annual Meeting*. 2009. Hawaii.
75. Alsop, D.C. and J.A. Detre, *Reduced transit-time sensitivity in noninvasive magnetic resonance imaging of human cerebral blood flow.* J Cereb Blood Flow Metab, 1996. **16**(6): p. 1236-49.
76. Darquie, A., et al., *Transient decrease in water diffusion observed in human occipital cortex during visual stimulation.* Proc Natl Acad Sci U S A, 2001. **98**(16): p. 9391-5.
77. Harshbarger, T.B. and A.W. Song, *B factor dependence of the temporal characteristics of brain activation using dynamic apparent diffusion coefficient contrast.* Magn Reson Med, 2004. **52**(6): p. 1432-7.
78. Song, A.W., et al., *Enhanced spatial localization of neuronal activation using simultaneous apparent-diffusion-coefficient and blood-oxygenation functional magnetic resonance imaging.* Neuroimage, 2002. **17**(2): p. 742-50.

79. Song, A.W. and S.L. Gangstead, *The spatial and temporal characteristics of the apparent-diffusion-coefficient-dependent fMRI signal changes during visual stimulation.* J Neural Eng, 2004. **1**(1): p. 32-8.
80. Kennan, R.P., et al., *A general model of microcirculatory blood flow effects in gradient sensitized MRI.* Med Phys, 1994. **21**(4): p. 539-45.
81. Lorenz, C.H., et al., *Magnetic resonance diffusion/perfusion phantom experiments.* Magn Reson Med, 1991. **19**(2): p. 254-60.
82. Luo, Y., et al., *BISTRO: an outer-volume suppression method that tolerates RF field inhomogeneity.* Magn Reson Med, 2001. **45**(6): p. 1095-102.
83. Zhang, W., D.S. Williams, and A.P. Koretsky, *Measurement of rat brain perfusion by NMR using spin labeling of arterial water: in vivo determination of the degree of spin labeling.* Magn Reson Med, 1993. **29**(3): p. 416-21.
84. Rudin, M. and A. Sauter, *Non-invasive determination of cerebral blood flow changes by 19F NMR spectroscopy.* NMR Biomed, 1989. **2**(3): p. 98-103.
85. Wegener, S., et al., *Quantification of rodent cerebral blood flow (CBF) in normal and high flow states using pulsed arterial spin labeling magnetic resonance imaging.* J Magn Reson Imaging, 2007. **26**(4): p. 855-62.
86. Wang, X., et al. *Further Test and Validation of Saturation-recovery T1 MRI Measurement for Imaging Absolute CBF Change*. in *ISMRM 18th Annual Meeting*. 2010. Stockholm.
87. Silva, A.C., et al., *Multi-slice MRI of rat brain perfusion during amphetamine stimulation using arterial spin labeling.* Magn Reson Med, 1995. **33**(2): p. 209-14.
88. Alsop, D.C. and J.A. Detre, *Multisection cerebral blood flow MR imaging with continuous arterial spin labeling.* Radiology, 1998. **208**(2): p. 410-6.
89. Silva, A.C. and S.G. Kim, *Pseudo-continuous arterial spin labeling technique for measuring CBF dynamics with high temporal resolution.* Magn Reson Med, 1999. **42**(3): p. 425-9.

90. Zhang, W., et al., *NMR measurement of perfusion using arterial spin labeling without saturation of macromolecular spins.* Magn Reson Med, 1995. **33**(3): p. 370-6.
91. Silva, A.C., et al., *Estimation of water extraction fractions in rat brain using magnetic resonance measurement of perfusion with arterial spin labeling.* Magn Reson Med, 1997. **37**(1): p. 58-68.
92. Kim T, K., S. G., *Dynamics of Arterial Labeled Spins Investigated by using 2-coil DASL.* 2002: p. 1061.
93. Kim, T. and S.G. Kim, *Quantification of cerebral arterial blood volume and cerebral blood flow using MRI with modulation of tissue and vessel (MOTIVE) signals.* Magn Reson Med, 2005. **54**(2): p. 333-42.
94. Meyer, J.S., et al., *Local cerebral blood flow and tissue solubility measured by stable, xenon-enhanced computerized tomography.* Adv Neurol, 1981. **30**: p. 73-84.
95. Roberts, D.A., et al., *Magnetic resonance imaging of the brain: blood partition coefficient for water: application to spin-tagging measurement of perfusion.* J Magn Reson Imaging, 1996. **6**(2): p. 363-6.
96. Wang, X., et al. *A Comparison Study of Imaging Absolute CBF Change in Rat Brain with SR-T1app method and CASL technique*. in *ISMRM 19th Annual Meeting*. 2011. Montreal.
97. Frietsch, T., et al., *Relationship between local cerebral blood flow and metabolism during mild and moderate hypothermia in rats.* Anesthesiology, 2000. **92**(3): p. 754-63.
98. Hansen, T.D., et al., *Distribution of cerebral blood flow during halothane versus isoflurane anesthesia in rats.* Anesthesiology, 1988. **69**(3): p. 332-7.
99. Shen, Q., et al., *Functional, perfusion and diffusion MRI of acute focal ischemic brain injury.* J Cereb Blood Flow Metab, 2005. **25**(10): p. 1265-79.
100. Pohmann, R., G. Shajan, and D.Z. Balla, *Contrast at high field: relaxation times, magnetization transfer and phase in the rat brain at 16.4 T.* Magn Reson Med, 2011. **66**(6): p. 1572-81.

101. Bandettini, P.A., et al., *Time course EPI of human brain function during task activation.* Magn Reson Med, 1992. **25**(2): p. 390-7.
102. Ogawa, S., et al., *Intrinsic signal changes accompanying sensory stimulation: functional brain mapping with magnetic resonance imaging.* Proc Natl Acad Sci U S A, 1992. **89**(13): p. 5951-5.
103. Ogawa, S., et al., *On the characteristics of functional magnetic resonance imaging of the brain.* Annu Rev Biophys Biomol Struct, 1998. **27**: p. 447-74.
104. Cohen, E.R., et al., *Hypercapnic normalization of BOLD fMRI: comparison across field strengths and pulse sequences.* Neuroimage, 2004. **23**(2): p. 613-24.
105. Duong, T.Q., et al., *Microvascular BOLD contribution at 4 and 7 T in the human brain: gradient-echo and spin-echo fMRI with suppression of blood effects.* Magn Reson Med, 2003. **49**(6): p. 1019-27.
106. Frahm, J., et al., *Brain or vein--oxygenation or flow? On signal physiology in functional MRI of human brain activation.* NMR Biomed, 1994. **7**(1-2): p. 45-53.
107. Gao, J.H., et al., *Quantitative assessment of blood inflow effects in functional MRI signals.* Magn Reson Med, 1996. **36**(2): p. 314-9.
108. Kim, S.G., et al., *Potential pitfalls of functional MRI using conventional gradient-recalled echo techniques.* NMR Biomed, 1994. **7**(1-2): p. 69-74.
109. Lu, H., X. Golay, and P.C. van Zijl, *Intervoxel heterogeneity of event-related functional magnetic resonance imaging responses as a function of T(1) weighting.* Neuroimage, 2002. **17**(2): p. 943-55.
110. Kruger, G., et al., *Simultaneous monitoring of dynamic changes in cerebral blood flow and oxygenation during sustained activation of the human visual cortex.* Neuroreport, 1999. **10**(14): p. 2939-43.
111. Boxerman, J.L., et al., *The intravascular contribution to fMRI signal change: Monte Carlo modeling and diffusion-weighted studies in vivo.* Magn Reson Med, 1995. **34**(1): p. 4-10.
112. Le Bihan, D., et al., *MR imaging of intravoxel incoherent motions: application to diffusion and perfusion in neurologic disorders.* Radiology, 1986. **161**(2): p. 401-7.

113. Song, A.W., et al., *Diffusion weighted fMRI at 1.5 T.* Magn Reson Med, 1996. **35**(2): p. 155-8.

114. Bandettini, P.A., et al., *Processing strategies for time-course data sets in functional MRI of the human brain.* Magn Reson Med, 1993. **30**(2): p. 161-73.

115. Kim, T. and S.G. Kim, *Quantification of cerebral arterial blood volume using arterial spin labeling with intravoxel incoherent motion-sensitive gradients.* Magn Reson Med, 2006. **55**(5): p. 1047-57.

116. Kim, S.G., X. Hu, and K. Ugurbil, *Accurate T1 determination from inversion recovery images: application to human brain at 4 Tesla.* Magn Reson Med, 1994. **31**(4): p. 445-9.

117. Rooney, W.D., et al., *Magnetic field and tissue dependencies of human brain longitudinal 1H2O relaxation in vivo.* Magn Reson Med, 2007. **57**(2): p. 308-18.

118. Donahue, M.J., et al., *Effect of inflow of fresh blood on vascular-space-occupancy (VASO) contrast.* Magn Reson Med, 2009. **61**(2): p. 473-80.

119. Goelman, G., et al., *Tracking the effects of crusher gradients on gradient-echo BOLD signal in space and time during rat sensory stimulation.* Magn Reson Med, 2008. **60**(3): p. 548-54.

120. Yacoub, E., et al., *Decreases in ADC observed in tissue areas during activation in the cat visual cortex at 9.4 T using high diffusion sensitization.* Magn Reson Imaging, 2008. **26**(7): p. 889-96.

121. Harshbarger, T.B. and A.W. Song, *Differentiating sensitivity of post-stimulus undershoot under diffusion weighting: implication of vascular and neuronal hierarchy.* PLoS ONE, 2008. **3**(8): p. e2914.

122. Michelich, C.R., A.W. Song, and J.R. Macfall, *Dependence of gradient-echo and spin-echo BOLD fMRI at 4 T on diffusion weighting.* NMR Biomed, 2006. **19**(5): p. 566-72.

123. Lee, S.P., et al., *Diffusion-weighted spin-echo fMRI at 9.4 T: microvascular/tissue contribution to BOLD signal changes.* Magn Reson Med, 1999. **42**(5): p. 919-28.

124. Wang, X. and W. Chen. *Substantial Flow-related Contribution in fMRI Signal Observed in Human Visual Cortex at 4T*. in *ISMRM 18th Annual Meeting*. 2010. Stockholm.

125. Gibbs, J.M., et al., *Evaluation of cerebral perfusion reserve in patients with carotid-artery occlusion.* Lancet, 1984. **1**(8370): p. 182-6.

126. Nezu, T., et al., *Preserved acetazolamide reactivity in lacunar patients with severe white-matter lesions: 15O-labeled gas and H2O positron emission tomography studies.* J Cereb Blood Flow Metab, 2012. **32**(5): p. 844-50.

127. Vorstrup, S., L. Henriksen, and O.B. Paulson, *Effect of acetazolamide on cerebral blood flow and cerebral metabolic rate for oxygen.* J Clin Invest, 1984. **74**(5): p. 1634-9.

128. Aso, K., et al., *Preoperative cerebrovascular reactivity to acetazolamide measured by brain perfusion SPECT predicts development of cerebral ischemic lesions caused by microemboli during carotid endarterectomy.* Eur J Nucl Med Mol Imaging, 2009. **36**(2): p. 294-301.

129. Ratnatunga, C. and M. Adiseshiah, *Increase in middle cerebral artery velocity on breath holding: a simplified test of cerebral perfusion reserve.* Eur J Vasc Surg, 1990. **4**(5): p. 519-23.

130. Muller, M., et al., *Assessment of cerebral vasomotor reactivity by transcranial Doppler ultrasound and breath-holding. A comparison with acetazolamide as vasodilatory stimulus.* Stroke, 1995. **26**(1): p. 96-100.

131. Willie, C.K., et al., *Utility of transcranial Doppler ultrasound for the integrative assessment of cerebrovascular function.* J Neurosci Methods, 2011. **196**(2): p. 221-37.

132. Leoni, R.F., et al., *Assessing Cerebrovascular Reactivity in Carotid Steno-Occlusive Disease Using MRI BOLD and ASL Techniques.* Radiol Res Pract, 2012. **2012**: p. 268483.

133. Noth, U., et al., *Cerebral vascular response to hypercapnia: determination with perfusion MRI at 1.5 and 3.0 Tesla using a pulsed arterial spin labeling technique.* J Magn Reson Imaging, 2006. **24**(6): p. 1229-35.

134. Divani, A., et al. *Development of A Custom-Design Microwire for Endovascular Occlusion of Middle Cerebral Artery in Rats via Transformoral Approach*. in *the XXVIth International Symposium on Cerebral Blood Flow, Metabolism and Function & XIth International Conference on Quantification of Brain Function with PET*. 2013. Shanghai.

135. Divani, A.A., et al., *Development of an Endoluminal Microwire for Focal Middle Cerebral Artery Occlusion in Rodents.*, in *The 2012 Design of Medical Devices Conference*. 2013: Minneapolis.

136. Goljan, E.F., *Rapid Review Pathology*. 3rd ed. 2007: Elservier. p576.

137. Dirnagl, U., C. Iadecola, and M.A. Moskowitz, *Pathobiology of ischaemic stroke: an integrated view.* Trends Neurosci, 1999. **22**(9): p. 391-7.

138. LJ, L., *Water relaxation in heterogeneous and biological systems.* Magnetic Resonance in Biology, 1983. **2**: p. p 280–286.

139. Wolff, S.D. and R.S. Balaban, *Magnetization transfer contrast (MTC) and tissue water proton relaxation in vivo.* Magn Reson Med, 1989. **10**(1): p. 135-44.

140. Betz, A.L., F. Iannotti, and J.T. Hoff, *Brain edema: a classification based on blood-brain barrier integrity.* Cerebrovasc Brain Metab Rev, 1989. **1**(2): p. 133-54.

141. Qiao, M., et al., *Transient hypoxia-ischemia in rats: changes in diffusion-sensitive MR imaging findings, extracellular space, and Na+-K+ -adenosine triphosphatase and cytochrome oxidase activity.* Radiology, 2002. **223**(1): p. 65-75.

142. Nakamura, K., et al., *Quantitative accuracy of delayed hyperperfusion in MRI of transient ischemia in rats.* Conf Proc IEEE Eng Med Biol Soc, 2008. **2008**: p. 839-42.

143. Tanaka, Y., et al., *Arterial spin labeling and dynamic susceptibility contrast CBF MRI in postischemic hyperperfusion, hypercapnia, and after mannitol injection.* J Cereb Blood Flow Metab. **31**(6): p. 1403-11.

144. Astrup, J., B.K. Siesjo, and L. Symon, *Thresholds in cerebral ischemia - the ischemic penumbra.* Stroke, 1981. **12**(6): p. 723-5.

145. Barber, P.A., et al., *Prediction of stroke outcome with echoplanar perfusion- and diffusion-weighted MRI.* Neurology, 1998. **51**(2): p. 418-26.
146. Neumann-Haefelin, T., et al., *Diffusion- and perfusion-weighted MRI. The DWI/PWI mismatch region in acute stroke.* Stroke, 1999. **30**(8): p. 1591-7.
147. Kanno, I., et al., *Oxygen extraction fraction at maximally vasodilated tissue in the ischemic brain estimated from the regional CO2 responsiveness measured by positron emission tomography.* J Cereb Blood Flow Metab, 1988. **8**(2): p. 227-35.
148. Heiss, W.D., et al., *Repeat positron emission tomographic studies in transient middle cerebral artery occlusion in cats: residual perfusion and efficacy of postischemic reperfusion.* J Cereb Blood Flow Metab, 1997. **17**(4): p. 388-400.
149. Kenneth, D.K., et al., *Deaths: final data for 2009*, in *Natl Vital Stat Rep*. 2011. p. 1-117.
150. Go, A.S., et al., *Heart disease and stroke statistics--2013 update: a report from the American Heart Association.* Circulation, 2013. **127**(1): p. e6-e245.
151. Schaller, B. and R. Graf, *Cerebral ischemia and reperfusion: the pathophysiologic concept as a basis for clinical therapy.* J Cereb Blood Flow Metab, 2004. **24**(4): p. 351-71.
152. Lo, E.H., M.A. Moskowitz, and T.P. Jacobs, *Exciting, radical, suicidal: how brain cells die after stroke.* Stroke, 2005. **36**(2): p. 189-92.
153. Doyle, K.P., R.P. Simon, and M.P. Stenzel-Poore, *Mechanisms of ischemic brain damage.* Neuropharmacology, 2008. **55**(3): p. 310-8.
154. Ackerman, R.H., et al., *Positron imaging in ischemic stroke disease using compounds labeled with oxygen 15. Initial results of clinicophysiologic correlations.* Arch Neurol, 1981. **38**(9): p. 537-43.
155. Zhu, X.H., et al., *Noninvasive and three-dimensional imaging of CMRO(2) in rats at 9.4 T: reproducibility test and normothermia/hypothermia comparison study.* J Cereb Blood Flow Metab, 2007. **27**(6): p. 1225-34.
156. Du, F., et al., *Tightly coupled brain activity and cerebral ATP metabolic rate.* Proc Natl Acad Sci U S A, 2008. **105**(17): p. 6409-14.

157. Zhu, X.H. and W. Chen, *In vivo oxygen-17 NMR for imaging brain oxygen metabolism at high field.* Prog Nucl Magn Reson Spectrosc, 2011. **59**(4): p. 319-35.
158. Faul, M., et al., *Traumatic Brain Injury in the United States: Emergency Department Visits, Hospitalizations, and Deaths, 2002-2006.* 2010.
159. Hoyt, D.B., et al., *Working Group on Trauma Research Program summary report: National Heart Lung Blood Institute (NHLBI), National Institute of General Medical Sciences (NIGMS), and National Institute of Neurological Disorders and Stroke (NINDS) of the National Institutes of Health (NIH), and the Department of Defense (DOD).* J Trauma, 2004. **57**(2): p. 410-5.
160. Ashikaga, R., Y. Araki, and O. Ishida, *MRI of head injury using FLAIR.* Neuroradiology, 1997. **39**(4): p. 239-42.
161. McGowan, J.C., et al., *Magnetization transfer imaging in the detection of injury associated with mild head trauma.* AJNR Am J Neuroradiol, 2000. **21**(5): p. 875-80.
162. Wang, X., et al., *Large enhancement of perfusion contribution on fMRI signal.* J Cereb Blood Flow Metab, 2012. **32**(5): p. 907-18.
163. Yablonskiy, D.A., J.J. Ackerman, and M.E. Raichle, *Coupling between changes in human brain temperature and oxidative metabolism during prolonged visual stimulation.* Proc Natl Acad Sci U S A, 2000. **97**(13): p. 7603-8.
164. Gary E. Wnek, G.L.B.-B.m., *Encyclopedia of Biomaterials and Biomedical Engineering*. 2004.